University of Seville

PhD Thesis

Dosimetry studies for radiation therapy with photons and radiobiology using low-energy protons:

(1) 2D dose verification for complex radiotherapy treatments
(2) Dosimetry of low-energy protons and first radiobiological experiments

Author:
Maria Cristina Battaglia

Directors:
Prof. J.M. Espino, Prof. M.I. Gallardo, Prof. D. Schardt

June 2017

Abstract

This thesis work is based on the knowledge about the interaction of radiation with matter to develop new methods with the aim of applying them to the radiation therapy and radiobiology, specifically to dose measurements in radiation therapy, dose measurements with low energy proton beams and DNA damages caused by these protons on cancer cells.

Thus, it presents two main parts: one regarding the presentation of a novel prototype based on silicon detector technology for treatment verification in radiotherapy, and the other, the instrumentation and the methodology for low energy proton beam characterization, dosimetry, with a special focus on the response of radiochromic films to protons, and finally the application on biological samples to study the DNA damage produced by protons.

The first part of this work presents a novel system with improved performances with respect to a previous system which was filed for a patent in September 13th 2011 at the OEMP - "Oficina Española de Patentes y Marcas"- Ministry of Industry, Tourism and Commerce, under reference number P201101009 [1]. This work was also published in specialized reviews and thesis works [2], [3], [4], [5]. The characterization of the response in terms of absorbed dose of this novel detector was presented in [6], [7] and [8].

Here, this study was repeated because of some modifications introduced in the electronics and in one of the detector's cables, which was modified due to a breakdown. The application of this system for complex treatment verification providing a 2D dose map reconstruction in the axial plane is presented for the first time in this thesis work.

The second part of the work presents the installation of instrumentation for dosimetry and radiobiology studies using proton beams produced by the 3 MV

Tandem accelerator at Centro Nacional de Acceleradores, Sevilla. The original work within this part can be divided into three main points: i) the elaboration of a protocol which allows to obtain a beam profile with low current and an homogeneous profile over the whole sample surface; ii) dosimetry with low energy protons using ionization chambers and radiochromic films; iii) study of the dosimetry at the Bragg peak. Last, the application of these studies to the irradiation of cell cultures is presented and preliminary results of the DNA damage produced by protons are shown.

Part of this work was published in a peer-review journal: **M. C. Battaglia et al.** "Dosimetric response of radiochromic films to protons of low energies in the Bragg peak region". *Physical Review Accelerators and Beams, 2016* [9].

Contents

List of Figures

List of Tables

Chapter 1

Introduction

Today cancer is a leading cause of death worldwide, accounting for around 13 % of all deaths (Globocan 2008). Knowledge about causes of cancer and interventions to prevent and manage the disease are extensive. In this scenario, radiotherapy plays an important role in the handling of a wide range of cancers since it is one of the most diffused techniques for the treatments. It uses ionizing radiation to stop the growth of malignant cells, by provoking the break of the DNA chain and leading them to death.

Another parameter of fundamental importance for the successful treatment of the disease must be taken into account: the resistance of some tumour cells to radiation. Thus, for tumors containing hypoxia cells (that are three times more radioresistant than oxygenated cells), it has been necessary to investigate how to increase the biological effectiveness of the radiations. Many studies have been conducted in this direction, discovering that heavy charged particles present a higher biological effectiveness over photons and electrons. For this reason, today, many clinical centers start to be equipped with accelerators that can produce and accelerate ions (most of them use protons) to treat cancer.

This thesis work consists of two main parts: the first one is about the development of a new technology of silicon detector with its dedicated electronics and acquisition system to provide an online monitoring of the dose delivered by a clinical linear accelerator (linac) in the context of conventional radiotherapy. This project wants to address the needs of having an on-line monitoring system of the dose delivering for treatment verification, proposing a resistant, fast and reusable device equipped

with a friendly user software interface which can provide dose map reconstructions with high spatial resolution.

The second part approaches the studies of the biological effectiveness of the radiation, presenting the work carried out to provide a beam line dedicated to dosimetry and radiobiology study using low energy proton beams. The beam analysis, characterization and optimization of the beam, energy and homogeneity onto the targets are shown in here. A special emphasis will be given to the dosimetry response of radiochromic films and, at the end, the results of a first breast cancer cell irradiation will be presented.

As a small introduction to the thesis, this chapter starts presenting the aim of the research work and continues with a brief overview of accelerators for therapy, with a distinction between therapy using photons or electrons and heavy charged particles.

1.1 Aim of this thesis work

As mentioned above, the doctoral thesis has two main cores: one regarding the treatment verification for complex radiotherapy, and the other presenting all the physical aspects that one must control before performing irradiation of cell cultures with low energy protons.

The novel system for radiotherapy treatment plan verification showed here, consists of a new detector designed by our group using the silicon technology to furnish better performances in terms of dose quantification, repeatability and rapidity of the analysis. This project (named Radia) is part of a wide collaboration which involves academic, research and clinical centers, specifically: the Department of Atomic, Molecular and Nuclear Physics and Department of Electronics Engineering of the University of Seville, the National Center of Accelerators of Seville (CNA) and the University Hospital Virgen Macarena of Seville (HUVM).

The detector, manufactured by the company Micron Semiconductor, is a dual chip single sided silicon strip detector (DSSSSD) formed by two strip detectors of silicon packed together with Kapton. Its response to photon radiation was studied and characterized as absorbed dose placing it in a polyethylene slab phantom and irradiating it with the detector's plane orthogonal to the beam direction. After

the characterization of the detector itself, a calibration as a real dosimeter is needed for reconstructing axial dose maps. With this scope, the detector was then installed in a cylindrical rotating phantom, remotely controlled. In this configuration, the detector plane is now parallel to the beam and a new calibration is needed. After calibrating, the system can be used for dose map reconstruction. Several projections for each detector strip are collected rotating the detector and then, by applying Radon transform and the calibration, are transformed in 2-D dose plots. In this way, the detector, placed in a polyethylene rotating phantom, allows to obtain 2D dose maps in the axial plane, furnishing a fast way of checking the radiation delivered by the clinical linacs.

The second part of the thesis illustrates the work born from a collaboration between the the Department of Atomic, Molecular and Nuclear Physics of the University of Seville, the National Centre of Accelerators (CNA) of Seville, the GSI Helmholtz Centre for Heavy Ions Research in Germany, the Department of Atomic, Molecular and Nuclear Physics of the University of Granada and the University Hospital San Cecilio of Granada. The National Centre of Accelerators in Seville, Spain, counts with a Tandem accelerator of 3MV maximum voltage. This device allows to perform cell irradiations with low energy proton beams, since the maximum energy that can provide for protons is 6 MeV. At the moment, few studies at low energies have been conducted in the field of radiobiology because of the difficulties of performing measurements in such regions (e. g. pioneering work performed earlier in 1990's by Belli et al. [10]).

This work shows the process for optimizing a beam line placed at the exit of the Tandem, in order to realize radiobiology studies on living cells. The main motivation of such investigation is the significant increase in using proton beams to treat cancers in recent years. Such tendency is mainly due to a combination of two factors: on one hand, the evidence of the benefits of this type of therapy over conventional radiotherapy (which uses photons or electrons for some types of tumors) and, on the other hand, the advent of new efficient and compact commercial equipments with affordable costs, which allowed many centers to be able to offer this treatment strategy.

A particular characteristic of protons and other ions is their depth dose profile that shows a sharp maximum ("Bragg peak") at the end of the range in tissue, where particles lose most of their initial energy. In this region, the radiobiological effectiveness (RBE) is not well established and therefore, to unveil this fact, it

is important to perform dedicated measurements. In this context the Tandem Accelerator which can provide proton beams with low energies, gives the possibility of making research in this interesting region of the Bragg curve and gives the chance of implementing radiobiological studies in this region. This work aims to provide further experimental data for dosimetry in the Bragg region for proton beams and to establish a relationship between dosimetry and linear energy transfer of these particles.

This thesis is organized in five chapters: it starts with a general introduction (this chapter), followed by chapter 2, dedicated to the physical aspects of radiation and the instrumentation used in the thesis work, with a special focus on silicon detectors and radiochromic films, which have been characterized as absolute dosimeters. Chapter 3 is dedicated to the description and the characterization of the novel system which employs the DSSSSD for dose maps reconstruction in complex radiotherapy treatments with photon beams.

Thus, this Chapter deals essentially with conventional radiotherapy only, while in Chapter 4, we present the physical and radiobiology studies performed using proton beams; In particular: the protocol adopted for the beam optimization, together with the proton dosimetry performed with radiochromic films and ionization chambers and, at the end of this chapter, the application to the irradiation of sample cells is presented and preliminary results are discussed.

Finally general conclusions and outlooks are given in Chapter 5.

1.2 Accelerators and their use in therapy

Accelerators dedicated to nuclear investigations began to be built in 1928 [11]. First accelerators were thought as vacuum tubes with high voltage terminals. Such accelerators were electrostatic and presented discharge issues. In order to obtain higher energies without increasing the voltage applied, Wideroe in 1928 and Lawrence and Sloan in 1930 thought about multiple accelerations. The cyclotron designed by Lawrence in 1929 was the first accelerator coupling magnetic and electric fields to obtain multiple accelerations: charged particles are forced into a circular trajectory that obliges them to go through the same voltage gap, by accelerating them many times. This mechanism allowed to construct compact

accelerators able to reach high energies. The development of the prototype was done at Berkeley laboratories.

Other accelerators based on cyclotron basis were developed, bringing in 1940 to the Kerst's apparatus, the betatrone, which used the electromagnetic induction to accelerate electrons up to many MeV. Further improvements of this technology led to the synchrotron, which presents the advantage of a ring structure, maintaining the ions with an appropriate magnetic field on the circular orbit. In these machines the beam has to be previously accelerated before being injected into the accelerator.

After the first treatments of cancer with X-rays at the end of the XIX century, many machines were developed to accelerate electrons and heavy charged particles with the scope of using them for therapy.

In this process, we can distinguish four main eras:

- the discovery era starts with the discovery of X-rays by W. C. Roentgen in 1895. In 1896, two treatments were performed with X-rays: the first one was performed in Chicago to treat a breast cancer and the second in Vienna for skin cancer treatment. During these years (until the 1920s) the basis of radiotherapy were developed. In this period, Becquerel (in 1895) and Marie and Pierre Curie (in 1898) discovered the natural radioactivity from uranium and radium. Radioactive sources were employed for internal treatments while X-rays for superficial ones. X-ray tubes (180-220 kV, by Collidge) were improved in order to have more penetrating X-rays. At that time, the biological effects were almost unknown, so treatments were conducted in an empirical way;

- the orthovoltage era, from 1920s to the 1950: a further development can be noticed for intra radioactive source applied to treat deep sited cancers, because of the lack of powerful X-ray tubes. This was also a transition period where the tubes were able to reach a voltage of 500 kV to 2 MV. With the construction of the betatron around 1940, therapy with electrons started to be available;

- the megavoltage era, from 1950 and still on going. In this era, we can distinguish two main developments: cobalt teletherapy units (producing γ-rays around 1.3 MV) and electron linacs (clinically available since 1950). The

first technology of electron linacs provided beams of 4-6 MeV, till the last developments which reached 10-20 MeV. The main advantage of these linacs, with respect to cobalt units, was to increase the penetration depth, sparing the damage on the skin. Despite of such improvements, the path of photons through the tissue was difficult to control. Multi-field treatment plans were implemented in order to disperse the dose contribution on normal tissues. Nowadays the research in conventional radiotherapy is focused on maximizing the dose to the diseased tissues and, at the same time, minimizing the dose on the healthy ones;

- the ion beams era: in 1946 Wilson proposed to use protons for therapy. The main motivation of Wilson was that protons, among the charged particles, offered the longest range for a given energy and were the simplest and most practical for medical use. A feasibility study for the clinical use of proton beams was conducted at Berkeley laboratories in 1954 (C. A. Tobias and coworkers) for the treatment of a pituitary gland tumor. Patient treatments started in this year at Berkeley laboratories, first with protons and later with helium beams. In Europe proton therapy begun in 1950s and 1960s at laboratories in Uppsala (Sweden), Moscow and St. Petersburg.

  In 1970, first clinical trials with light ions were performed. At Berkeley, in 1975-1992 most of the patients were treated with ^{20}Ne ions (670 MeV/u). This facility stopped its operation in 1992. In 1994 the heavy-ion medical accelerator in Chiba, Japan (HIMAC) dedicated to radiotherapy with carbon beams begun to be operative. First treatment in Europe with ^{12}C ions was performed at GSI laboratory, Darmstadt, in 1997. Clinical trials with He-ions are under preparation at HIT facility in Heidelberg; at present only proton and carbon ion beams are used for cancer treatments.

  According to the International Journal of Particle Therapy, from 1954 to 2014, more than 137000 patients were treated with particle therapy [12] (fig. 1.1), 86% of which were treated with protons and 14% with carbon ions or other particles. Hadrons are in general more suitable to treat deep sited tumors because of their capability in penetrating tissues, losing most of their energy at the end of their range in the medium. This allows to irradiate the region to be treated with higher precision, allowing to reduce the dose deposited in the healthy tissues surrounding the tumor. Besides that, they are also characterized by elevated linear energy transfer being a promising

technique to treat radioresistant tumors. Physical aspects of ions in therapy are discussed in section 1.4.

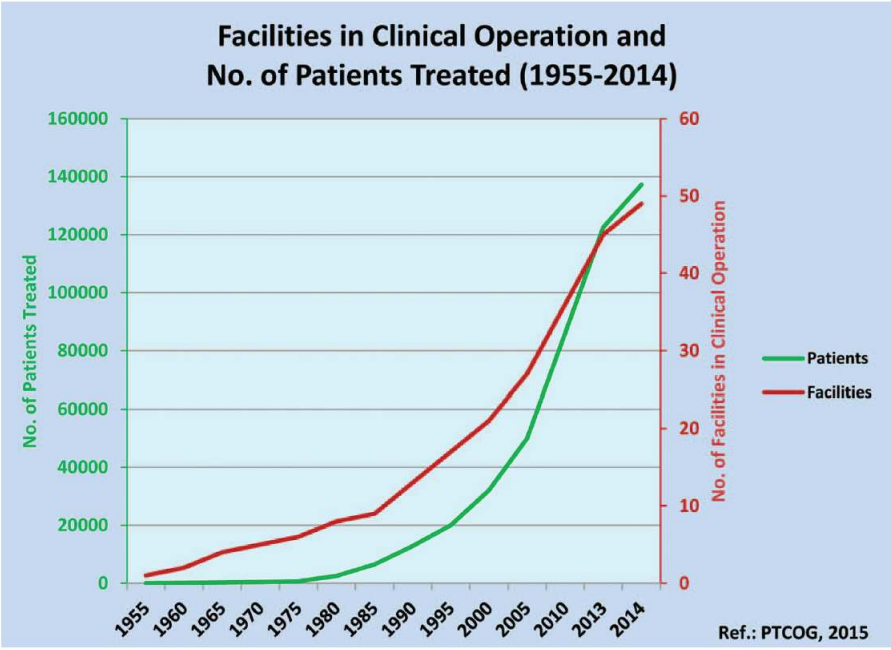

FIGURE 1.1: N° of patients and N° of facilities for treatments with particle accelerators (from 1954 to 2014).

1.3 Conventional radiation therapy

Nowadays, most radiation therapy is delivered with high energy photons (X-rays and γ rays mostly). Electrons are used to treat superficial tumors or in treatments where deep penetration is not required. Heavier charged particles, such as ions of hydrogen, helium, carbon and other nuclei, are being used increasingly to treat deep sited tumors.

All the types of radiations are able to kill tumor cells if the dose is high enough. In this context, radiation therapy is very useful since it stops cancer cells from dividing and growing, thus slowing or stopping tumor growth and in many cases is capable of killing all of the cancer cells, thus shrinking or eliminating the tumor.

Radiotherapy is basically performed in two ways:

a) Radioactive sources are placed close to the area to be treated: for instance, brachytherapy is an advanced technique where radioactive seeds or sources are

placed in or near the tumor itself, giving a high radiation dose to the tumor while reducing the radiation exposure in the surrounding healthy tissues. The term "brachy" is Greek for short distance, thus, brachytherapy is radiation therapy given at a short distance: localized and precise. Its use is limited by the anatomical location of the tumor because of its indication spectrum, which is significantly narrower in comparison with external radiotherapy.

b) The external beam therapy uses machines that deliver electrons or photons (by Brehmstralung), in order to irradiate the tumor from outside. This is mainly performed using clinical linacs. They are the most diffused and used in hospitals (operating at 6, 15, 18 MV), allowing to irradiate from several directions the tumour. Plenty of studies were and are performed in order to furnish more and more accurate evaluation of the dose to the target, trying to release to normal tissue the lowest amount of dose.

Films, ionization chambers (ICs), semiconductor detectors, thermo luminescent detectors (TLD) and optically stimulated luminescent detectors are being employed in order to furnish an accurate checking of the dose delivered by the accelerator to the patient.

Before delivering treatment to the patient, a treatment plan is developed and approved by the radiation oncologist in collaboration with the radiation dosimetrist and physicist. The plan is double-checked is given and quality-control procedures ensure that the treatment is delivered as planned.

Quality control of the linear accelerator is also very important. There are several systems using mainly film dosimetry and ionization chambers to reach the scope. Each morning before any patients are treated, the radiation therapist performs checks on the machine to make sure that the radiation intensity is uniform across the beam and that it is working properly. In addition, the radiation physicist conducts more detailed weekly and monthly checks of the linear accelerator [13].

In 2008, the 88 % of patients treated with radiation therapy received external beam treatments from a linear accelerator [14]. In order to improve the performances of radiation therapy treatments, a new technique was developed and now it is successfully adopted in clinical facilities, which is called “intensity modulated radiation therapy (IMRT)”. It allows to conform the dose more precisely to the three-dimensional (3-D) shape of the tumor, by modulating—or controlling—the intensity of the radiation beam in multiple small volumes. IMRT also allows higher

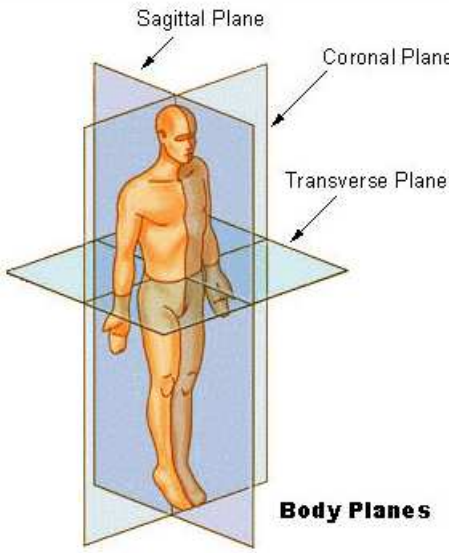

FIGURE 1.2: Axial, sagittal and coronal planes, from [2]

radiation doses to be focused in regions within the tumor while minimizing the dose to surrounding normal critical structures. This is possible by integrating the IMRT with 3-D computed tomography (CT) or magnetic resonance images (MRI) of the patient. Once the images are acquired, a treatment planning strategy is established in conjunction with computerized dose calculations to determine the dose intensity pattern that best conforms to the tumor shape. In general, treatment planes refer to three planes in the human body (fig. 1.2):

- Sagittal plane is the vertical plane that passes through the body from front to back. It divides the body into right and left halves.
- Transverse or axial plane is parallel to the floor when a patient is standing.
- Coronal plane is vertical and passes through the patient from side to side. It divides the body into front and back halves.

Typically, combinations of multiple intensity-modulated fields coming from different beam directions produce a custom tailored radiation dose. Fig. 1.3 shows the dose map distribution for a treatment of prostate cancer with conventional radiotherapy and with IMRT. As it can be easily seen, the areas close to the target volume are receiving less dose with IMRT than with conventional radiotherapy.

This fact reduces the side effects associated to the exposure of healthy tissues to radiation.

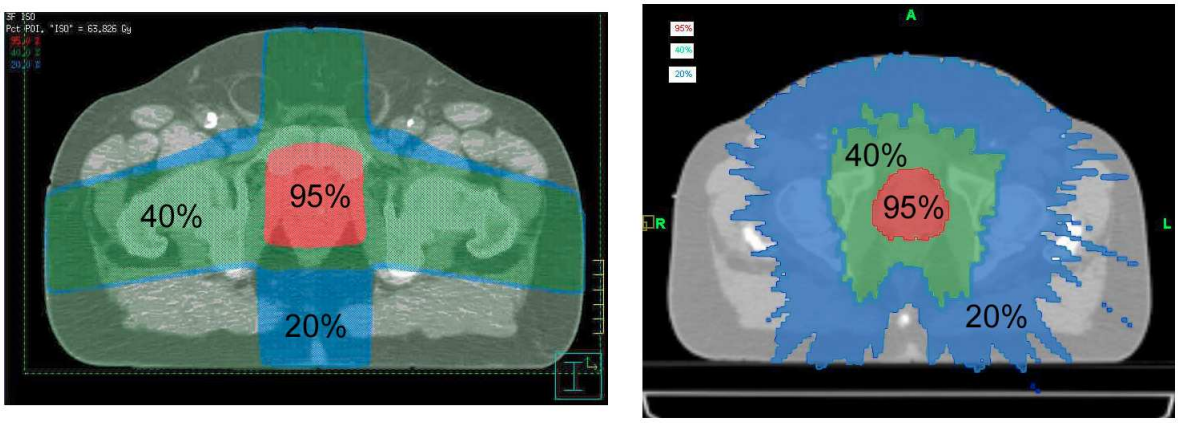

FIGURE 1.3: Isodose curves for a treatment of prostate cancer for conventional radiotherapy (left) and IMRT (right) in the axial plane [15]

Currently, IMRT is being used most extensively to treat cancers of the prostate, head and neck, and central nervous system. IMRT has also been used in limited situations to treat breast, thyroid, lung, as well as in gastrointestinal, gynecologic malignancies and certain types of sarcomas. IMRT may also be beneficial for treating pediatric malignancies.

A step further the IMRT consists in the new technique IGRT (image guided radiation therapy). This technique takes into account that tumours can move between treatment sessions due to changes in organ-filling or while breathing. There could also be variations in patients' position during day to day treatment session set up. From here, the need of developing a way to see the location of the tumour during the treatment delivery sessions. The change in the position of tumor can be tracked with a CT image, just before the treatment delivery and the appropriate corrections are made online. The imaging information from the "planned CT" scan done earlier is overlapped on this new CT image. IGRT further helps to improve the delivery of radiation. In some cases, tiny gold markers are implanted in or near the tumor to pinpoint it for IGRT. The technique of tracking the tumor during respiration and treating at a particular phase of breathing is called Gated or Breath Synchronized IGRT. This is also known as 4D IGRT (where the fourth dimension is the time).

1.4 Hadrons in therapy context: physical aspects

As stated before, the role of radiotherapy is to stop malignant cells from dividing, in order to prolong patient life. This is done trying to minimize the dose to healthy tissues for avoiding secondary complications.

Fig.1.4 shows the normalized absorbed dose curve for photon and proton beams as a function of the range in the tissue. The green curve represents the dose given to the normal tissue in front of the tumor volume, to the tumor and to the healthy tissues behind it when the treatment is performed with photons. The pink one represents a pristine Bragg peak for a single proton. However, in a treatment, in order to cover the whole tumor volume, several protons with different energies are shooting, forming the blue curve (called spread out Bragg peak, SOBP). Comparing the curves, the entrance dose given to the normal tissues is higher for photon beams. The dose at the tumour is higher when irradiated with protons and no exit dose after the tumor is delivered. Instead, photons show a tail which goes through the normal tissues behind the target which could lead to secondary clinical complications.

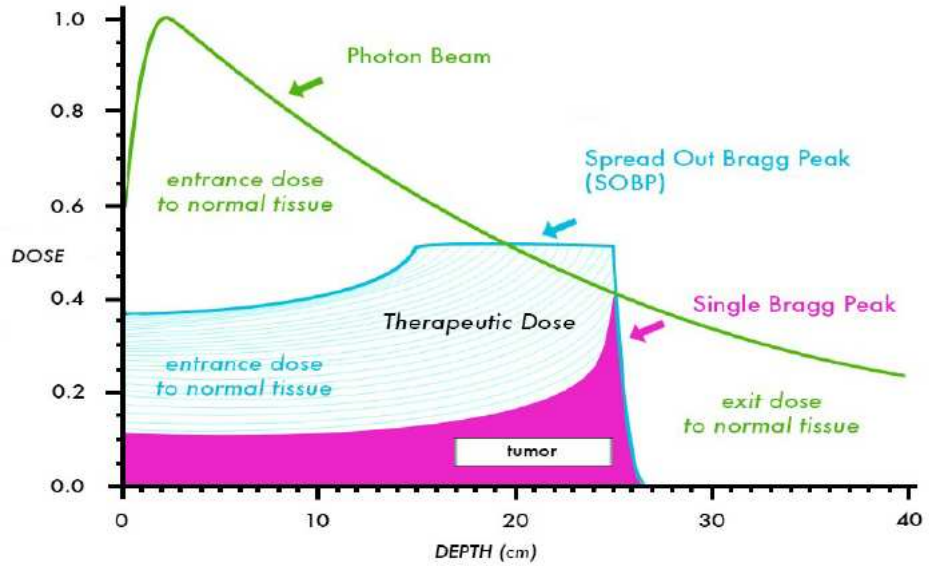

FIGURE 1.4: Normalized dose for photon and proton beams as a function of the range in the tissue.

A liver cancer treatment plan is presented in fig. 1.5 and shows the isodose curves comparing proton and photon treatments. Both modalities accomplish similar high-dose coverage of the clinical target volume (red outline), but the superior

controllability of the proton beam enables the physician to prevent most of the normal liver tissue from receiving low-dose irradiation in the IMRT plan.

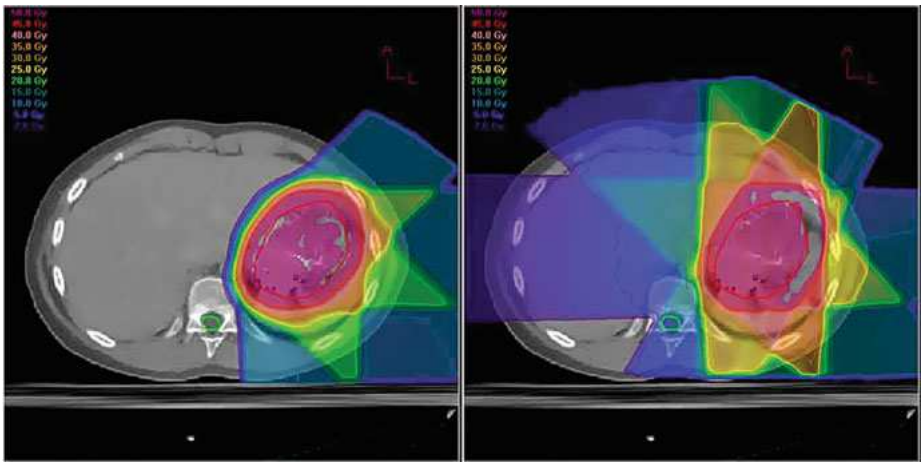

FIGURE 1.5: Comparison between a 3-field proton plan (left) and a 6-field IMRT plan (right) for treating a large liver cancer [16]

Another parameter must be taken into account for the success of a therapy: the biology effectiveness of the radiation. In some cases, conventional radiotherapy cannot to provide a successful treatment of the disease. Some tumor cells are resistant to radiation, thus, the scientific community started to look for particles with a higher biological effectiveness over photons or electrons. In this direction, negative pions and neutrons started to be employed to treat patients. But the expectations for an increase of biological effectiveness were not fulfilled in practice, so pions were abandoned as radiation for therapy, as well, neutrons, because of several side effects and the poor depth dose profile. A very good alternative is represented by heavy charged particles like protons or heavier ions. This is related to the way in which radiation causes damage to cells. In fact, since the discovery of the DNA and the genetic code in 1953, it became clear that the sensitive target in a cell is constituted by the DNA chain. When a cell is irradiated with an ionizing irradiation, a break in the DNA chain may occur such as: single-strand break, base loss, base modification, double-strand break. These facts can lead to different scenarios:

- the cell repairs error free;
- the cell repairs wrongly leading to cancerous cells;
- the cell dies.

Double-strand breaks are the most dangerous damages which can lead to error-repair or cell death. When a tumour is treated, it is desirable to lead its cells to death in order to stop its growth.

Ions (heavier than protons) show an increased relative biological effectiveness (RBE), being very useful to treat radioresistant malignancies. The elevated RBE is due to the increase in ionization density in the tracks of such particles, and the DNA damage becomes very difficult to repair [17].

However, because of the high RBE, the position of the ions inside the patient body must be known with high precision, since a small misalignment (of few mm) can lead to heavy damages (compared to a bad alignment with photons).

Physical and biology aspects of hadrons are discussed in Chapter 4 together with survival cell curves comparing irradiation with photons and protons.

Chapter 2

Interaction of radiation with matter: physical aspects and radiation dosimeters

This Chapter starts with a summary of the physical aspects of the interaction of radiation with matter followed by the definitions of some physical and dosimetric magnitudes. In particular, the discussion is limited to the radiation beams directly involved in this thesis work, making a distinction between the theoretical basis regarding radiotherapy with photon beams and the ones related to the physical and radio-biology studies performed with proton beams of low energy.

Then, the most used radiation dosimeters and their properties are discussed.

2.1 Theoretical basis

This section gives a summary of the theoretical basis regarding the interaction of radiation with matter.

It begins with the interaction of photons and electrons with matter; the subsections dedicated to "Kinetic energy released per unit mass, dose and electronic equilibrium" and the "Cavity theory" address the physical processes related the most to the characterization of the new system presented in Chapter 3 and used for treatment verification in photon therapy.

The interaction of heavy charged particles and the physical quantities: energy straggling, lateral beam spread, LET, stopping power and range are defined here because they essentially deal with Chapter 4 dedicated to the physical and radiobiology studies with low-energy protons.

2.1.1 Interaction of photons and electrons with matter

Photons interact with matter as follows: they transfer their energy to the atomic electrons of the medium and, subsequently, the electrons interact with the matter, by collisions or radiative processes. There are three main effects produced by photons in matter:

- Photoelectric effect: a photon is absorbed by an atomic electron, which is subsequently ejected from the atom with an energy of E= hν - B.E., where B. E. is the binding energy.
- Compton scattering consists on the scattering between the photon and a free electron. In matter, electrons are obviously binded to the atoms, but, if the photon energy is high compared to the B. E., this latter can be considered negligible and the electrons can be considered free.
- Pair production (energy threshold of 1.02 MeV): a photon is transformed in an electron-positron pair. In order to conserve the momentum, this phenomenon can be produced only in the presence of a third body (e. g. a nucleus) [18].

Fig. 2.1 shows the relative importance of these effects for photons in water.

Photons passing through a medium are not attenuated in energy but in intensity, because the three processes mentioned before remove the photon entirely from the beam by absorption or scattering. The law of absorption is thus :

$$-\frac{dI}{I} = \mu dx \tag{2.1}$$

where I is the intensity of the incident radiation, μ is the absorption coefficient and dx the thickness of the material.

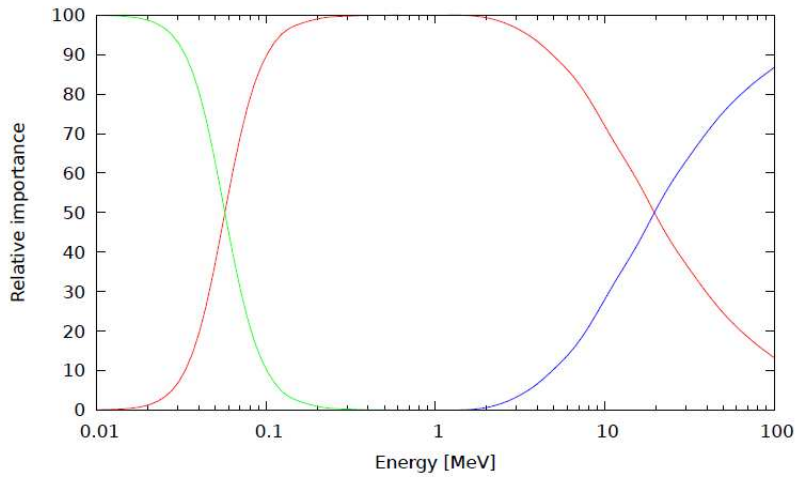

FIGURE 2.1: Plot of the relative importance of photoelectric effect (green curve), Compton (red curve) and pair production (blue curve) in function of the energy for photons in water. Figure taken from [7]

The clinical photon beam used for the measurements with the novel detector, studied in Chapter 3, is of 6 MV, thus, the Compton effect is the most probable in our case, which is responsible for the motion of secondary electrons in the medium.

In general, the energy loss of charged particles in matter is described by the inelastic collisions, in which, the energy of the particles is transferred to the atom, causing its ionization or excitation. The amount of energy transferred at each collision is a very small fraction of the total kinetic energy of the particles. The atomic collisions can be divided in two groups: hard (atom ionization) and soft collisions (only excitation as result). As the interaction of radiation with matter, the inelastic collisions are statistical in nature, occurring with a certain quantum mechanical probability. The number of interactions per unit of length is large, the fluctuations in the total energy loss are small and it is possible to work meaningfully with the average energy loss per unit path length [19].

As charged particles, electrons loose energy through collisional processes and, because of their small mass, the emission of electromagnetic radiation from scattering in the electric field of a nucleus (the so called bremsstralhung) plays an important role. Thus the total energy loss per unit of distance can be described as the sum of two contributions (collisional and radiative):

$$\frac{dE}{dx}_{tot} = \frac{dE}{dx}_{coll} + \frac{dE}{dx}_{rad} \tag{2.2}$$

which is also called stopping power S= dE/dx, with both radiative (S_{rad}) and collisional contributions (S_{coll}).

The stopping power in a medium is described in terms of mass stopping power, which is defined as the ratio between S over the density of the medium:

$$S_\rho = \frac{S}{\rho} \tag{2.3}$$

Another quantity of interest is the "range" of the particle which is the distance that the particle travels before stopping:

$$R = \int_{E_o}^{0} -\frac{dE}{S} \tag{2.4}$$

To describe the interaction of a particle beam with matter, some important magnitude must be introduced:

- fluence: total number of particles going through the area dA, orthogonal to the beam direction, ϕ= dN/dA;
- fluence rate (or flux): total number of particles crossing the area dA in a time dt, ϕ/dt= dN/(dA dt);
- energy fluence: total energy crossing the area dA:

$$\psi = \frac{dE}{dA}(E) \tag{2.5}$$

2.1.1.1 Kinetic energy released per unit mass, dose and electronic equilibrium

The KERMA (kinetic energy released per unit mass) is the energy transferred by the incident photon to the charged particles in an infinitesimal volume:

$$K = \frac{dE_{transf}}{dm} \tag{2.6}$$

KERMA is expressed in units of erg/g (rad) or J/kg (Gray).

The total KERMA is constituted by two contributions: collisional KERMA, K_{coll} and radiative KERMA, K_{rad}:

$$K_{tot} = K_{coll} + K_{rad} \tag{2.7}$$

The absorbed dose (unit Gray [1 Gy = 1 J/kg]) is defined (ICRU, 1993) as the mean energy dE_{abs} deposited by ionizing radiation in a mass element dm,

$$Dose = \frac{dE_{abs}}{dm} \tag{2.8}$$

the absorbed dose represents the contribution to the energy loss due to collisional processes $(dE/dx)_{coll}$.

Considering a photon beam, the absorbed energy is defined as the difference between the energy entering (E_{in}) a volume dV and the one leaving it (E_{out}), both for contributions of photons and electrons created in the volume:

$$dE_{abs} = (E_{\gamma in} - E_{\gamma out}) + (E_{e^- in} - E_{e^- out}) \tag{2.9}$$

thus, the dose is:

$$D = \frac{dE_{abs}}{dm} = \frac{(E_{\gamma in} - E_{\gamma out}) + (E_{e^- in} - E_{e^- out})}{dm} = K_{coll} + \frac{(E_{e^- in} - E_{e^- out})}{dm} \tag{2.10}$$

If the electronic equilibrium is achieved, for a particle entering the volume dV there is another one of the same type and energy which is leaving it, therefore $E_{e^- in} = E_{e^- out}$ and the D= K_{coll}. In general, the ratio between the dose and the KERMA is defined through a coefficient β.

Dose and KERMA are shown in fig. 2.2 as a function of depth in a medium, in the ideal case (electronic equilibrium achieved) and in the real case (no-electronic equilibrium).

In the first case, under the hypothesis that the photon beam is not attenuated as it passes through the medium, the KERMA does not show dependence on the depth in the medium, because the probability of a Compton scattering stays constant. At the surface, there is no electronic equilibrium: electrons are produced and the number of particles leaving the volume is greater than the ones entering it (build-up region). Thus the dose increases until a depth d of the same order of the range of the electrons (z_{max}): at this depth the electronic equilibrium is reached and the dose is constant and equal to the collision KERMA (fig. 2.2a).

In a real case, the photon beam suffers an attenuation as it passes through the medium and a complete electronic equilibrium is not achieved (fig. 2.2b). Thus, the probability for a Compton scatter decreases with the decrease of the number of photons N, and so does KERMA. This decrease is linear because $dN/dx \propto N(x)$, as follows by the exponential attenuation of photons. The absorbed dose increases for a depth $d \leq z_{max}$, reaches a maximum and, then decreases as KERMA. At a certain depth, KERMA is always a bit smaller than dose. This is again due to the attenuation law: since KERMA depends on the number N of photons at the depth d (N(d)) and the dose depends on the number of photons at a depth $d' \leq d$, due to the non-zero range of the electrons. Near the maximum, the so-called Transient Charged Particle Equilibrium (TCPE) is achieved [20].

2.1.1.2 Cavity theory

In order to perform dose measurements, a radiation sensitive device (dosimeter) must be introduced in the medium. This device introduces a perturbation, thus, the dose it measures does not correspond to the energy that would be absorbed in the same portion of medium in the absence of the dosimeter. The correspondence between the dose absorbed by the dosimeter and the dose in the medium if it was not present is given by cavity theory.

On the basis of the comparison between the range of the secondary electrons produced (d) and the cavity dimension (R), three main cases can be distinguished, whether only secondary electrons should be considered or also perturbations due to the primary particles:

- $d \ll R$, Bragg cavity conditions: the interactions in the cavity are mostly due to the secondary electrons produced outside of it;

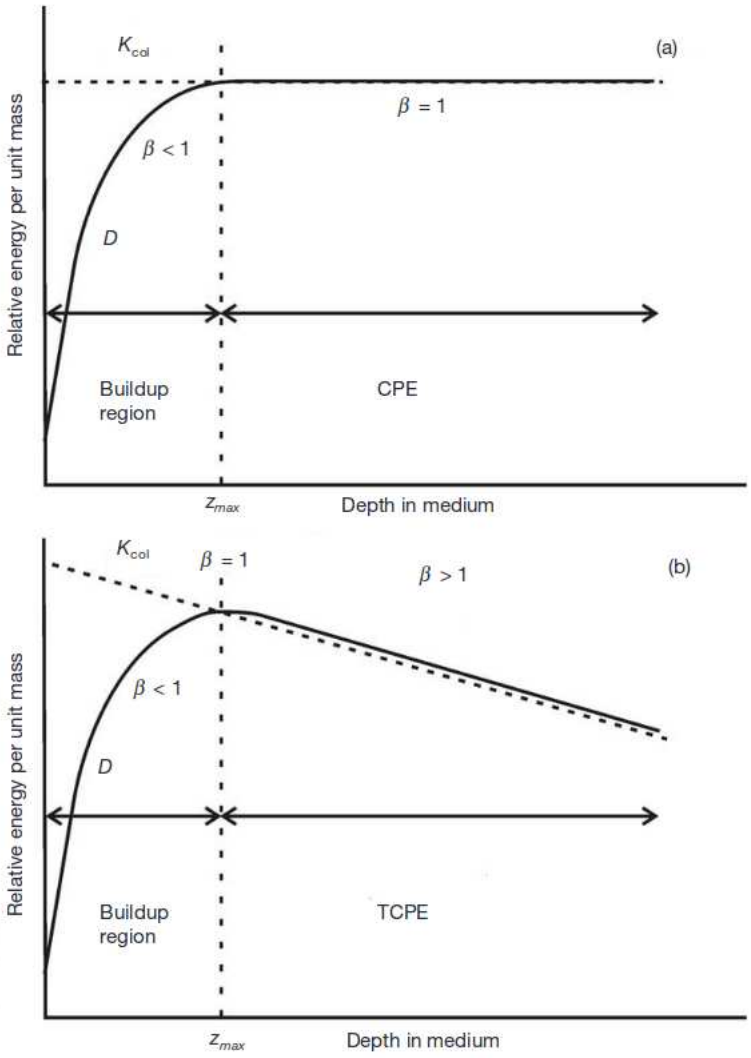

FIGURE 2.2: Dose and KERMA curves in function of the depth in a medium. a) Electronic equilibrium achieved. b) Real case, no electronic equilibrium. Taken from [20]

- d $\gg$ R, electronic equilibrium: the contributions to the absorbed dose are due to the electrons produced inside the cavity;
- d $\simeq$ R, Burlin theory: both electrons produced inside and outside the cavity contribute to the dose.

Two general hypotheses are contemplated: the materials which constitute both the cavity and the surrounding medium are considered homogeneous, and, the primary particle field is considered uniform in the cavity and in the surrounding medium. If the photon field is taken into account a correction factor must be added in the description.

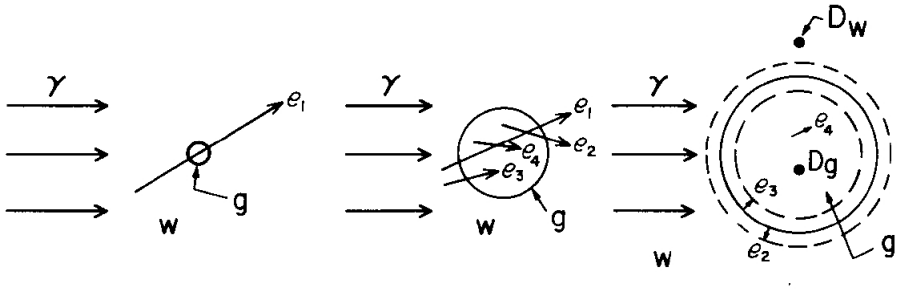

FIGURE 2.3: From left to right: Draft of a small, intermediate and big cavity in a photon field. Taken from [20]

Bragg cavity theory for small cavities:

the cavity dimension is small enough to not perturb the particle field, thus, the particle fluence is considered equal outside and inside the cavity. The small cavity theory, moreover, assumes that any backscattered particle field produced at the interface between the cavity and the surrounding medium can be considered negligible. In addition, the dose contribution is only given to the charged particles crossing it and no secondary particles are produced or stopped in the cavity, reaching the electronic equilibrium conditions inside of it. No δ-electrons or bremsstralhung photons are produced and the energy release in the cavity is considered as a continuous process (continuous slowing-down approximation, CSDA).

Under these conditions, the dose is:

$$D_{m,c} = K_{m,c}^{coll} = (\frac{S(E)}{\rho})_{m,c}\Phi(E) \mid_{E=E_{e-}} \tag{2.11}$$

where Φ is the charged particle fluence and S/ρ is the mass stopping power (as defined in eq. 2.3) , both calculated at an energy E equal to that of the incoming electrons. Typically this equation must be integrated on the energy spectrum of the electrons, since, commonly, they are not monoenergetic:

$$D_{m,c} = \int_{\sigma(E)} (\frac{S(E)}{\rho})_{m,c}\Phi(E) = \Phi_{tot}(\frac{\bar{S}}{\rho})_{m,c} \tag{2.12}$$

where Φ_{tot} is the total fluence and $\bar{S}/\rho$ is the average mass collision stopping power. Thus the ratio between the dose in the medium and the dose in the cavity can be described as the ratio between the two mass collisional stopping powers:

$$\frac{D_m}{D_c} = \frac{(\frac{\bar{S}}{\rho})_m}{(\frac{\bar{S}}{\rho})_c} = (\frac{\bar{S}}{\rho})_{m,c} \tag{2.13}$$

The big cavity theory assumes that the dose contribution is given to the photon field inside the cavity. The particle contribution produced at the interface with the outside medium can be neglected. Hence, the electrons produced outside the cavity are a small fraction and they do not contribute significantly to the absorbed dose. The electronic equilibrium is achieved inside the cavity and the absorbed dose is due to the collisional KERMA:

$$\frac{D_m}{D_c} = \frac{K^m_{coll}}{K^c_{coll}} = (\frac{\bar{\mu}_{abs}}{\rho})_{m,c} \tag{2.14}$$

For describing the intermediate case, Burlin theory must be adopted. This theory makes several approximations:

- The materials of the cavity and the medium are considered homogeneous.
- The photon field is uniform inside and outside the cavity and it is not perturbed by the discontinuity between the media.
- Charged-particle equilibrium is achieved in the cavity and in the surrounding medium.
- The secondary electron spectrum can be considered the same outside and inside the cavity.
- The electron fluence entering the cavity is attenuated along the cavity exponentially without changing its energy.
- The electron fluence inside the cavity grows exponentially with the distance until it reaches its equilibrium value.

If all the hypothesis are satisfied, then the relation for the Burlin's theory is:

$$\frac{D_m}{D_c} = d(\frac{\bar{S}}{\rho})_{m,c} + (1-d)(\frac{\bar{\mu}_{abs}}{\rho})_{m,c} \tag{2.15}$$

where d is a parameter which represents the cavity size. When d approaches 0, we are in the big cavity approximation, while, if d is close to 1, the Bragg theory can be used.

In the real case, many correction factors must be added to the cavity theory to have a complete description of a real dosimeter, such as:

- Corrections for the attenuation of the photon field with the depth in the medium (fluence factor).
- A dose gradient factor must be included to describe any inhomogeneities in the dose distribution inside the cavity.
- Wall correction factor, which includes the discontinuities in the interface between the cavity and the surrounding medium and the contribution of the backscattered particles.
- Temperature and density factors: changes in the temperature, pressure or density can affect the measurements (cavity filled with gas).

2.1.2 Interaction of heavy charged particles with matter

As for the electrons, the passage of heavy charged particles in matter is described by the stopping power. In the case of heavy charged particles, inelastic collisions are the solely responsible for the energy loss, thus the radiative contribution can be neglected in the description.

A semi-classical description of this process was given for the first time by Bohr. Formula 2.16, known as the Bethe-Bloch formula, adds quantum corrections to the Bohr's theory:

$$\frac{dE}{dx} = \frac{4\pi e^4 Z_t Z_p^2}{m_e v^2}\left[ln\frac{2m_e v^2}{< I >} - ln(1-\beta^2) - \beta^2 - \frac{C}{Z_t} - \frac{\delta}{2}\right] \tag{2.16}$$

where Z_p and Z_t denote the nuclear charges of the projectile and target, m_e and e are the mass and charge of the electron, v is the particle velocity, $< I >$ is the

mean ionization energy of the target atom or molecule, β = v/c, C/Z_t represents the shell correction term and $\delta/2$ is the density effect correction term [21]. Due to the $1/\beta^2$ dependence the energy loss increases with the decrease of the particle kinetic energy. At high velocities the atomic electrons are completely stripped off and the projectile charge is equal to the atomic charge number Z_p.

At lower velocities (for light ions below about 10 MeV/u), the mean charge state decreases due to the interplay of ionization and recombination processes and Z_p in eq. 2.16 has to be replaced by the effective charge Z_{eff}, which can be described by the empirical formula [21]:

$$Z_{eff} = Z_p(1 - exp(-125\beta Z_p^{\frac{2}{3}})) \tag{2.17}$$

When a beam of heavy charged particles slows down in matter, its energy loss changes with the changes of its kinetic energy. The energy loss increases with the depth in the medium until it reaches a maximum at the end of the particles' path in the medium, and then is followed by an abrupt fall. As will be explained in Chapter 4, this behavior makes charged particles attractive in tumor treatments.

2.1.2.1 Energy Straggling

A mono-energetic particle beam, after passing through a material, shows statistical fluctuations of the energy loss. This is due to the large number of collisions in the slowing-down process. This results in a broadening of the Bragg peak [18].

These fluctuations are described by the asymmetric Vavilov distribution ([22]) for charged particles through a thin layer of matter (energy-loss straggling). In the limit of many collisions the Vavilov distribution becomes a Gaussian [23], [24]:

$$f(\Delta E) = \frac{1}{\sqrt{2\pi\sigma}} exp \frac{(\Delta E - \langle \Delta E \rangle)^2}{2\sigma^2} \tag{2.18}$$

where

$$\sigma = 4\pi Z_{eff} Z_t e^4 N \Delta x \left(\frac{1 - \frac{\beta^2}{2}}{1 - \beta^2} \right) \tag{2.19}$$

2.1.2.2 Lateral beam spread

Charged particles, as they pass through matter, suffer elastic Coulomb scattering; this leads to a lateral spread of the particle beam, which is well described by the Rutherford formula [18]:

$$\frac{d\sigma}{d\Omega} = Z^2 Z_p^2 r_e^2 \frac{mc/\beta\rho}{4sin^4(\theta/2)} \tag{2.20}$$

Because of its $1/\sin^4(\theta/2)$ dependence, the particle angular deflection is small. In general, the Coulomb interactions can be described distinguishing three main cases:

- Single scattering: if the absorber is very thin, the probability that more than one single scattering will occur is small and the angular distribution is given by formula 2.20.
- Plural scattering: if the average number of collisions is N $<$ 20, we have plural scattering. This is the most difficult case to describe since nor formula 2.20 or statistical methods can be applied.
- Multiple scattering: if the average number of scatterings is N $>$ 20, the problem can be treated statistically. The probability distribution for the angle deflection is described as a function of the thickness of the absorber.

At small incident angles, the particle distribution for a beam of ions is approximated to a Gaussian function f_α with a standard deviation given by eq. 2.22:

$$f_\alpha = \frac{1}{\sqrt{2\pi\sigma_\alpha}} exp(-\frac{\alpha^2}{2\sigma_\alpha}) \tag{2.21}$$

$$\sigma_\alpha = \frac{14.1MeV}{\beta pc} Z_p \sqrt{\frac{d}{L_{rad}}} \left(1 + \frac{1}{9} log_{10} \frac{d}{L_{rad}}\right) \tag{2.22}$$

where σ_α is the standard deviation, p the momentum, L_{rad} the radiation length and d the thickness of the material [21].

2.1.2.3 Linear energy transfer

LET (linear energy transfer) is a unique function of kinetic energy for a given type of particle and represents an important physical quantity in radiation biology.

Here we report the definition of LET given by the ICRU (International commission on radiation units) in 1968: the linear energy transfer or restricted linear collision stopping power (L_Δ) of charged particles in a medium is the quotient of dE by dl, where dl is the distance transversed by the particle and dE is the mean-energy loss due to the collisions with energy transfers less than some specified value Δ.

$$L_\Delta = \left(\frac{dE}{dl}\right)_\Delta \tag{2.23}$$

According to this definition, L_{100}, is the LET when $\Delta = 100$ eV. The quantity L_∞ indicates the case in which all the energy is transferred.

2.2 Radiation dosimeters: a brief overview and state of the art

A radiation dosimeter is a device, instrument or system that measures or evaluates the absorbed dose or the related quantities of ionizing radiation. A dosimeter with its reader forms a dosimetry system. An instrument can be considered and used as a dosimeter if: it owns at least one physical property that is a function of the measured dosimetry quantity; and if with proper calibration, can be used for radiation dosimetry. Ideal radiation dosimeter must have the following properties: a linear response to the dose received, energy independence and high spatial resolution.

Fig. 2.4 shows the behavior of two different radiation dosimeters in function of the dose received. Such systems present a linear response at low doses. The non-linear behavior, if the dosimeter response is not saturated, can be corrected with a proper calibration.

Dosimeters are generally calibrated for a specified radiation beam and used over a wide energy range. The dosimeter, however, gives a readout 'r' which is proportional to the absorbed dose of the dosimeter itself. In general, this is not what one

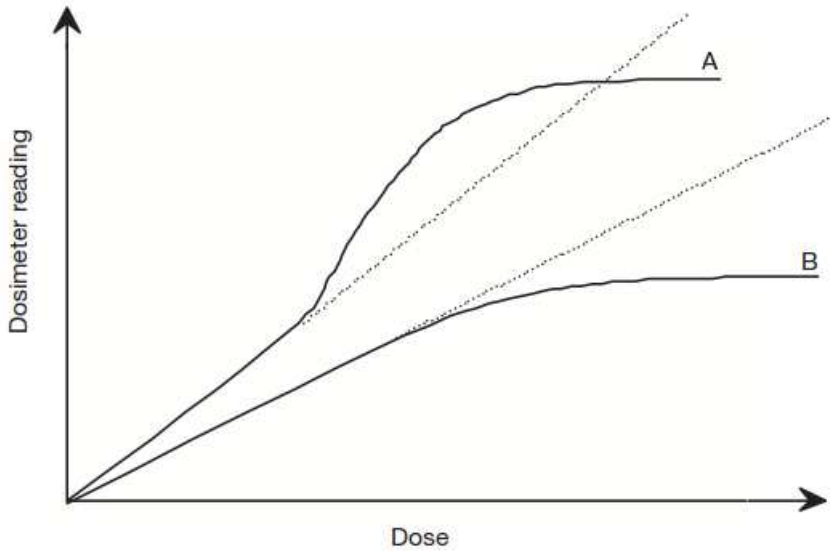

FIGURE 2.4: Response of two dosimetry systems. Curve A exhibits linearity with dose, then supra-linear behavior and finally saturation. Curve B is linear at the beginning and then saturated at high doses. Taken from [25]

is looking for; instead, it is important to know which would be the absorbed dose in the surrounding medium D_m if the detector was not present.

The calibration consists in finding the proportionally factor between 'r'and D_m. The cavity theory, described in the previous sub-section, gives the prescriptions in order to find such factors. However the application of this theory is not straightforward, thus, usually, the measurement taken with the system that one wants to calibrate are compared with the ones measured by another system, previously calibrated with other means, in referenced conditions.

In a dosimeter, the dose-dependent magnitude can be charge, heat, light, change in the optical or chemical property of the material.

In this section the most common detectors used as dosimeters will be described with a special focus on radiochromic films and silicon detectors, which were the most used in this thesis work.

2.2.1 Radiochromic films

An accurate dose determination and a precise dose delivery to the tumor are directly associated with better treatment outcomes in terms of higher tumor control and lower post treatment complications. Numerous problems are associated to the iso-dose curves and depth-dose distributions with conventional 2D radiation detectors. Ionization chambers and semiconductor detectors do not provide sufficient spatial resolution for many treatment plans. Thermoluminescent dosimeters are cumbersome and time consuming. Radiographic films have high spatial resolution compared to other detectors, but they show large differences in sensitivity for photon energies between 10-200 keV. Moreover they present difficult handling, since they require wet chemical processing and are sensitive to light.

Over the years, film dosimetry was developed into a powerful tool for radiotherapy treatment verification and quality assurance.

Radiochromic films offer high spatial resolutions, weak energy dependence for electrons and photon beams used in radiation therapy and near tissue equivalence (they are composed by 9.0 % hydrogen, 60.6 % carbon, 11.2 % nitrogen and 19.2 % oxygen). For all these reasons, they have been considered a valid alternative to conventional 2D radiation detectors and this makes them suitable for dose measurements [26].

In this section, a brief overview of the development of radiochromic films is given, describing how their characteristics changed over the years, comparing the models that were developed until the last one, which was used in this thesis work.

2.2.1.1 Historical background and chemical makeup

First films, made of papers and special gels, were used for imaging in the mid-1800s. A very early radiochromic process, demonstrated in 1826 by Niepce, was obtained with an unsaturated hydrocarbon polymeric mixture based on bitumen that cross links upon irradiation leaving a light-scattering pattern. Other technology of films based on organic image-forming system involving cis-trans isomeric conversions were employed for high-dose radiation dosimeters (10^4- 10^6 Gy), but they were not sensitive enough for clinical or radiobiological applications. Films based on triphenyl tetrazolium chloride (TTC) salts were used for biological applications

in aqueous gels for mapping ionizing radiation dose distribution. These salts are colorless in aqueous solutions but upon irradiation become highly colored.

In order to be able to use films for medical application, a new form based on polydiacetylene was developed. At the beginning, two main types were created: GafChromic DM-1260 (also known as HD-810) and GafChromic MD-55, for absorbed doses of 50-2500 Gy and 10-100 Gy respectively. These films are colorless before irradiation and consist of a thin, active microcrystalline monomeric dispersion coated on a flexible polyester base. They turn progressively blue upon exposure to ionizing radiation. Their technical features are:

- GafChromic HD-810 purchased from the manufacturer International Specialty Products (ISP, Wayne, NJ) available in 20 cm x 25 cm clear sheets, used for dose mapping of 50-2500 Gy, formed by a 7 μm thick radiation sensitive layer on a 100 μm polyester base,
- Double-layer GafChromic MD-55-2 purchased from the manufacturer International Specialty Products (ISP, Wayne, NJ), in 12.5 cm x 12.5 cm clear sheets, used for dose range of 3-100 Gy. They are made of layers of highly uniform transparent coating, sensitive to ionizing radiation, on a polyester base (fig. 2.5) [27].

Nowadays the sensitive structure of these films has been changed. To avoid confusion and to be able to compare results, it is useful to recognize manufacturer's stated lot number for a given type of film.

Further radiochromic film developments lead to the EBT (External Beam Theraphy) GafChromic models designed to be applied in intensity modulated radiotherapy (IMRT) quality assurance (QA) protocols. The EBT films have been studied and characterized for dose measurements using flat bed scanners and analyzing the images in the red channel (extracted from the RGB (Red-Green-Blue) scanned images), which has the highest absorption spectrum for clinical dose ranges (0.25-40 Gy) [26]. EBT films differ from the previous models in the composition of the active layer, which leads to an increased sensitivity. Sensitivity in film dosimetry is defined as the ratio of the change in optical density and the amount of dose which causes that change. It is measured at the maximum absorbance wavelength (673 nm for HS-810 and 635 for EBT) achieved by modifying the composition of the active layer. As reported in [28], EBT model can be used to measure dose ranges

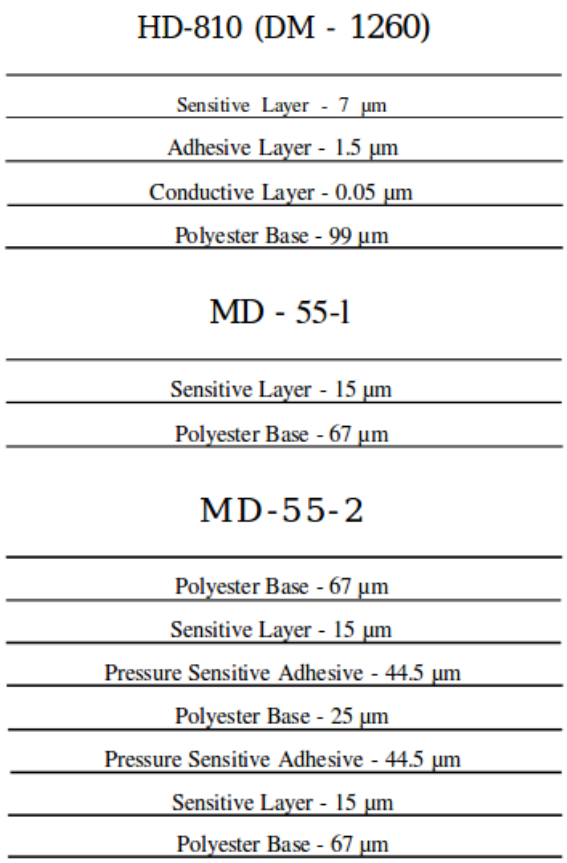

FIGURE 2.5: Transversal section of HD-810, MD-55-1 and MD-55-2 GafChromic films.

from 0.2 to 100 Gy with an uncertainty better than 2 %. An important source of uncertainties is due to the non-uniformity of the sensitive layer. For EBT, the non-uniformity was reduced to a 2 % whereas previous models showed 10-15 % for MD-55 and 6-8 % for HD-810 [29]. A further improvement of the film uniformity was obtained introducing a yellow dye to the sensitive layer (model EBT2), which showed an acceptable uncertainty for clinical applications. The addition of the dye aims to correct for subtle differences in the thickness of the active layer. It is also assumed that this dye does not affect the film optical density when exposed to radiation. EBT2 model is made by combining clear polyester over-laminate (175 μm thick) with active film coating (30 μm nominally thick) over which a topcoat of 5 μm is applied. Another substrate of polyester of 50 μm is bounded to the topcoat with 25 μm of pressure-sensitive adhesive (fig. 2.6). Since the structure of this model is not symmetric, the manufacturer started to make a small cut of the upper right corner indicating the top surface of the sheet.

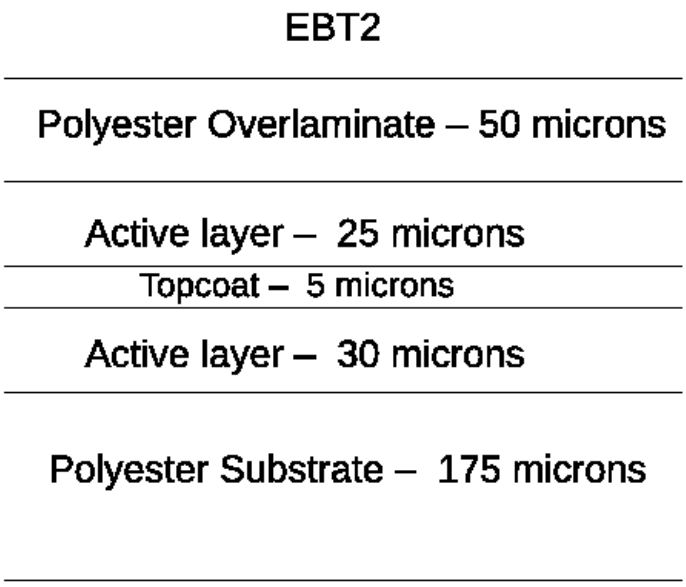

FIGURE 2.6: Transversal section of an EBT2 GafChromic film.

This difficulty of keeping track of which side has been irradiated is overcome with the latest technology of radiochromic films: the EBT3 GafChromic model. Such films present the same structure of the EBT2 but their composition is symmetric: they are constituted by two polyester layers of 125 μm sandwiching the active layer of 28 μm.

2.2.1.2 Dosimetry with GafChromic films

In general, the radiochromic reaction is a solid-state polymerization, where the film turns deep blue proportionally to the radiation dose. The response of the radiochromic film needs to be converted into absorbed dose values. For each film model a protocol for the calibration has to be established. The standard way is to use a reference dosimeter (generally ionization chambers or thermo-luminescent detectors (TLDs)), which relies on a calibration factor or calibration curve that was determined in a reference beam quality of a known dose output (see paragraph 3.1.3). Dose response of an absolute dosimeter is directly used to calculate dose at a given point of measurement. The film response in dose is expressed in terms of change in its optical density, netOD (before and after the irradiation), which is generally defined as:

$$netOD = -\log I/I_o \tag{2.24}$$

where I is the intensity of the color value after the irradiation and I_o is the value before the irradiation. The dose is plotted as function of the measured netOD and then the data are fitted with an appropriate function using the method of the least squares

$$D = f_1(netOD) \tag{2.25}$$

where f_1 is a function which correlates the two magnitudes. The reference radiochromic film dosimetry protocol is established to measure absolute dose of a plane dose distribution in an IMRT plan using the red channel of the scanned image acquired in the three color channels (red green and blue, RGB). However, one has to bear in mind that while designing the protocol for an actual radiochromic film dosimetry system, a number of effects that could affect the response of the film must be taken into account. As Rink et al. showed in their work [30], a temperature change from 22 °C to 38 °C can affect the dose response because of a shifting in the absorbance spectrum of the maximum absorption peak from 636 nm to 630 nm. Moreover, careful attention has to be paid in the post irradiation analysis: the recommendations given by the manufacturer stated that for an optimal scanning procedure the film should be scanned after 24h of irradiation. Although the constant growth in optical densities can be neglected in most of the contemporary film dosimetry protocols, scanning irradiated film pieces after excessive periods of time (several months), if not corrected, could lead to significant uncertainties [26].

2.2.2 Silicon detectors: working principle

For charged particle detection, silicon is the most widely used semiconductor material [18]. It is possible to dope the silicon by means of special defect atoms creating the n-type and p-type silicon (one exceeding in donors and another in acceptors of electrons).

A junction between p- and n-type silicon creates a diode. Special techniques are used to achieve the creation of a junction. One method, for example, is to diffuse sufficient p-type impurities into a homogeneous bar of n-type material so as to change that end into a p-type semiconductor. The formation of p-n junction

creates a special zone at the interface between the two materials. Because of the difference in the concentration of electrons and holes between the two materials, there is an initial diffusion of holes towards the n-region and of electrons towards the p-region. Thus, the electrons fill up holes in the p-region while the diffusing holes capture electrons in the n-side. N and p regions are initially neutral, but this recombination causes a charge build-up at the sides of the junction. Since the p-region is injected with electrons it becomes negative, while, the n-side positive. This creates an electric field gradient along the junction which gives rise to a potential difference across the junction. The region of potential change is known as depletion zone. The depletion area is the sensitive region of the junction to the passage of charged particles.

When a reverse bias voltage is applied, the potential barrier in the junction becomes higher and so the diffusion; the recombination current is suppressed and the depletion zone is growing. When radiation traverses the silicon, it produces ionizing and non-ionizing energy loss. The non-ionizing energy loss creates radiation damages, while the ionization loss causes the creation of electron-hole pairs which produce the signal (fig. 2.7).

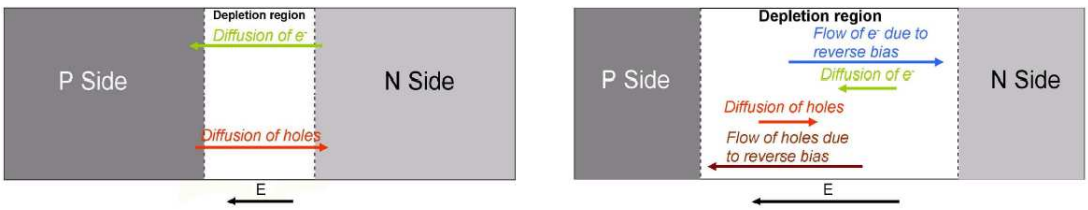

FIGURE 2.7: PN junction. Left: no bias is applied; right: junction biased at a voltage V creating a depletion zone. Taken from [2]

In order to obtain spatial resolution the p implantation of a simple p on n diode can be structured (the so-called single sided p on n detector). It is also possible to add a n+ implantation on the n-side of the diode. The result is a double sided detector that can measure two independent projections.

2.2.2.1 Silicon diode dosimeters

Silicon diode dosimeters are made of p-n junction diodes. Diodes usually employed in radiotherapy are p-n type because they are less affected by radiation damage

and present a small dark current; diodes are used as relative dosimeters. They are very sensitive and small in size and are particularly useful for measurements in phantom with small field or high dose gradient area. They are also widely used for in vivo dosimetry on patients. They are provided inside a specific encapsulation to protect them from physical damage. However diodes need to be calibrated when used for in vivo dosimetry and several correction factors must be taken into account. Since they suffer the radiation damage, their calibration has to be repeated often. Their response in dose is also temperature, energy and direction dependent.

Some of these disadvantages are overcome with the MOSFET (metal-oxide semiconductor field effect transistor), a miniature silicon transistor which possesses excellent spatial resolution, small size (small beam attenuation) and is particularly used for in vivo dosimetry. The MOSFET threshold voltage is a linear function of the absorbed dose; when an ionizing radiation penetrates the oxide, it generates permanently trapped charges, which cause a change in the threshold voltage proportional to the absorbed dose.

2.2.2.2 Silicon Strip detectors

Strip detectors are the most common structures used on silicon. Strips could have any form and can be wound arbitrarily over the detector if necessary, but strips equally spaced are the most employed ones. The most common pitch dimensions vary from 20 to 250 μm, according to the application.

2.2.2.3 Pads and Pixels

Pads and pixels are structures commonly used in single-sided detectors. A pixel is a small pad. Common pixel dimensions go from (50 $\times$ 50) μm^2 to (200 $\times$ 200) μm^2, while pads (200 $\times$ 200) μm^2 to few mm^2. In principle one can construct any shape of pixels or pads but the most common way is to use rectangular shapes. A special case of pixel detectors are the CCDs (charge-coupled devices).

Many efforts have been done to develop silicon detectors for medical applications, taking advantage of the experience and advances earned in detector technology from nuclear physics research (i.e. tracking silicon detectors, electronics and data acquisition systems). In particular, research is oriented towards silicon strip/pixel

technology to improve spatial resolution for complex radiotherapy verification. As a matter of fact, silicon pixel detectors were developed to obtain good spatial resolutions, such as MAESTRO [31], DOSI [32], and CMRP DMG detectors [33]. They require a high number of allocated channels and complex multichannel readout electronics based on application specific integrated circuits (ASIC) coupled directly to the detection system. This can produce some inconveniences due to the sensitivity of ASICs to radiation. In addition, these systems are not suitable to obtain dose maps in axial planes, which are generally oriented parallel to the beam axis. In fact, many of them are designed to be irradiated only perpendicularly with respect to detector active area. This means that they are useful for verifying separately each treatment field but not the full plan.

2.2.2.4 Dual chip silicon detector for dosimetry

Within this scenario, a novel solution using a single sided silicon strip detector (SSSSD) was developed and its feasibility to obtain two-dimensional (2D) axial dose maps in radiotherapy treatments was studied [6]; concretely, the model used was a 16-strip design W1(SS)-500 from Micron Semiconductor Ltd. The detector was placed at the axial plane of a cylindrical rotating phantom and the whole system was irradiated under clinical conditions by a Siemens linac installed at the Virgen Macarena Hospital in Seville (Spain). After successful results using the W1(SS)-500, we present the development of a more advanced prototype. The aim is to improve the traditional devices and to verify in a simple, fast and accurate way, a complete radiotherapy treatment. The new system allows to obtain a 2D axial dose map with higher resolution than the previous detector and with half of the acquisition time because of its novel design (two strip detectors mounted together, each one with the strips in a direction perpendicular to the other). The characteristics and the results obtained with this system are presented in Chapter 3.

2.2.3 Ionization chambers

Ionization chambers (ICs) are the simplest gas-filled detectors. They are used in radiotherapy and in diagnostic radiology to measure the radiation dose.

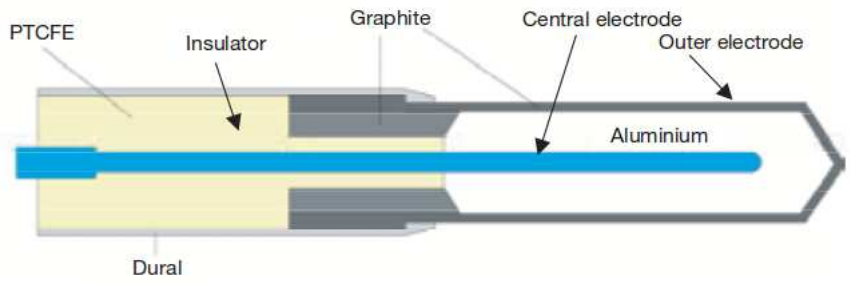

FIGURE 2.8: Scheme of a Farmer type IC. In the picture, the materials used as electrodes, walls and insulators are also described. Adapted from [25]

Their operation principle consists of the collection of all the charges created when a radiation ionizes the gas contained in the chamber. The number of electron-ion pairs created is proportional to the energy deposited by the incident radiation. Under the action of an applied electric field the electrons created are accelerated towards an anode and the ions towards a cathode. The current signal observed depends on the voltage V applied. As the voltage increases, the electron-ion pairs are collected before they can recombine. When the voltage V reaches a value for which all the pairs are collected, the detector is working in ionization chamber regime.

The basic configuration is a container filled with gas with conductive walls and thin end windows with a central collecting electrode. The walls are separated from the electrode by an insulator which also reduces the leakage current when the chamber is polarized. Generally, ICs are equipped with a guard electrode which further reduces the leakage current and improves the field uniformity in the sensitive volume, thus, facilitating the charge collection. Ionization chambers are commonly used to measure γ-ray exposure and as monitoring instruments for large fluxes of radiation. The signal current is normally very small and needs to be measured with an electrometer (able to measure current of the order of 10^{-9}A or less). Ionization chambers working in open air require measurement corrections which include temperature and pressure corrections to account for changes in the mass of the air inside the chamber.

Fig. 2.8 represents the most popular cylindrical type of ionization chamber used in radiotherapy dosimetry, called "thimble chamber", designed by Farmer and

originally manufactured by Baldwin. Its sensitive volume resembles a thimble (hence its name) and generally they have a volume between 0.1 and 1 cm^3, with a typical length $\leq$ 25 mm and a diameter $\leq$ 7 mm. The walls are constructed with low atomic number material and its construction is made as homogeneous as possible; for its calibration in air, a ^{60}Co radiation source is used. The Farmer type ionization chamber data were used in this thesis work as comparison with the data collected by the new treatment verification system and are shown in the next sections.

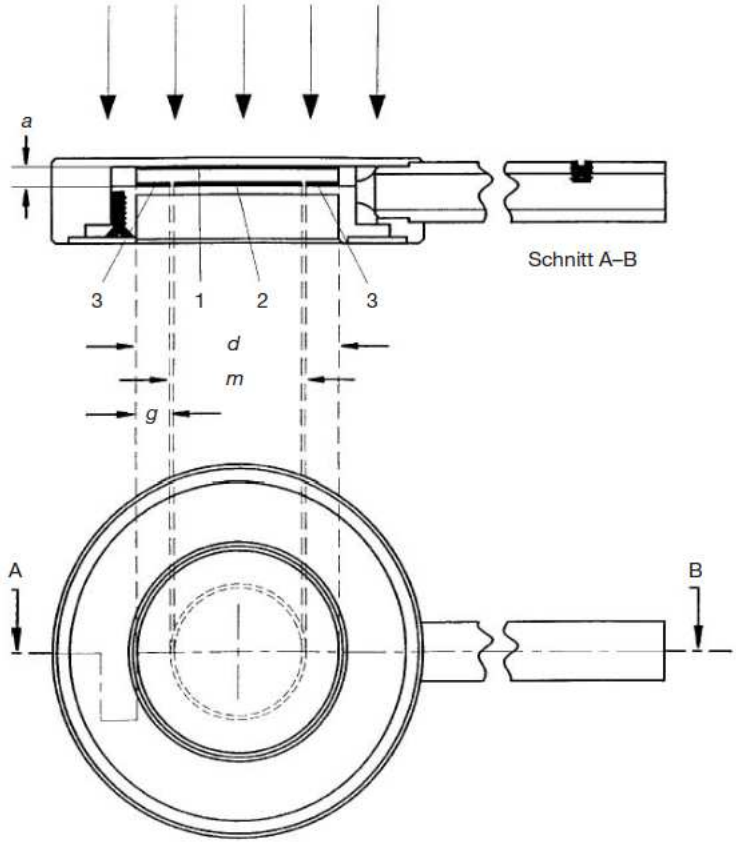

FIGURE 2.9: Parallel-plate ionization chamber scheme. 1: polarizing electrode. 2: collecting electrode. 3: guard ring. a: height (electrode separation) of the air cavity. d: diameter of the polarizing electrode. m: diameter of the collecting electrode. g: width of the guard ring; figure taken from [25]

Parallel-plate ICs are usually made of two plane walls, one used as entry window and polarizing electrode and the other as back wall and collecting electrode, as

well as guard ring system. A scheme of a parallel-plate model is shown in fig. 2.9. Back walls are constituted by conducting plastic or non-conducting material with a thin conducting layer of graphite forming the collecting electrode and the guard ring at the top. A special parallel-plate IC, constructed at GSI laboratories, was used within this research work and its application is exposed in section 4.2.2.2.

Other types of parallel-plate ICs are the extrapolation chambers, which have a variable sensitive volume and are used in measurements of surface doses in orthovoltage and megavoltage X-ray beams and in the dosimetry of β particles and low energy X-rays. The variable volume allows to calculate the cavity perturbation introduced by the IC itself in the beam field.

2.2.4 Luminescence dosimeters

Some materials can absorb radiation and retain a part of the energy in metastable states. When this energy is emitted as ultraviolet, infrared or visible light, this phenomenon is called luminescence. Depending on the time delay between stimulation and emission we can distinguish between fluorescence (time delay between 10^{-10}s and 10^{-8}s) and phosphorescence (time delay greater than 10^{-8}s). Such materials have storage traps and recombination centers, located in the energy gap band (between the valence band and the conduction band), characterized by a specific activation energy which depends on the crystalline solid and nature of the trap. When the material is stimulated, secondary charged particles (produced in primary interaction of photons with the material) create numerous low energy free electrons and holes through the ionization of the atoms. They can recombine or become trapped in an electron or hole trap. The free charges trapped can be released by heating (giving place to the thermoluminescence process) or by light irradiation (optical stimulated luminescence).

If the exciting agent is heat, the material is called thermoluminescent. A dosimeter made of such material is called a thermoluminescent dosimeter (TLD). The TLDs most commonly used in medical applications are LiF:Mg,Ti, LiF:Mg,Cu,P and $Li_2B_4O_7$ because of their tissue equivalence [25]. The thermoluminescence emission can be correlated with dose through proper calibration. The dose response for these devices is linear over a wide range of doses used in radiotherapy, although they exhibit a supralinear behavior for high doses before saturating. TLDs are used for in vivo dosimetry on patients, in quality assurance procedures, for dose

monitoring and for verification of treatment techniques in various phantoms. In table 2.1, we summarize the main advantages and disadvantages of the most commonly used dosimeters.

	Advantages	Disadvantages
Ionization Chamber (IC)	Allow beam calibration; instant readout	Connecting cables; high voltage supply required
Film	2-D spatial resolution; very thin: does not perturb the beam	Tools and softwares required for processing. Proper calibration is needed; energy dependency problems
Diode	Small size; high sensitivity; instant readout; no external bias voltage; simple instrumentation	Requires connecting cables; variability of calibration with temperature; change in sensitivity with accumulated dose; special care needed to ensure constancy of response.
TLD	Small in size; available in various forms; some are reasonably tissue equivalent; not expensive	Signal erased during readout; no instant readout; accurate results require care; readout and calibration time consuming; not recommended for beam calibration.

TABLE 2.1: Advantages and disadvantages of the most commonly used dosimetric systems. Adapted from [25]

2.2.5 Other types of dosimeters

Here, some other technologies of dosimeters are listed. More details can be found in [25].

2.2.5.1 Plastic scintillators

Plastic scintillators are starting to be used in radiotherapy dosimetry because of their numerous advantages: they can be very small (1 mm^3) and very sensitive. Moreover they do not have significant directional dependence, no pressure or temperature corrections need to be taken into account; they are dose rate independent, very resistant to radiation damage, characterized by good reproducibility and long

term stability. Because of their atomic composition and electron density, they are considered almost water equivalent materials.

The radiation generates light in the scintillator which is transported by optical fibers to a photomultiplier (PMT) outside the irradiation room. Generally two sets of optical fibers coupled to two PMTs are used in order to subtract the Cerenkov radiation background from the measured signal. Their response is linear in the dose range of therapeutic interest.

2.2.5.2 Diamond dosimeters

Diamond dosimeters, on radiation exposure, change their resistance. When a bias voltage is applied, the resulting current is proportional to the dose rate. Diamonds are designed for measuring relative dose in high intensity photon and electron beams. They have a small sensitive volume, thus, providing dose maps with very high resolution. They can be considered as tissue equivalent materials and have a high radiation damage resistance. Since they are water proof, they are employed in water phantom measurements.

2.2.5.3 Gel Dosimetry

Gel dosimetry allows to obtain 3D dose distributions. There are two types of gel dosimeters: Fricke gels and polymer gels. Fricke gels present Fe^{2+} ions dispersed in gelatin, agarose or PVA matrix. Radiation converts Fe^{2+} ions in Fe^{3+} with a corresponding change in paramagnetic properties which are detected using nuclear magnetic resonance (NMR). This allows to reconstruct a 3D image of the dose distributions. The major limitation of this system is due to the continual post-irradiation diffusion of ions which leads to blurred images. Instead, in polymer gels, monomers are dispersed in gelatin or agarose matrix. Radiation polymerizes such monomers and their changes can be detected by a NMR, CT tomography, ultrasound, etc.

Chapter 3

Characterization of a new silicon strip detector for verification of complex radiotherapy treatments with photon beams

The description of the methodology adopted to calibrate the new silicon strip detector as an absolute dosimeter following a clinical protocol and its application for dose map reconstruction in the axial plane is described in this Chapter, which is structured as follows: it begins describing briefly the dose delivery in complex radiotherapy treatments, providing information about clinical linear accelerator, treatment planning and verification, and the protocol for absolute dose calibration. Then, it continues with the thesis core which describes the new dosimetry system and presents the studies conducted to characterize the detector response in absorbed dose to water. It must be underlined that the detector's characterization in standard conditions was performed in [7], but, these studies had to be repeated in this thesis because of two major changes of the system:

i) Length of one of the two detector's Kapton cables: the breakdown of this cable led to a different detector design respect to the original prototype. ii) Changes of the electronics components to fix a saturation of three boards out of four of the electronics used for the signal processing that was present in the measurements presented in [8].

After having characterized the system in standard conditions, the detector was placed in a rotating cylindrical phantom and calibrated under treatment conditions. To do that, a new protocol for the dose calibration has to be applied since the detector active area is now parallel to the beam axis. The measurements in this configuration, the study of the detector response at different angles, the calibration in absorbed dose are novel and presented for the first time in this work. The thesis core ends showing the application of this device for a reconstruction of an axial dose map and the comparison with the dose distribution provided by the treatment planning system. At the end of the Chapter, the results obtained are discussed in the section "Final remarks".

3.1 Clinical tools for complex radiotherapy treatments

3.1.1 Clinical linear accelerator

The accelerator used for the measurements is a clinical linac (model Siemens PRIMUS) installed at the Virgen Macarena Hospital of Seville. This clinical linac accelerates electrons that can be used for electron and/or photon therapy.

In a standard clinical linac, two main parts can be distinguished: one assigned to the beam production and acceleration, the other dedicated to the beam delivery. The components used for the production and acceleration of the beam are:

- Injection system: it is the source of the electrons and it is essentially a simple electrostatic accelerator called an electron gun. There are two types of guns: diode and triode type. Both contain a heated filament cathode and a perforated grounded anode. The triode, in addition, presents a grid. Electrons are thermo-ionically emitted from the heated cathode, focused by a curved electrode and accelerated towards the anode. In a triode gun, the grid is kept to a negative potential respect to the cathode in order to cut off the current to the anode.

- RF power generation system, constituted by an RF power source and a pulsed modulator. It generates microwave radiation used to accelerate the electrons to the desired kinetic energy.

- Accelerating waveguides: evacuated structures used for the transmission of the microwaves. The electrons are accelerated in the waveguide by means of an energy transfer from the high power RF field, set up in the accelerating waveguide.
- Auxiliary system which includes a series of elements not directly connected to the acceleration such as: vacuum pumping system, water cooling system, air pressure system for pneumatic movement of the target and/or other beam shaping components, shielding elements.
- Beam transport system such as evacuated drift tubes and bending magnets.
- Beam collimation and monitoring system, such as steering coils and focusing coils.

Electrons originating in the electron gun are accelerated in the accelerating waveguide to the desired kinetic energy and then brought, through the beam transport system into the linac treatment head (fig. 3.1), which is equipped with dedicated elements, to monitor the production, the shape and the delivery of the beam at the exit of the linac [20]:

- Retractable X-ray targets: such targets allow to set up photon beams or to be retracted, leaving electron beams.
- Flattening filters: to flatten the beam.
- Primary collimator: it defines a primary circle.
- Secondary collimators: two upper and two lower independent jaws to shape the beam in squared an rectangular fields.
- Dual transmission ionization chambers: to monitor the radiation beam.
- A field defining light and a range finder: to provide visual methods for the correct positioning of the patient using referenced marks, by illuminating an area equal to the radiation field.
- A Multi-leaf collimator (MLC): it combines tens of pairs of leaves individually motorized moving along the transversal direction (cross-plane). The leaves allow the generation of irregular radiation fields, which adopt the required shape with high accuracy. They are normally used in combination

with the jaws to obtain fields of any shape and size varying from a few millimeters (mm^2), to (40×40) cm^2.

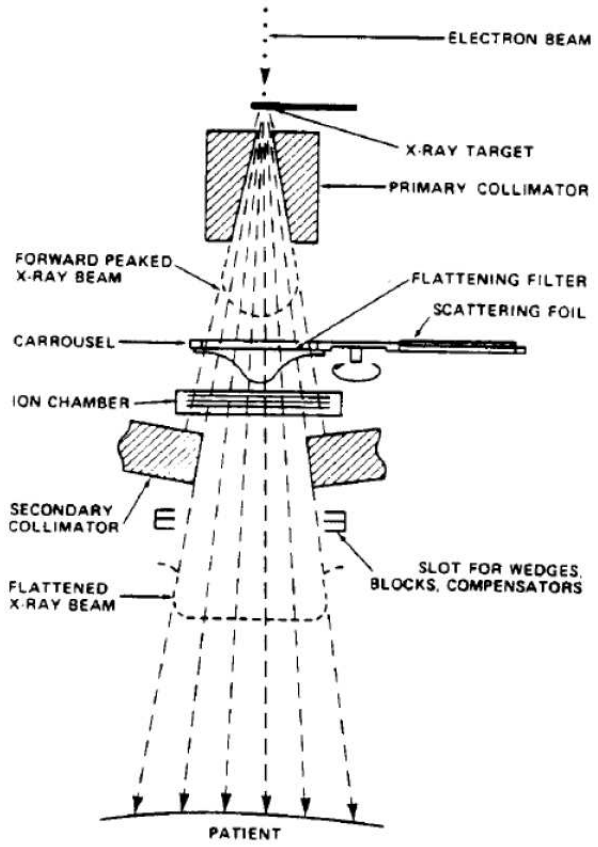

FIGURE 3.1: A scheme of the linac head (taken from [34])

3.1.2 Treatment verification in complex radiation therapy

The treatment strategy in radiotherapy is established from the cooperation between radiotherapists working together with clinical medical physicists. Radiotherapists prescribe and approve the patient's treatment while the medical physicists have the role of ensuring the correct delivery of the radiation dose distribution, with the purpose of maximizing the dose to the malignant area and, at the same time, minimizing the dose to the surrounding critical organs.

The achievement of dose distributions shaped according to the tumor anatomy requires complex radiotherapy treatments. The first step consists of getting an

image (usually using CT scans) of the area to be treated. Then, the different volumes of interest for radiotherapy treatments (which definitions are given by ICRU 83 [35]) are identified (fig. 3.2):

- Gross tumor volume (GTV): the gross palpable extent of the malignant grow.
- Clinical target volume (CTV): a volume of tissue that contains the whole GTV, taking into account possible sub-clinical malignant disease (anatomical concept).
- Internal target volume (ITV) is the expansion of CTV including organs motions.
- Planning target volume (PTV): region that shapes the dose distribution to assure that an adequate dose will be delivered to the all parts of CTV (geometric concept).
- Organs at risk (OAR): critical structures close to the tumor volume.

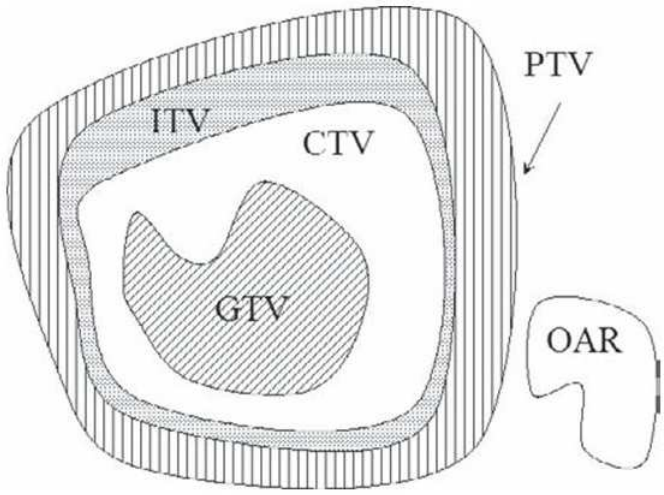

FIGURE 3.2: Margins of GTV, CTV, ITV, PTV and OAR (from ICRU report 83, [35])

Subsequently, the radiotherapist prescribes the dose to the PTV, indicating the maximum limit of dose that the OARs can receive. Thus, the medical physicist plans the treatment strategy establishing the beam characteristics in the treatment planning system (TPS) and then simulating the dose distributions using its algorithms.

However, uncertainties in the TPS dose distribution might occur [36] apart from those due to the data used to model the beam. In fact, the TPS is generally configured with data of the linac operating under standard conditions. Generally, TPS may furnish dose distributions that are not enough accurate because of:

- small field size compared to the range of the secondary electrons produced by the incident radiation (lateral electronic equilibrium is not achieved);
- large heterogeneities of the area to be treated;

Because of this, a complex treatment has to be verified before delivering it to the patient. The goal would be to have a system able to reconstruct dose maps in the axial plane, which means, in the same planes as the CT scan, from which the treatment planning is performed.

Dosimeters traditionally used for treatment verification are described in section 2.2.

At present there are commercial devices of 2D arrays of diodes and/or ionization chambers(such as MapCHECK, MatriXX and OCTAVIUS 729), which provide 2D dose map distributions. However, these systems are designed to be irradiated only perpendicularly with respect to detector active area, hence, to get axial dose maps, they must rely to certain approximations. A Swedish based company, ScandiDos, developed a pre-treatment full plan verification phantom called Delta^4. This system uses cylindrical diodes that are installed in two orthogonal planes inside a polymethylmethacrylate (PMMA) phantom. This system provides on-line dose map reconstruction in the desired plane, but, it heavily relies on TPS calculations.

Radiochromic films show very high spatial resolution (less than 1 mm) and are able to furnish 2D dose distributions in the axial plane. However, it takes time to get the dose distribution since they need to be scanned and analyzed.

Recent developments shifted the attention on silicon strip/pixel detectors, presenting new prototypes (such asMAESTRO [31], DOSI [32], and CMRP DMG detectors [33], already mentioned in section 2.2.2) to improve spatial resolution for complex radiotherapy verification.

Our research group conducted a feasibility study for treatment verification method using a silicon strip detector (model W1(SS)-500) ([4], [2], [5], [3]) offering a valid

alternative to overcome these disadvantages to offer a fast, reusable system with good radiation hardness to obtain 2D dose maps in the axial plane for the treatment verification. Because of the good results obtained, this system was filed in a patent at the OEMP - "Oficina Española de Patentes y Marcas"- Ministry of Industry, Tourism and Commerce, under reference number P201101009 [1].

The novel prototype studied in this work, based on the same silicon strip technology as the W1(SS)-500, shows important implementations (details are given in 3.3.1) which provide dose distributions in the axial plane with improved resolution and bigger active area. Moreover, as will be explained later, its special configuration allows to halve the data acquisition time.

3.1.3 Absolute photon dosimetry

Absolute dose values are obtained using devices which calibration is traceable directly or indirectly to primary standards. These are instruments of the highest metro-logical quality that permit determination of the unit of a quantity from its definition, the accuracy of which has been verified by comparison with standards of other institutions of the same level. Primary standards are realized by the primary standards dosimetry laboratories (PSDLs) in about 20 countries worldwide [20].

Since PSDLs are few around the world, routine calibrations instead rely on secondary standards dosimetry laboratories (SSDLs) which are equipped with instruments previously calibrated in PSDLs.

Thus, clinical centers for the calibration of the response of their devices count on SSDLs. The reading of a dosimeter at a certain beam quality has to be related to the absorbed dose in the medium, without being perturbed by the dosimeter.

To do that, two protocols have been conventionally followed in radiotherapy:

- Air KERMA based protocols for air calibration coefficients;
- Protocols based on absorbed dose to water calibration coefficients;

The air KERMA based protocols are being fallen into disuse. Hence the discussion here is limited to the second protocol, since it is the one adopted to calibrate our system.

The dose to water, at a referenced depth in water z_{ref}, for a reference beam quality Q_0 is:

$$D_{W,Q_0} = M_{Q_0} N_{D,W,Q_0} \tag{3.1}$$

where M_{Q_0} is the fully corrected dosimeter reading under the reference conditions used in the standard laboratory and N_{D,W,Q_0} is the calibration coefficient in terms of absorbed dose to water of the dosimeter.

When a dosimeter is used in a beam with quality Q different from Q_0, the absorbed dose is given by:

$$D_{W,Q} = M_{Q_0} N_{D,W,Q_0} k_{Q,Q_0} \tag{3.2}$$

where k_{Q,Q_0} is a correction factor that takes into account the differences between the referenced beam quality Q_0 and the one used Q. It is defined as the ratio of the calibration coefficients (at beam qualities Q_0 and Q) in terms of absorbed dose to water of the dosimeter:

$$k_{Q,Q_0} = \frac{N_{D,W,Q}}{N_{D,W,Q_0}} \tag{3.3}$$

The common reference quality Q_0 used for the device calibration is the ^{60}Co radiation. Some PSDLs are extending the calibration procedures using as reference high energy photon and electron beams.

If the dosimeter is small compared to the range of the secondary particle field (as usually are the devices used with this scope, i.e. IC, diodes), the absorbed dose to the medium could be calculated using the Bragg-Gray approximation (cavity theory in Chapter 2), relating the absorbed dose at a point in the medium (i.e. water) D_W to the mean absorbed dose in the detector (cavity, $\overline{D}_c$) through the ratio of the mass collision stopping powers ($s_{W,c}$):

$$D_W = \overline{D}_c s_{W,c} \tag{3.4}$$

for which the particle fluence present in the cavity is equal to that in the (undisturbed) medium at the point of interest. Deviations from perfect Bragg-Gray behavior are accounted for adding perturbation factors.

3.2 Thesis core: materials and methods

A novel system was designed to meet clinical requirements in radiotherapy with improved spatial resolution and bigger active area, to perform radiotherapy treatment verification faster than the ones obtained by the previous prototype patented by this research group [4], [3], [2], [5] (model W1(SS)-500, fig. 3.3).

This section starts describing the characteristics of the novel detector, followed by the depict of the two phantoms used respectively for the calibration of the detector under standard and treatment conditions. Then, the improvements introduced in the data acquisition interface are presented, together with a new interface for the on-line data analysis. The section ends with the algorithm used for the axial dose map reconstruction.

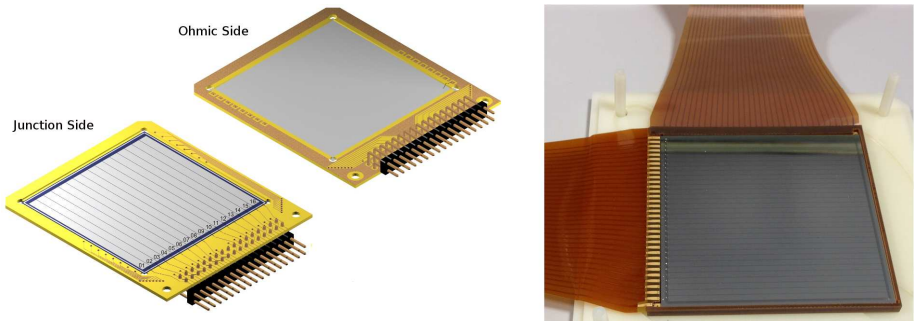

FIGURE 3.3: W1(SS)-500 compared to the model BB7 for radiotherapy treatment verification.

3.2.1 Characteristics of the new silicon strip detector

The new prototype was designed, developed and built within the context of RADIA collaboration (Departments of FAMN and Electronic Engineering of the University of Seville, the National Accelerator Centre (CNA) and the University Virgen Macarena Hospital), with the support of the companies ATI sistemas S.L. and Micron Semiconductor Ltd.; the latter was also responsible for its construction.

In the new design, based as the previous one on silicon strip technology, we decided to modify four key elements for improving the performances respect to the previous one [6]:

1. Bigger active area (64×64) mm^2 to allow measurements of larger dose maps.

FIGURE 3.4: Experimental setup used for the measurements: both pictures show the linac head, the slab phantom centered with the laser system of the clinical treatment room, and the electronics.

2. Smaller strip width (2 mm), 32 strips per wafer, to improve the spatial resolution.

3. Two perpendicular strip orientations to allow simultaneous measurements in two different orientations, hence reducing considerably the acquisition time.

4. Optimization of the packaging of the detector, minimizing it and improving the density uniformity of materials with respect to the previous design.

Let us now explain in detail the characteristics of the detector and how these four improvements were realized. The dual single sided silicon strip detector (D-SSSSD) is composed of two 500 μm thick detectors, model BB7 from Micron Semiconductor Ltd., mounted together with the detector strips perpendicular to each other, thus, implementing the ability to perform simultaneous measurements with two different strip orientations. Another goal of the new setup is to minimize the perturbation due to placing the detector in the medium (water-like) where absorbed dose has to be measured. This can be achieved by uniformizing detector composition with material densities as close as possible to water density. Thus, for the frame of the new detector, 1200 μm Kapton was chosen (Arlon 85N polymide laminate from DuPont), with a density of 1.6 g/cm^3. Since Kapton presents very

low thermal conductivity and very good insulating properties, a 500μm Kapton film was used as dielectric separator between both silicon wafers, avoiding air gaps between them. Following the idea of minimizing materials, that can cause perturbations around the detecting volume, the connectors, for the strip signal reading, are moved away from the detector frame. To do this, two thin Kapton cables were designed. One extreme of them is directly connected to the strips and, at the other end, pin connectors (Samtec TSW 117 7 L D) were installed. These flat cables, 200 mm long, are made of 50 μm DuPont AP8525R core of a density of 1.43 g/cm^3, with 18 μm of copper on each side. The characteristics of the new device compared to the previous detector are summarized in table 3.1:

Characteristics	W1(SS)-500 detector	Dual chip SSSSD BB7
Nº Wafers	**1**	**2**
Nº Junction elements on Wafer 1	16	32
Nº Junction elements on Wafer 2	N/A	32 (perpendicular to strips on wafer 1)
Element lenght	49.5 mm	64 mm
Element pitch	**3.1 mm**	**2.1 mm**
Element width	3000 μm	2000 μm
Active Area	**50 x 50 mm^2**	**64 x 64 mm^2**
Wafer Thickness	500 μm	500 μm
Element active volume	49.5 x 3.0 x 0.5 mm^3	64 x 2.0 x 0.5 mm^3
Metallization	Aluminum 0.3 μm	Aluminum 0.3 μm
Package	**PCB with edge connections**	**Kapton with 20 cm cables**
Structure material	**FR4 (1.85 g/cm^3)**	**Kapton (1.6 g/cm^3)**

TABLE 3.1: Comparison between the characteristics of the W1(SS)-500 detector and the Dual chip SSSSD BB7. The most important improvements are highlighted in bold

During the measurements one of the two kapton cables was damaged leading to a modification of the length of the cable, and, in the other cable, two wire bondings needed to be re-solded a couple of times. This experience suggests that an improvement in the robustness of the cables and connectors is needed for the construction of the definitive model.

An electronics system was designed specifically for the acquisition of the integrated charge collected by the strips of the detector when exposed to the irradiation field. It was developed by engineers from the Department of Electronic Engineering of

the University of Seville. Some modifications were introduced in its components after the detector reparation. All the details about the first electronics prototype can be found in [8].

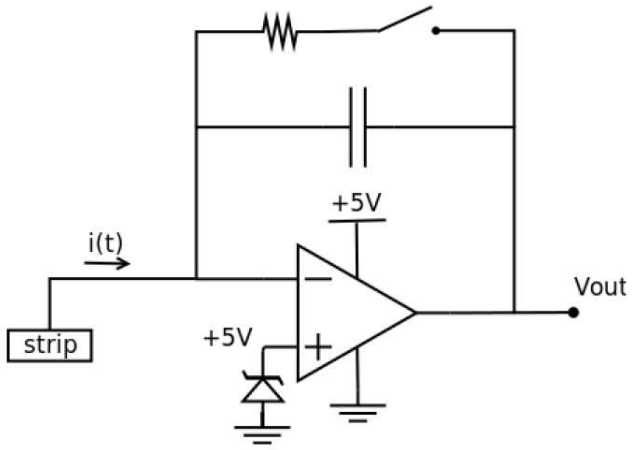

FIGURE 3.5: Simplified circuital diagram of the charge integrator implemented for each strip taken from [7]

The total charge produced by the ionizing radiation is proportional to the absorbed dose. The front-end readout electronics has therefore been implemented as an integration circuit, composed by an operational amplifier with negative feedback through a capacitor (fig. 3.5). The capacitor can be short-circuited by means of a switch (provided by a MOSFET transistor in switch mode), thus resetting the accumulated charge. The positive pin of the amplifier is set at a reference voltage of $V_i = +5V$, using a Zener diode. The output voltage $V_0(t)$ is therefore

$$V_0(t) = V_i - V_c(t) = V_i - 1/C \int_0^t i(t')dt' = V_i - q(t)/C \tag{3.5}$$

where $V_c(t)$ is the voltage drop across the capacitor (of capacitance C) at time t, i(t) is the current at the time t and q(t) is the total charge. The output voltage is therefore a linear function of the absorbed dose. The voltage signal for each strip is then buffered to avoid charge losses and digitized by means of 16-bit, eight-channel ADC converters (serial number ADS8568 by Texas Instruments).

In order to collect the signal of the 64 strips, eight ADCs have been used, placed in four different boards. Each of them samples eight channels sequentially. The data acquisition is managed by a software developed under the LabVIEW platform.

It controls all the hardware components of the electronic chain, including the motor and the angular sensor of the cylindrical phantom (see next subsection); it constitutes the interface of the acquisition-related operations like sending the trigger, resetting the capacitors and changing the sampling time (usually set at 100 ms in our acquisitions). The measured values are plotted as a function of time in order to check the data acquisition, and then stored in a file for off-line analysis.

3.2.2 Phantoms

The detector was placed in a polyethylene box (fig. 3.6, central panel) with dimensions 108.4 x 108.4 x 46.1 mm^3, in order to protect it and facilitate the positioning in the phantoms.

Two phantoms made of polyethylene were mechanized to host the detector: a slab phantom (fig. 3.6, right panel) is used to place the detector plane orthogonally to the beam axis and, a cylindrical rotating phantom, where the detector active area is placed parallel to the beam axis.

The slab phantom is used to characterize the detector strip response and to calibrate it in absorbed dose to water in standard conditions; its dimensions are 300.0 x 300.0 x 46.0 mm^3. The detector placed in the system box plus phantom is lying in the movable treatment couch, then centered using the lasers in the treatment room. Because of the transversal dimensions of the slab phantom and of the box, the minimum solid water depth achievable is 1 cm.

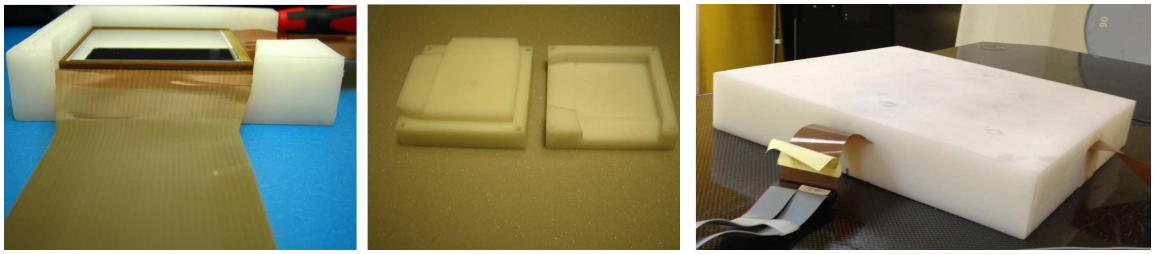

FIGURE 3.6: From left to right: Detector, polyethylene box and slab phantom

The cylindrical phantom is used for the detector angular response characterization, which is needed for the calibration in treatment conditions. It is composed by independent parts (fig. 3.7): one of the two central pieces (fig. 3.8) hosts the box with the detector, the right one is coupled to an angular sensor (which allows to

check its angular position during the measurements) and the left part is connected to a motor, controlled by a LabVIEW software interface, which allows to rotate the phantom. The phantom can be rotated around its symmetry axis with a precision better than 1^o. The total dimension of this prototype are 64 cm of length and 24 cm of diameter. The phantom is mounted in a polyethylene base (which can be removed for the experiments) to meet more stability and easiness during its carriage, reaching a total height of 27 cm. The detector's cables, to reach the electronics, are coupled to cables extensions through pin connectors. The connectors and the kapton cables fragile elements of the system, thus, polyethylene protections have been designed and constructed to protect them. Cable ties are used to fix the connector protections and the cable extensions to the phantom body, allowing to not charge with extra pressure the detector's Kapton cables.

The phantoms' dimensions assure the necessary electronic equilibrium conditions.

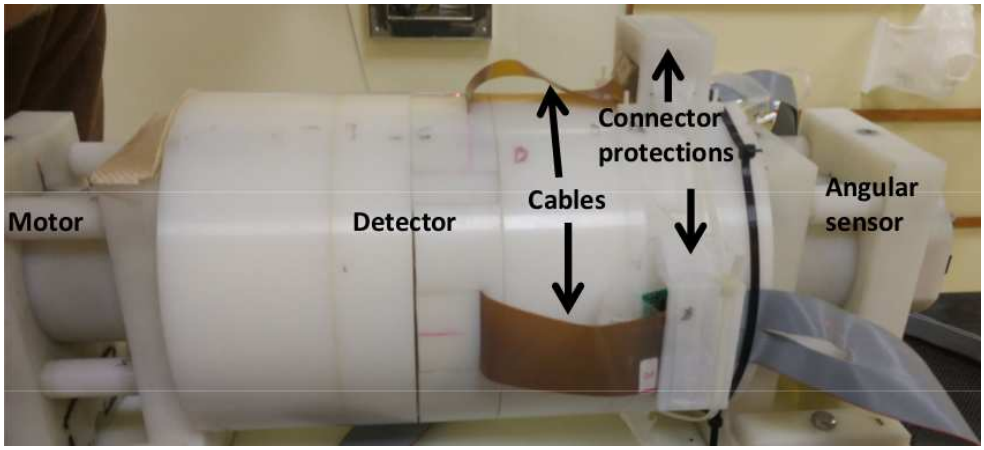

FIGURE 3.7: Picture of the cylindrical phantom which is formed by assembling four cylinders of polyethylene.

3.2.3 LabVIEW interface

For the data acquisition and analysis, our system dispose of two dedicated LabVIEW interfaces.

The one dedicated to the data acquisition was for the first time implemented and presented in [8]. Some important options were added within this thesis work, in order to equip this interface with buttons that permits the remote control of the cylindrical phantom rotation.

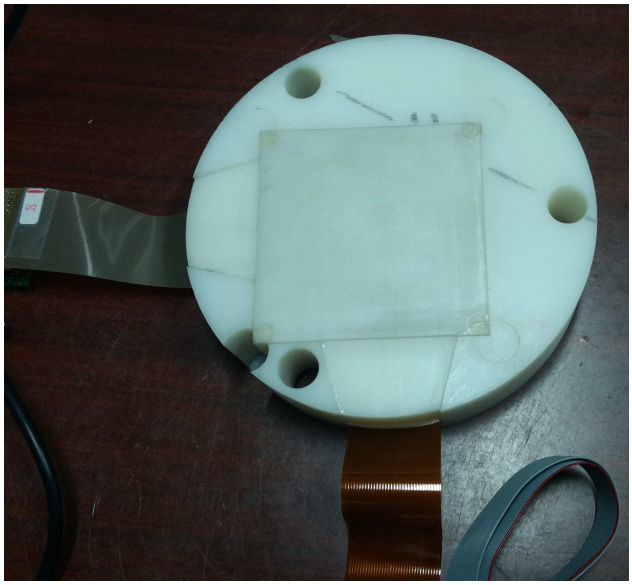

FIGURE 3.8: Detector inside the box mounted in a transversal section of the cylindrical phantom

Fig. 3.9 represents the interface dedicated to the data acquisition, which is divided into three main panels:

- Top left panel: it allows the connection between the ADC and the software for the data acquisition using the Controller Area Network (CAN, serial communications bus) protocol.
- Central left panel: in this section, one can set the sampling period, the number of samplings to acquire (saved through the trigger button). These parameters are saved and displayed at the top right panel, named "System Variables". Then one can start the acquisition.
- Central left panel: to control the rotating motor of the cylindrical phantom. It allows to choose the rotation angle and the direction (turn right or left).

Another brand-new interface was implemented here for the data analysis, fig. 3.10. It allows in a first place an on-line checking that the system is working properly and the on-line detection of errors or failed measurements, step by step. Once all the parameters are verified, the axial dose map reconstruction is provided only pressing one button.

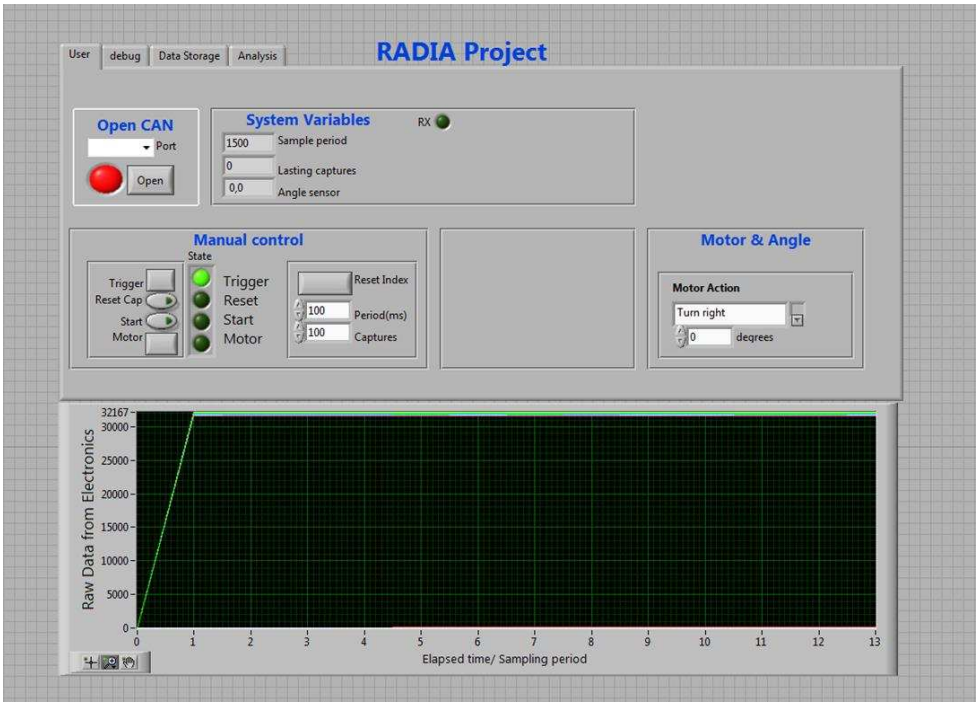

FIGURE 3.9: LabVIEW interface for data acquisition

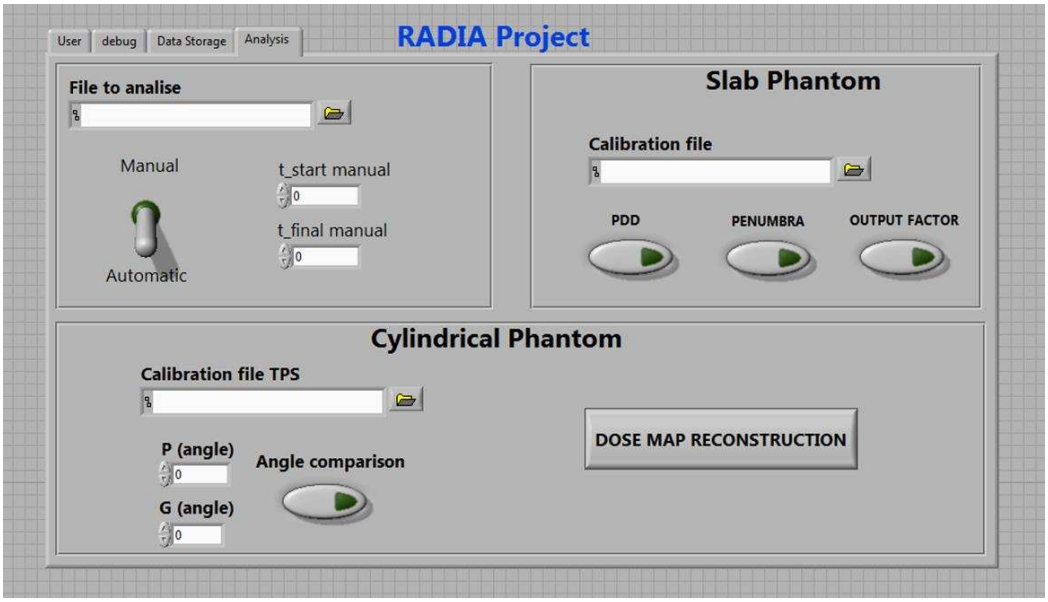

FIGURE 3.10: LabVIEW interface for data analysis

This was achieved coupling Matlab ([37]) scripts that perform the data analysis to the LabVIEW interface. The analysis interface is equipped with three main panels:

- top left panel: opening the file to analyze; plotting the strip response as function of irradiation time. Finding the initial and final instants of the irradiation (automatic or manual option);
- top right panel: calibration of the strips' response in absorbed dose (in standard conditions) and study the PDD, penumbra and output factor (detector placed in the slab phantom);
- bottom: it allows to calibrate the response of the detector in the cylindrical phantom (the complete procedure will be explained in section 3.3.2). Subsequently, the data are collected at different angles, calibrated and storage in a matrix. Since we dispose of a dual SSSSD, the 32 strips of one detector's chip are arraying the data in a range of 0^o - 90^o, and at the same time, the other 32 are collecting the data between 90^o and 180^o, allowing a complete dose map reconstruction reducing at a half the acquisition time respect to the system with the W1(SS)-500. Last, once all the data at different projections are acquired, the reconstruction algorithm can be launched and the axial dose map is calculated and displayed.

3.2.4 Algorithm for dose map reconstruction with Radon transform

In this subsection, the algorithm that allows to reconstruct a 2D dose maps with the Radon transform will be exposed. The algorithm is adapted from the one developed by Miguel Antonio Cortes Giraldo [1] for the previous detector (W1(SS)-500), which was successfully used for dose map reconstruction in [2]. A theoretic introduction will be given to supply the formulas which have been used. Then, the modifications carried out within this work to apply the reconstruction algorithm to our case with the real dimensions of our system are presented.

3.2.4.1 Theoretical basis

Let's define f(x,y) as a bi-dimensional function defined in a plane with dimensions x and y. If we consider the rotation in a plane of a vector (x,y) of an angle θ, the new vector (x', y') can be expressed as:

$$\begin{pmatrix} x' \\ y' \end{pmatrix} = \begin{pmatrix} cos(\theta) & sin(\theta) \\ -sin(\theta) & cos(\theta) \end{pmatrix} \begin{pmatrix} x \\ y \end{pmatrix} \tag{3.6}$$

the projection of the function f over the x direction is:

$$p(x', \theta) = \int_{-\infty}^{\infty} f(x'cos\theta - y'sin\theta, x'sin\theta + y'cos\theta)dy' \equiv R\{f(x, y)\} \tag{3.7}$$

given such equations, one has to reconstruct the function f(x,y) (which is unknown), starting with the projection p(x', θ).

This problem can be solved by the Theorem of the projections:

being F(k_x,k_y) the bi-dimensional Fourier transform of f(x,y) and P(k, θ) the Fourier transform of the projection p(x', θ),

the projection theorem demonstrates that:

$$F(p(x', \theta)) = F(k_x, k_y) \tag{3.8}$$

where k_x = k cos θ and k_y = k sin θ. It is then possible to calculate f(x,y) by knowing the projection p(x',θ), where 0$\leq \theta \leq \pi$:

$$f(x, y) = F^{-1}(P(k, \theta)) = \int_{-\infty}^{\infty} dk_x \int_{-\infty}^{\infty} dk_y P(k, \theta) e^{2\pi i(k_x x + k_y y)} \tag{3.9}$$

Changing the coordinates k_x and k_y in polar coordinates k, θ, the integral becomes:

$$f(x, y) = \int_0^{\pi} d\theta \int_{-\infty}^{\infty} dk P(k, \theta)|k| e^{2\pi i(kx')} \tag{3.10}$$

Now we define

$$p^*(x',\theta) = \int_{-\infty}^{\infty} P(k,\theta)|k|e^{2\pi i(kx')} = \int_{-\infty}^{\infty} P^*(k,\theta)e^{2\pi i(kx')} \tag{3.11}$$

thus,

$$f(x,y) = \int_0^{\pi} d\theta p^*(x',\theta) \tag{3.12}$$

with

$$p^*(x',\theta) = p(x,\theta)F^{-1}(|k|) \tag{3.13}$$

which is given by the backward projection of the function p(x, θ) and the filter $F^{-1}(|k|)$.

3.2.5 Algorithm for 2D dose maps with the D-SSSSD

The dose map reconstruction is based on the Projection theorem, which allows to calculate the dose distribution on the plane x,y with the knowledge of a projection in a direction x' at an angle θ. Each detector strip is considered as an independent detector and has a length of 64 mm. The element pitch is a= 2 mm and the number of strips for each detector are 32, thus the strip length can be expressed as l=32*a. If d(x,y) is the dose distribution in the axial plane that has to be found and the d(x', θ) the set of data for each rotation.

Thus, according to formula 3.7,

$$d(x',\theta) = \frac{1}{32a}\int_{-16a}^{16a} d(x'cos\theta - y'sin\theta, x'sin\theta + y'cos\theta)dy' \equiv \frac{1}{32a}R\{f(x,y)\} \tag{3.14}$$

the factor 1/32*a is averaging the accumulated dose over the strip length. In this case, the material is considered homogeneous and the averaging factor is purely geometric. Considering the projection theorem:

$D(k_x,k_y)=F_{2D}d(x,y)$ and $\overline{D}(k,\theta) = F\overline{d}(x',\theta)$ then, $D(k_x,k_y)=32a\ \overline{D}(k,\theta)$.

From the last relation, it can be written the equation to find d(x,y):

$$d(x,y) = 32a\int_0^{\pi} d\theta \int_{-16a}^{16a} dk\overline{D}(k,\theta)|k|e^{2\pi i(kx')} = \int_0^{\pi} d\theta\overline{d}^*(x',\theta) \tag{3.15}$$

Since the detector is measuring for values of x_n= (n-16.5)a with n= 1,2,..32, then integral must be discretized:

$$\overline{d}(n,\theta) = \frac{1}{a}\int_{17a}^{16a} \overline{d}(x',\theta)dx' \approx \overline{d}(x'_n,\theta) \tag{3.16}$$

$\overline{d}$(n, θ) represents our set of data. Thus the discrete Fourier transform $\overline{D}$(k, θ) becomes:

$$\overline{D}(m\Delta k,\theta) = \sum_{p=0}^{M-1} \overline{d}(p\Delta x,\theta)e^{-2\pi i m_p/M} \tag{3.17}$$

where Δx is the element pitch a and k_{max}=1/2a thus Δk=1/Ma where M=32. If we consider that the strips are enumerated as n=1, 2, ..., 32 then the previous equation becomes:

$$\overline{D}(m/Ma,\theta) = \sum_{n=1}^{M} \overline{d}(n,\theta)e^{-2\pi i m(n-16.5)/M} \tag{3.18}$$

with m=-(M-1)/2,..,(M-1)/2. Applying the inverse Fourier transform in its discrete formalism:

$$\overline{d}^*(x'_n,\theta) = 1/M \sum_{m=-(M-1)/2}^{(M-1)/2} \overline{D}(m/Ma,\theta)|m/Ma|e^{2\pi i m(n-16.5)/M} \tag{3.19}$$

where M is the normalization factor needed to pass from the Fourier transform to its inverse. Now, it is possible to calculate pixel by pixel the dose distribution:

$$d(x_i,y_i) = 32a \sum_{q=1}^{180/\Delta\theta} \overline{d}^*(x'_n,\theta_q)\Delta\theta \tag{3.20}$$

$\Delta\theta$ is given by the experimental setup: the detector is supposed to be rotating around its center, thus the angular step of the measurement is set as the inverse tangent of the ratio between the element pitch and half length of the strip ($\tan^{-1}$(a/(l/2)), leading to a value of $\Delta\theta \approx 3.60^o$ and θ_q = q $\Delta\theta$. If the dimension of the pixels are equal to the element pitch dimension a= 2 mm, x_i = (i-16.5)a and y_j= (j-16.5)a, thus obtaining the value of d(x,y) for each pair x_i,y_j if they satisfy

the relation:

$$x'_n = x_i cos\theta_q + y_j sin\theta_q \tag{3.21}$$

The last equation must be satisfied for all the sets of integers i, j, n, q. For this reason and to be able of obtaining the dose in the pixels of sensitive area of the detector, the interpolation methods has to be introduced. Being i, j, q fixed values, according to 3.21, x'$_{ijq}$ is not equivalent to x'$_{n}^{32}{}_{n=1}$, but it is possible to find two values x'$_m$ and x'$_{m+1}$ for which: x'$_m$ < x'$_{ijq}$ < x'$_{m+1}$ with 1 < m < 31. Being x'$_{m+1}$-x'$_m$ = a, the values of the dose in each pixel are obtained by the sum of the linear interpolation, as it follows:

$$\overline{d}^*(x_{ijq}, \theta_q) = \overline{d}^*(x_m, \theta_q)\frac{x'_{m+1} - x'_{ijq}}{a} + \overline{d}^*(x_{m+1}, \theta_q)\frac{x'_{ijq} - x'_m}{a} \tag{3.22}$$

leading to the final expression for d(x,y):

$$d(x_i, y_i) = 32a \sum_{q=1}^{180/\Delta\theta} \overline{d}^*(x_{ijq}, \theta_q)\Delta\theta \tag{3.23}$$

Since we dispose of two SSSSD mounted in a perpendicular configuration, we assume that one detector with 32 strips is collecting the data from 0º to 90º, and, contemporaneously, the other one from 90º to 180º. Thus, referring to eq. 3.23 where the filtered back projections are summed for a range that goes from 0º to 180º, the data from 0º - 90º are derived from the measurement of 'first detector and the rest from the other.

3.2.5.1 Data filtering

The projection-slice theorem that reconstructs the dose map is valid only for the points that were covered by the detector's active area at all rotation angles. Considering that the detector area is of 64 mm, we consider valid the pixels inside a circle centered at the center of the detector with a diameter equal to 64 mm. The formalism explained has to be improved with filters. This comes from the fact that the integral shown in equation 3.7, should converge. However in our case, the interval in which we integrate is limited to the detector's dimensions and does not satisfy the convergence to zero required. As a matter of fact, if the integral does not converge to zero in the interval inside the detectors dimensions, which is

practically the case for a real treatment, some edge artifacts appear in the reconstructed dose map. Because of this reason, a background filter was implemented by M. A. Cortés-Giraldo and applied to the dose map reconstruction in the following way: the minimum value (absorbed dose) between all the strips at every angular position is taken. Then we find the minimum of all the values previously obtained. Afterwards, this value is subtracted to all the strips at every position of the phantom. After the subtraction, the projection-slice theorem is applied and the dose map is reconstructed. Once we obtain the dose map, we add to all the pixels the value that was previously subtracted.

3.3 Thesis core: results

This section presents the results obtained for the treatment verification measurements using the DSSSSD.

The measurements took place at the radio therapy Unit of the HUVM by a Siemens PRIMUS clinical linac operating in 6 MV photon mode. As an illustration, here we present in fig. 3.11 the profiles of a standard field with dimensions (10×10) cm^2 delivered from this clinical linac at a source to surface distance (SSD) of 100 cm for different depths in water.

The protocol for the detector characterization is based on the prescriptions showed in [7]. The study of the detector response and its calibration in absorbed dose to water in standard conditions had to be performed again because of the changes introduced by the reparation of one of the detector's cables and the new design of the electronics.

These studies are presented in the section 3.3.1 where the detector's response was characterized in terms of *linearity, percentage depth dose (PDD), penumbra, output factor and dose threshold*. All these parameters correspond to a clinical protocol usually performed to validate a dedicated device for QA purposes.

Consequentially, the detector was placed in a rotating cylindrical phantom (made of polyethylene as the slab one) and irradiated with its active area parallel to the beam axis. The measurements in this configuration are novel and are presented for the first time in this thesis. Hence, the detector's response was characterized as function of the rotating angles and calibrated under treatment conditions. Once

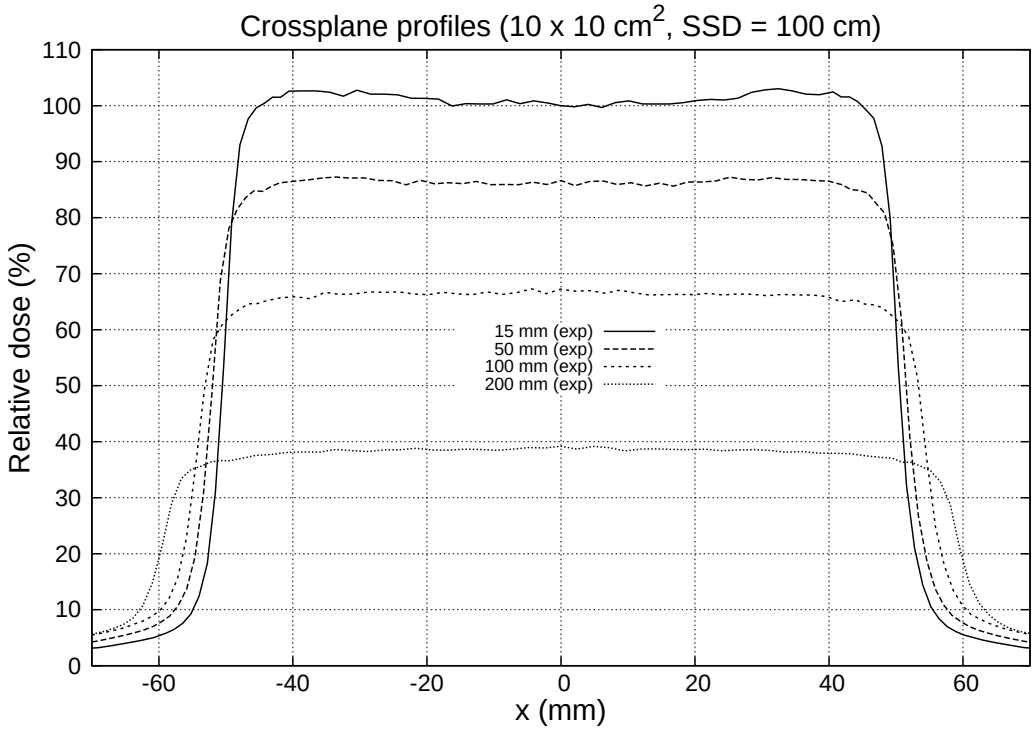

FIGURE 3.11: Profiles of a standard field (10 × 10) cm^2 and SSD = 100 cm of the clinical linac at different depth in water. Plot provided by the radiophysics service of the HUVM.

this procedure was ultimated, a treatment was applied to the phantom, the data were collected at different projections and by means of the filtered back projection algorithm, an axial dose map was reconstructed and compared to the one calculated by the TPS.

3.3.1 Detector characterization in standard conditions

In general, in a silicon strip detector, each strip works as an independent detector, giving a signal in current independent from the other strips. In our case, we dispose of two detectors mounted together (as explained in section 3.2.1) with 32 strips each. Each strip has its own electronics chain, its variations in resistance, capacitance, hence differences might occur between a signal and another.

Before proceeding with the calibration, this section presents considerations about the influences of the different materials that constitutes the detector and how the absorbed dose estimation could be influenced because of them.

With this scope, simulations of the setup were done in [7] using Geant4 toolkit, to furnish interesting tips for the dose calibration. The absorbed dose was calculated for two central pixels defined as sensitive volumes (with dimensions of 4.0 x 4.0 x 0.5 mm^3) for each detector. The effects of the air gaps in the box hosting the detector can be neglected for both upper and lower cavity.

The presence of Kapton between the two cavities is not modifying significantly the dose calculated. Instead, considering the two silicon layers of each detector, in general, the dose obtained is seized by the presence of this material: taking into account the upper detector, the silicon in the lower cavity is perturbing the particle field, producing backscattered particles, which lead to an increase of the dose received by the upper detector. In addition, the shading effect caused by the upper cavity on the lower cavity provokes a decrease in the absorbed dose in the lower one.

Nevertheless, simulations show that the dose absorbed in water at the position of the two cavities is essentially the same.

In summary, the difference in the absorbed dose by the two sensitive layers of the DSSSSD is due to the detector itself and is not related to the process of dose deposition in water. Because of this, a single readout for the dual chip can be used, considering the effective point of measurement located at the detector center (between the two detector chips).

3.3.1.1 Linearity

As stated in chapter 2, a detector can be used as dosimeter when its response can be related (through a calibration curve) to the absorbed dose. The lack of this property would not make convenient the use of such a device as a dosimeter. In order to verify the detector's response to dose for each strip, we irradiated the whole detector area in standard conditions, which means: i) a field of 10 $\times$ 10 cm^2, ii) 100 MU delivered by the accelerator, iii) a SSD of 100 cm and iv) 1.5 cm cm of water equivalent material above the phantom (0.5 cm of solid water plus 1 cm of phantom's polyethylene) In fig. 3.12 the response of the system is presented; we can distinguish three main zones:

- the region before the irradiation (time range 0 s - 156 s) where the number of counts is approximately constant.

- The slope caused by the irradiation (157 s - 460 s), where the charge generated inside the phantom by the secondary electrons produced by the photon field produces the signal (L_{raw}).
- Final region for t > 460 s when the irradiation is stopped.

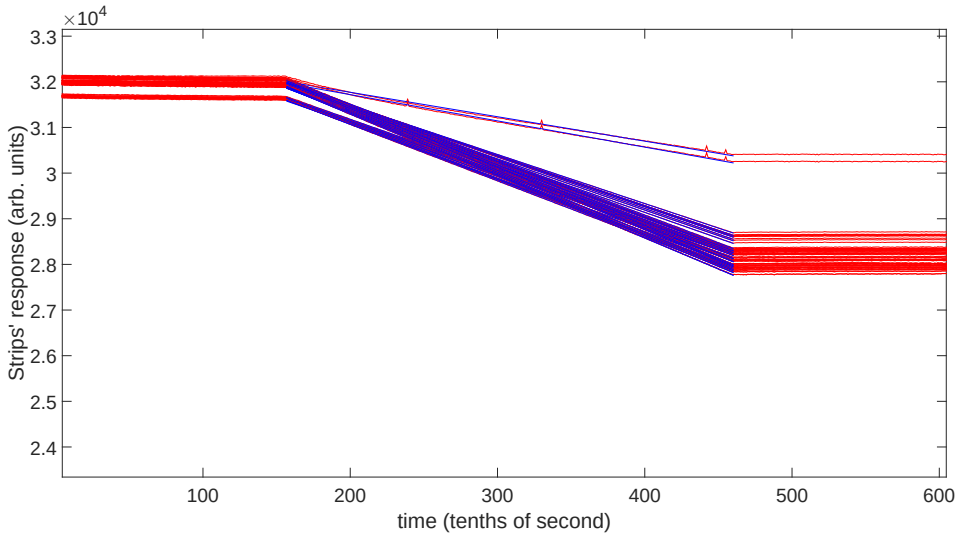

FIGURE 3.12: Raw response for the 64 strips (32 for each detector) of the detector (red curve) as a function of time and linear fit (blue curve)

As it can be seen in fig. 3.12, each strip collects the charge left by the radiation with a linear response as function of the irradiation time. Thus, the signal for the strip i can be fitted with a linear function $L^i = m^i \Delta t$, where m^i is the linear coefficient and Δt the irradiation time (which is the same for all the strips).

The deviation from the linearity is calculated as:

$$(L^i_{raw} - L^i)/L^i * 100 \tag{3.24}$$

where L^i_{raw} is the raw signal for each strip i generated during the irradiation time and L^i is the value obtained after the linear fit. Fig. 3.13 shows the response of one strip as a function of the irradiation time for 500 MU and the linear fit is drawn in blue color. The agreement is within the 0.1 % with an adjusted R^2 of 0.9997.

The study of the linear response was done for all the strips of the detector.

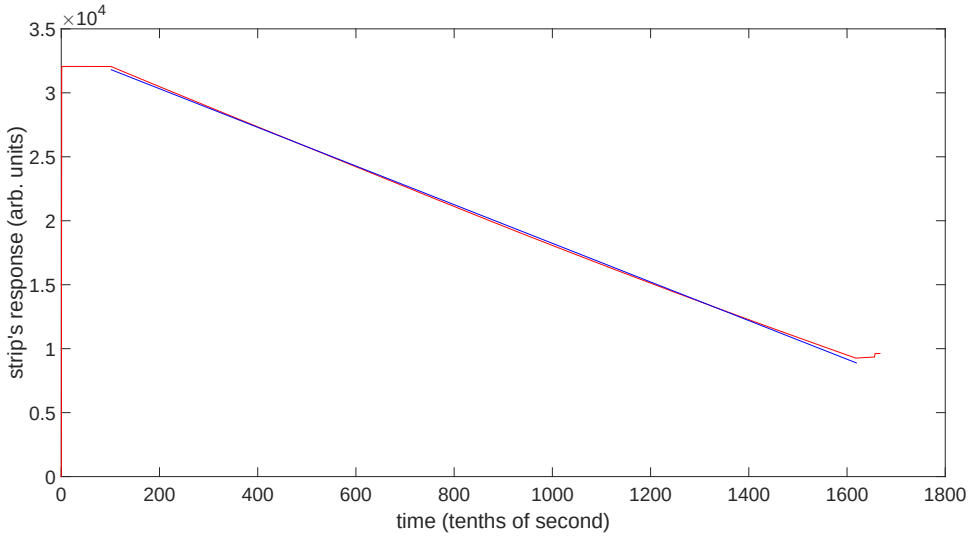

FIGURE 3.13: Response for strip 14 of the silicon strip detector (red curve) as a function of time and linear fit (blue curve)

All the strips of the dual chip have a linear response with an agreement within the 0.1 - 0.2 %, except for the 11 and 12 of the lower detector.

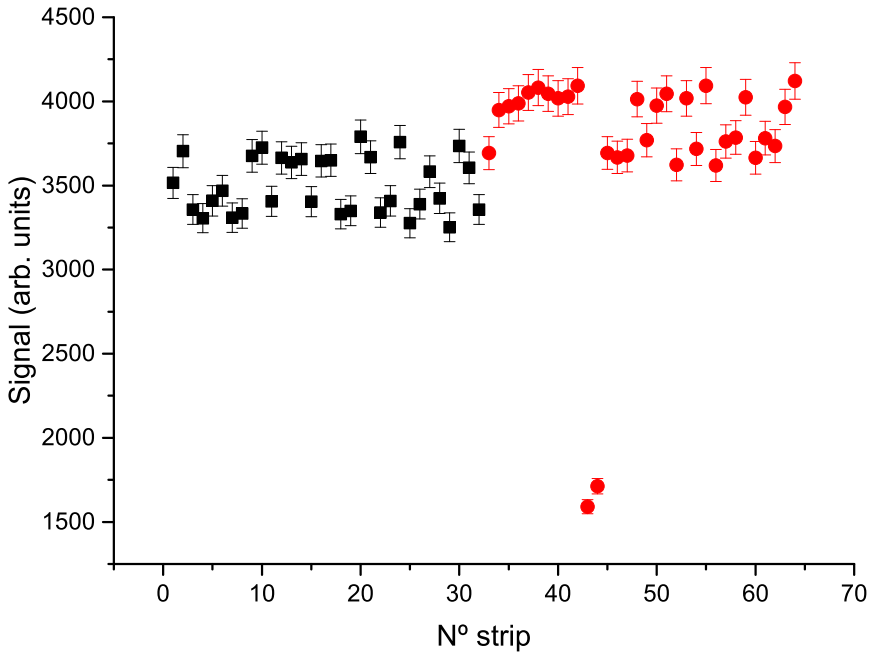

FIGURE 3.14: Raw signal for each detector strip. Black dots are referring to the upper chip while red ones to the lower detector. Strips number 11 and 12 of the second detector (43 and 44 in the plot) show a no reproducible behavior.

The raw signal of the detector strips L^i_{raw} is shown in fig. 3.14. The two detector chips are represented with two different colors: the upper strips are represented in black squares and the lower ones in red circles. As already seen, in the lower detector, there are two strips with a significant difference in the response respect to the other ones. In the measurements performed to calibrate the detector, their response is not reproducible thus, we considered the results given by them not reliable. For this reason, from here on, the analysis will be conducted keeping these two strips out.

3.3.1.2 Uncertainties estimation

As stated previously, the strips's signal is fitted by a linear function, hence the uncertainty associated to the signal can be calculated as:

$$\sigma^i_L = L^i \sqrt{(\frac{\sigma^i_m}{m^i})^2 + (\frac{\sigma_{\Delta t}}{\Delta t})^2} \tag{3.25}$$

where σ^i_m is the uncertainty associated to the linear coefficient m^i for the strip i. The $\sigma_{\Delta t}$ is given by the sampling time of the acquisition: higher sampling times allow a more precise estimation of the initial and final instants of the irradiation. A good compromise between accuracy and software's processing speed was reached by setting the sampling time to 100 ms. Thus, the initial and final instants are identified with an uncertainty of one tenth of second. The uncertainty associated to the slope m reflects the deviation from the linearity of each strip signal (treated independently) which must be taken into account in order to characterize the detector response as a linear dosimeter. As stated in [7], the data dispersion from the linearity is within 0.1 % for irradiations equal or greater than 100 MU. If the same measurement is repeated many times, the bigger contribution to the uncertainty is given by the standard deviation associated to the averaged coefficient m, which is larger than the previous one.

3.3.1.3 Calibration under uniformity conditions

In order to establish a common ground behavior of the strips, uniformity factors have to be calculated. For this scope, the detector was irradiated with a uniform standard field of 100 MU and 10 × 10 cm^2, larger than the detector area. The

irradiation conditions were of SSD = 90.0 cm and 10.0 cm cm of water equivalent material above the phantom (9 cm of solid water plus 1 cm of phantom's polyethylene). Under these conditions, the field beam profile can be considered flat in the detector region.

In order to check the field uniformity over the whole detector area, a EBT3 GafChromic film was irradiated under the conditions described before and analyzed as follows:

- an area of 6.4 × 6.4 cm^2 was selected at the center of the irradiated region 10 x 10 cm^2 of the film (simulating the DSSSSD's dimensions).
- each detector strip, section of 2 mm × 64 mm, was drawn and the netOD (defined in section 2.2.1.2) was calculated for each area as the averaged netOD of the pixels contained in that area. This was done in two perpendicular directions, horizontally (areas of 2 mm × 64 mm) and vertically (areas of 64 mm × 2 mm), to simulate the radiation received by each strip detector, leading to 64 values.
- the averaged netOD is plotted for each area in fig. 3.15 with its uncertainty. The black squares refer to selected area simulating the strips of the upper detector, while, the red circles are for the lower detector's strips.

The averaged value of the optical density for the horizontal direction is 1.00 ± 0.02, while the corresponding value for the vertical one is 0.99 ± 0.02. These values, equal within the uncertainty estimations, are compatible with a uniform field in the detector area.

The calibration factor F^i_{un} for each strip i can be calculated as:

$$F^i_{un} = \frac{D_{un}}{L^i_{un}} \tag{3.26}$$

where L^i_{un} is the signal under uniformity conditions of the strip i and D_{un} is 81 cGy (SSD = 90 cm, 10 cm of solid water depth and an irradiation field of 100 MU and 10 × 10 cm^2 in the uniformity conditions provided above). Three measurements were performed under the same conditions and factors F^i_{un} were calculated for both detector sides and plotted in fig. 3.16.

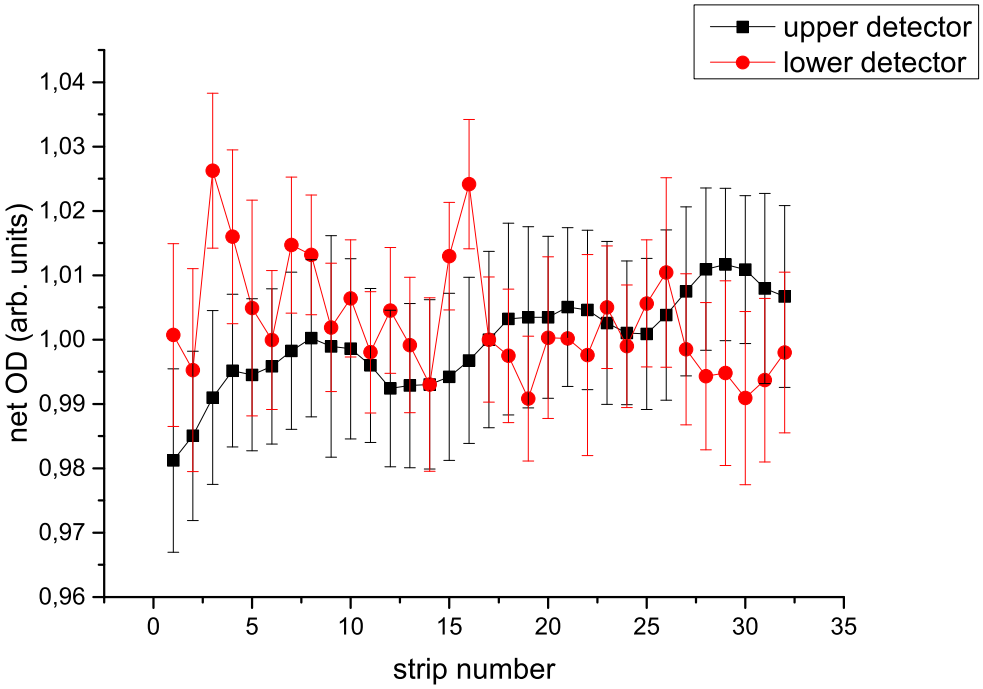

FIGURE 3.15: Response of the EBT3 film in terms of netOD under uniformity conditions for each area that refers to DSSSSD strips . Upper and lower detectors refer to perpendicualr directions in the simulated strips.

Thus, in general, the absorbed dose is given by the equation 3.27:

$$D^i(Gy) = F^i_{un} * L^i \tag{3.27}$$

with its associated uncertainty:

$$\sigma^i_{Dose} = D^i \sqrt{(\frac{\sigma_{F^i_{un}}}{F^i_{un}})^2 + (\frac{\sigma_{L^i}}{L^i})^2} \tag{3.28}$$

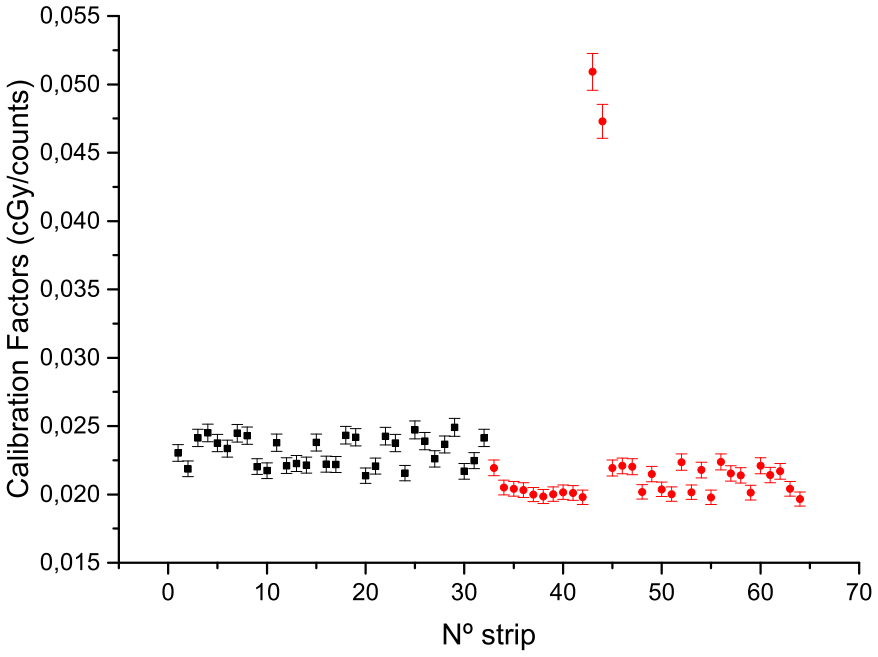

FIGURE 3.16: Calibration factor in uniformity conditions for the upper (black circles) and lower detector (red circles)

3.3.1.4 Calibration under referenced conditions

According to the calibration protocol adopted by the radiotherapy unit of the hospital, under the referenced conditions of SSD = 100 cm, 1.5 cm of solid water depth, beam field size 10 ×10 cm^2, 100 MU delivered by the linac used here correspond to 100 cGy at the beam isocenter.

Therefore the averaged response of the two central strips (for each detector) can be considered proportional to the absorbed dose. Since, under these experimental conditions, the field profile is not uniform, uniformity corrections, given in the previous section, must also be included in order to calibrate the rest of the strips. Three measurements have been performed under the referenced conditions to calculate the calibration factors. In order to evaluate these factors, the data were analyzed as follows:

- the averaged signal for the central strips i gives L^i_{st};
- the four values L^i_{st} are divided for the correspondent uniformed signal L^i_{un} and then averaged, giving the factor <F>; this factor represents the relative

difference between the central strips' response in standard and in uniformity conditions;

- finally, the calibrated signal for the rest of the strips i can be calculated as (considering an irradiation with 100 MU):

$$F^i_{cal} = \frac{100cGy}{L^i_{un} < F >} \tag{3.29}$$

with its uncertainty:

$$\sigma^i_{cal} = F^i_{cal}\sqrt{(\frac{\sigma_{L_{un}}}{L_{un}})^2 + (\frac{\sigma_{<F>}}{< F >})^2} \tag{3.30}$$

Once the detector response has been calibrated to absorbed dose to water, QA measurements, such as percentage depth dose, penumbra and output factor were measured and analyzed (see following sections).

3.3.1.5 Percentage Depth Dose

The percentage depth dose (PDD) is defined as the percentage ratio of the dose measured along the beam axis containing the isocenter at different depths of water "d" compared to its maximum value, when SSD = 100 cm:

$$PDD(d) = \frac{Dose(d)}{Dose(d_{ref})} \cdot 100 \tag{3.31}$$

For an irradiation performed with a 6MV photon mode, the maximum value of dose is occurring at a reference depth in water of 1.5 cm and a field size of 10 × 10 cm^2. In order to characterize the DSSSSD as a dosimeter, we compared the dose measured with our system at 1.5, 3.5, 5.0, 10, 15 and 20 cm in solid water depth (red points) with those measured by a Farmer type ionization chamber (black line) at the hospital under clinical reference conditions (10 × 10 cm^2 field, water phantom surface at the isocenter plane, SSD = 100 cm, variable depth on water). The PDD was estimated by averaging the calibrated dose signal of the four central strips for the two detectors (strip number 16, 17, 48, 49) and the errors were estimated propagating the uncertainties associated to the calibrated dose for each strips. The results were normalized to the averaged value of the absorbed dose of the central strips under the reference conditions and shown in fig. 3.17.

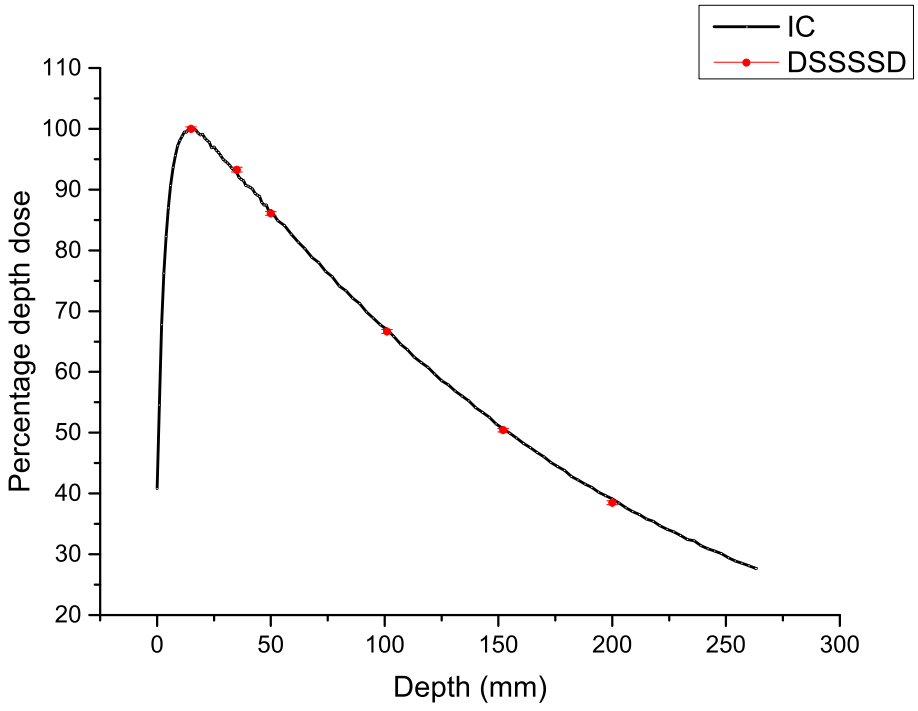

FIGURE 3.17: Percent depth dose measured by the IC (Farmer type) of the 6 MV clinical linac used in this experiment (black curve) and the DSSSSD (red circles) at different depths in solid water

Depth in solid water (mm)	PDD for DSSSSD	PDD for the IC
15	100	100
35	93.27 ± 0.39	92.78
50	86.10 ± 0.33	86.55
100	66.65 ± 0.31	67.00
150	50.42 ± 0.29	50.88
200	38.48 ± 0.29	39.11

TABLE 3.2: Comparison between the PDD values with the new detector and the IC

As it can be read in table 3.2, the agreement between the detector data and the QA measurements using a Farmer-type IC is below 1 %, in addition, the simulated data with the Geant4 toolkit shown in [7], also had an agreement better than 1% thus enhancing the performances of this new system as dosimeter.

3.3.1.6 Penumbra

Penumbra can be defined as the region located between 20% and 80% of a reference dose level, along the X and Y directions. For a symmetric field, the reference dose level is the one located at the central axis of the beam. Our studies of penumbra have been done with asymmetric fields of 5 × 10 cm^2 covering half of the detector active area, respectively at left (L) and right side (R) of the detector, along the X-axis (transversal direction). The same study was repeated in the perpendicular direction using asymmetric fields of 10 × 5 cm^2 covering the upper (U) and lower half (D) of the DSSSSD sensitive area, along the Y-axis (longitudinal direction). The measurements were carried out irradiating the system with 100 MU, at a SSD = 100 cm and 1.5 cm of depth in water.

Fig. 3.18 shows the response in absorbed dose of the different strips when the system is irradiated under the conditions cited above. The upper chart represents the dose response for the radiation fields of (5 × 10) cm^2. Black dots represent the response of the upper detector while, blue ones give the response of the lower detector when the radiation field is covering the left part of the detector area (L). Red dots show the response of the upper detector instead, violet ones, the response of the lower detector when the radiation field is delivered covering the right part of the detector area (R).

Bottom image refers to the dose response for a field size of (10×5) cm^2. Blue dots represents the response of the lower detector while, black ones are given the response of the upper detector when the radiation field is covering the top part of the detector area (U). Violet dots gives the response of the lower detector and red ones are given the response of the upper detector when the radiation field is delivered covering the bottom part of the detector area (D).

The dose profiles have been fitted by the sigmoid function f(s), defined as follows:

$$f(s) = a + \frac{b-a}{1+e^{c(s-d)}} \tag{3.32}$$

where a, b, c and d are the fitting parameters (given in table 3.3), and s refers to the strip number.

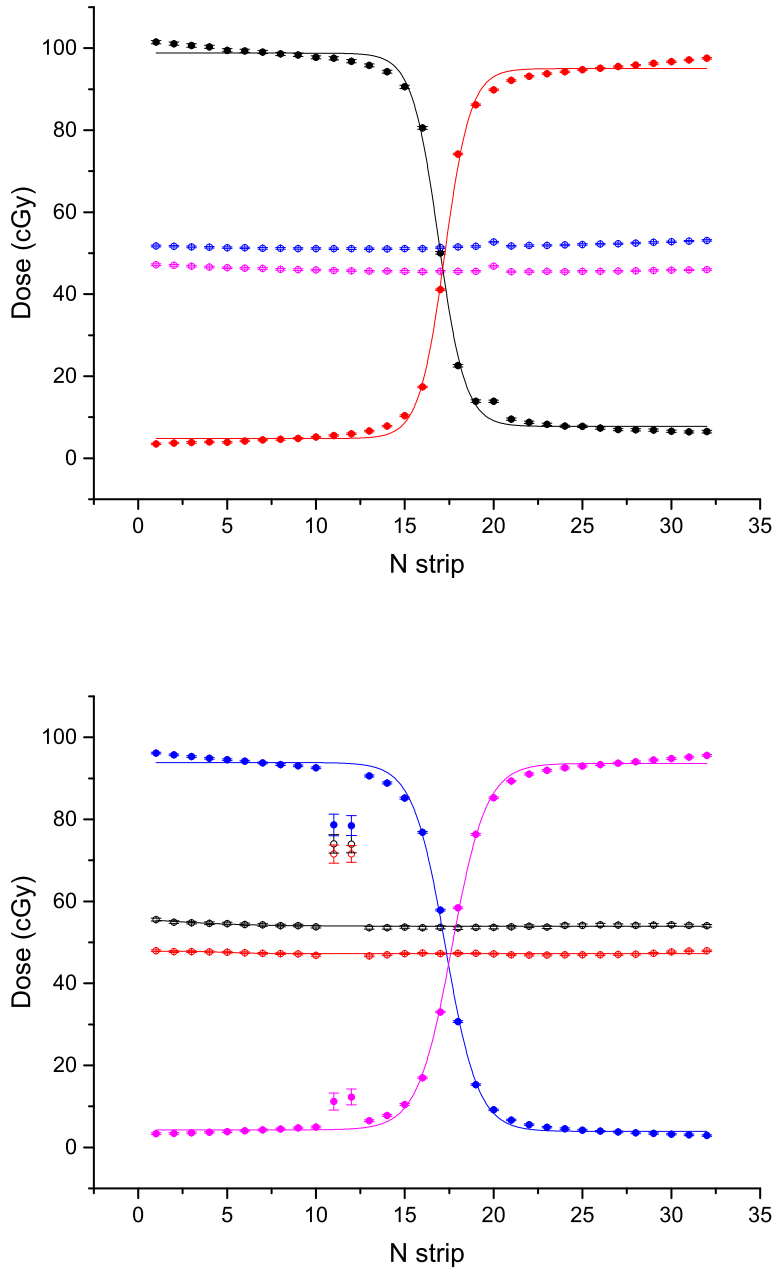

FIGURE 3.18: Top image: Response in absorbed dose for the detector irradiated with a field of (5 × 10) cm^2. Black dots show the absorbed dose for the upper detector when the field covers the left part of the detector active area; Blue points show the absorbed dose of the lower detector irradiated with the same field. Red dots are for the field covering the right part of the upper detector. Violet points represent the dose response for the lower detector under this condition. Bottom image: penumbra study with asymmetric field (10 × 5) cm^2 covering respectively the upper and lower part of the DSSSSD. As for the top image, black and blue dots represent the response in dose of respectively the upper and lower detector when the field is covering the upper part of the detector area, while, red and violet give the response in dose of respectively the upper and lower detector when the field is covering the lower part of the detector area.

The functions f(s) are represented in fig. 3.18 for the irradiations cited above (L, R, U and D). In this figure, we can assert that the experimental data are well described by eq. 3.32.

Using formula 3.32, the penumbra Δx is calculated as:

$$\Delta x_{pen} = \frac{2}{c} ln4 \times w. \tag{3.33}$$

where the factor w is the strip width (0.2 cm). Results are shown in table 3.3.

In the cross plane, corresponding to the field (5 × 10) cm^2, the penumbra estimation is of the order of (4 ± 1) mm. Meanwhile, in the in-plane (for fields of (10 × 5) cm^2), the penumbra is greater, around (5 ± 1) mm. These results are consistent considering the geometry of the linac head and how the asymmetric fields are shaped: fields in the in-plane direction corresponds to the motion of the collimator jaws, while, fields in the cross-plane are produced by the motion of the leaves of the Multi-Leaf Collimator of the linac, that are far from the source, leading to a sharper field variation in this direction, according to the results obtained here.

field (cm^2)	a (cGy)	b (cGy)	c (n^o strip^{-1})	d (n^o strip)	Δx_{pen} (cm)
5×10 L	7.76± 0.42	98.80± 0.54	1.34 ± 0.07	16.90 ± 0.04	4.14 ± 0.19
5×10 R	95.02± 0.42	4.80± 0.44	1.38 ± 0.07	17.25 ± 0.04	4.01 ± 0.19
10×5 U	3.91± 0.33	93.86± 0.34	1.09 ± 0.04	17.29 ± 0.03	5.08 ± 0.11
10×5 D	93.65± 0.33	4.27± 0.32	1.03 ± 0.03	17.65 ± 0.02	5.37 ± 0.11

TABLE 3.3: Penumbra fit values

3.3.1.7 Output factor

The output factor (OF) is defined as the ratio between the dose given for a field size A×A and the dose under referenced conditions (field (10 × 10) cm^2) at a given SSD and depth in water, in the center of the beam:

$$OF(A \times A) = \frac{Dose(A \times A)}{Dose(10 \times 10 cm^2)} \tag{3.34}$$

OF is usually checked for QA purposes and, in general, it is measured using ionization chambers or silicon diodes. Here the output factor measured using the

DSSSSD are compared with the ones considered for the QA measurements at the hospital. The measurements were performed at a depth of 1.5 cm of solid water, a SSD of 100 cm, 100 MU delivered by the linac and 1×1, 2×2, 5×5, 8×8 and 10 × 10 cm^2 field sizes.

field (cm^2)	DSSSSD	IC	Difference (%)
1 × 1	0.71±0.03	0.65	9 %
2 × 2	0.87±0.08	0.78	11 %
5 × 5	0.90 ±0.03	0.89	1 %
8 × 8	0.94 ± 0.04	0.96	2 %

TABLE 3.4: Output factor for the DSSSSD and the IC

In order to estimate the dose at the central axis of the beam, the dose values of the four central strips of the DSSSSD were averaged. Being the detector active area of 6.4 × 6.4 cm^2, for the measurements with a field size A×A smaller than those dimensions, a correction factor of 6.4/A has been included for a correct evaluation of the output factor.

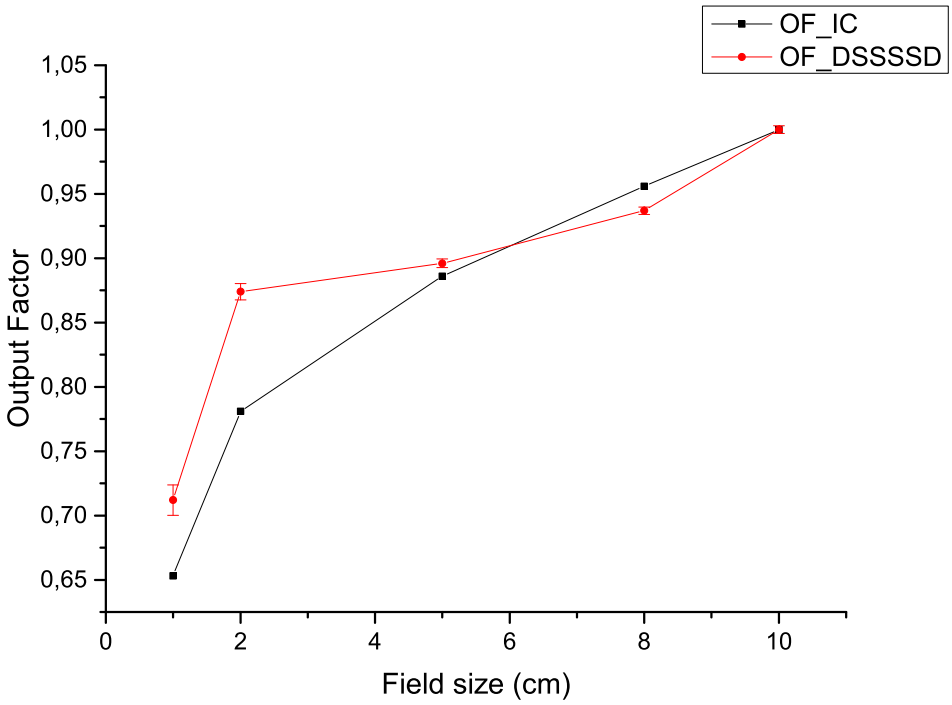

FIGURE 3.19: Comparison between the output factor measured by a IC (black curve) and the one given by the DSSSSD (red curve)

Results are collected in table 3.4 and represented in fig. 3.19. For small field sizes (1×1 and 2×2 cm^2), the detector measurements show a discrepancy of 9 % compared to the QA measurements of the IC. One reason is that, because of the strips' dimensions, the output factors for small field sizes are heavily influenced by any misalignment of the detector respect to the center of the beam Moreover, the factor 6.4/A used to correct the measured OF is just a geometrical approximation. Thus reliable results are obtained for field size greater or equal than 5×5 cm^2 with an agreement of 1-2 %.

3.3.1.8 Dose threshold

In the previous feasibility study performed in [7], it was observed a saturation of three boards out of four of the electronics used for the signal processing, provoked by a reset value of the voltage higher than the nominal 5 V. Such effect was producing a dose threshold (9.4 ± 0.2) cGy below which no significant informations could be given, being the dose different for each strip of the same board. In this work, this problem has been fixed by lowering the referenced value of the reset in order to never overcome 5 V.

As seen at the beginning of this study, two detector strips showed a non-reproducible results. This problem was caused by the electronic chain associated to them which was consequently revised and fixed. Due to this fact, the calibration under standard conditions (described in section 3.3.1.4) had to be repeated and applied to these measurements.

Fig. 3.20 shows the response for each strip of the detector (in the figure strips 1-32 for the upper side and 33-64 for the lower side) at low monitor units irradiations (2, 4, 6, 8, 10, 15 and 20 MU). The irradiation conditions correspond to the standard ones: field (10×10) cm^2, SSD = 100 cm and 1.5 cm of depth in water. All the strips have a reproducible response, except strip 53, which would not be considered in the analysis. The results show that beam profiles measured are similar to the one showed in fig. 3.11 for a depth in water of 1.5 cm.

Regarding to the uncertainties, the absolute ones are similar for all the irradiations, but, being 100 ms the sampling time of the data acquisition, at very low doses, the number of samplings is too little, leading to results with high relative uncertainties.

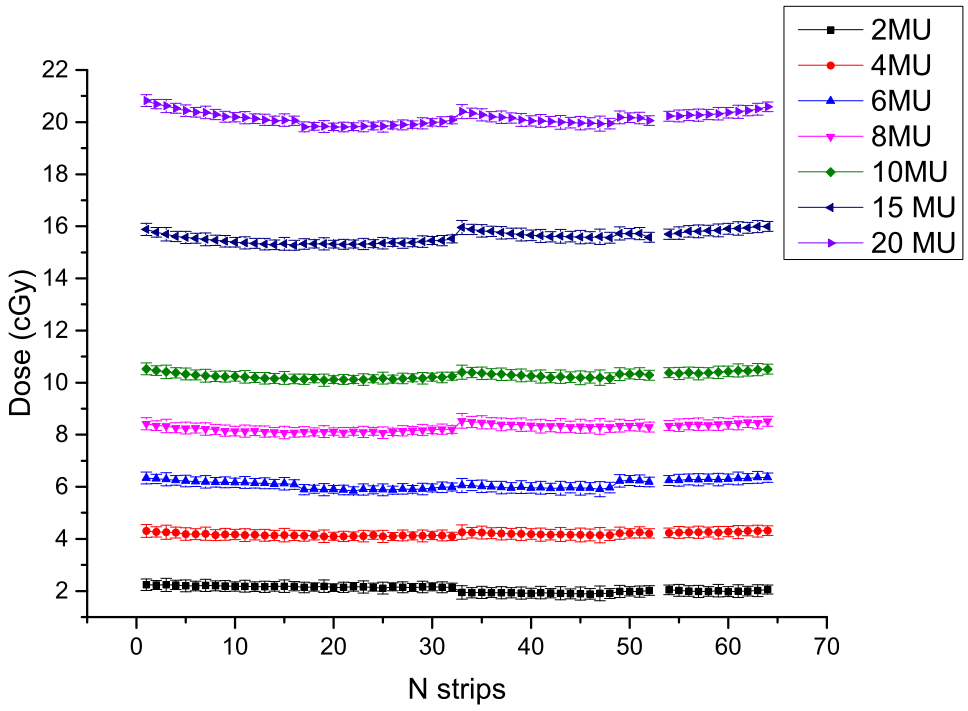

FIGURE 3.20: Measurements at low doses for 2, 4, 6, 8, 10, 15 and 20 MU delivered by the linac, for each strip of the detector, after applying the calibration factors.

Thus for an irradiation of 2 MU, the measured absorbed dose is (2.08 ± 0.25) cGy with a relative uncertainty of 12 %. Instead, for a fluence equal or greater to 10 MU, the dose responses obtained have an uncertainty lower than 2.5 % is obtained (in fact at 10 MU the dose obtained is (10.2 ± 0.2) cGy).

3.3.2 Dose calibration in treatment conditions

As stated at the beginning of this chapter, the system described in this section is going to be used to verify complex radiotherapy treatments. Therefore a new calibration in treatment conditions is needed. This implies to perform measurements of the device being irradiated at different angles, which response is then calibrated in absorbed dose to water. After having calibrated the detector response in this new configuration, the dose map in the axial plane is obtained through a forward-back projection of the strip data at different angles.

The angle between the detector and the beam direction can be changed in two ways: the first one would be rotating the gantry (of an angle θ_g) and the other

rotating the phantom (of an angle θ_p), considering as initial position the one pictured at the left of fig. 3.21 in which θ_g= θ_p= 0°.

From here on out, under the configuration $\theta_p = 0°$ and $\theta_g = 0°$, the detector chip with its strips parallel to the beam axis will be referred as detector 1 (which was the upper detector in the measurements under standard conditions), the other one as detector 2 (which corresponds to the lower detector in standard conditions, see section 3.3.1). θ_p, the rotation angle of the phantom, also corresponds to the rotation angle of the strips of detector 1. For detector 2, when the phantom is rotated of an angle θ_p, the strips are at an angle (θ_p + 90°). θ is the realtive angle between the strips and the beam direction. For detector 1 is $\theta = |\theta_p$ - $\theta_g|$, fig. 3.21, while, for detector 2, it would be $|\theta_p + 90° - \theta_g|$.

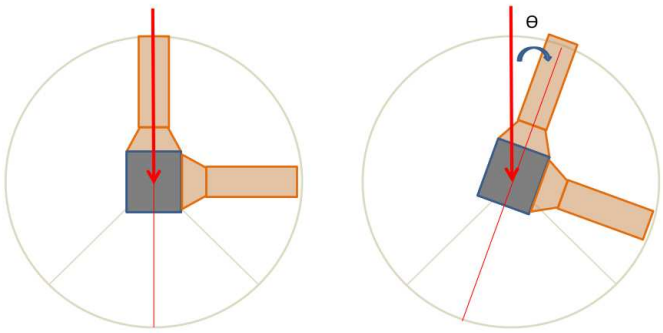

FIGURE 3.21: Left: detector located at the isocenter of the beam (drawn with a red arrow), with $\theta_g = \theta_p = 0°$; right: detector 1 rotated of an angle θ, while detector 2 is at an angle θ + 90°.

3.3.2.1 Detector positioning

It is important to center the detector respect to the beam axis once it is placed on the treatment couch. To check the correct alignment, a test was performed by irradiating the system with a rectangular field of size smaller than the detector dimensions. In this specific case, a field of (3 × 10) cm^2, centered at the isocenter has been delivered at $\theta_g = 0°$ and $\theta_g = 90°$ to verify the correct alignment respectively in the horizontal and vertical directions.

In fact, in the new system, as stated above, the strips of the two detector chips are forming an angle of 90°. For this reason, it is possible to center in the horizontal and vertical directions with two irradiations delivered at two gantry angles θ_g

equal to 0º and 90º, maintaining the phantom angle fixed at $\theta_p = 0º$. In this way, by studying the profiles, it was possible to know the detector displacement by adjusting the data to the double sigmoidal function f(s):

$$f(s) = \frac{A}{1 + e^{\frac{-s-c+w1/2}{w2}}} \left[1 - \frac{1}{1 + e^{\frac{-s-c-w1/2}{w2}}} \right] \tag{3.35}$$

where A, c, w1 and w2 are adjustable parameters and s is strip number. In particular, the parameter c represents the displacement of the detector with respect to the beam axis center.

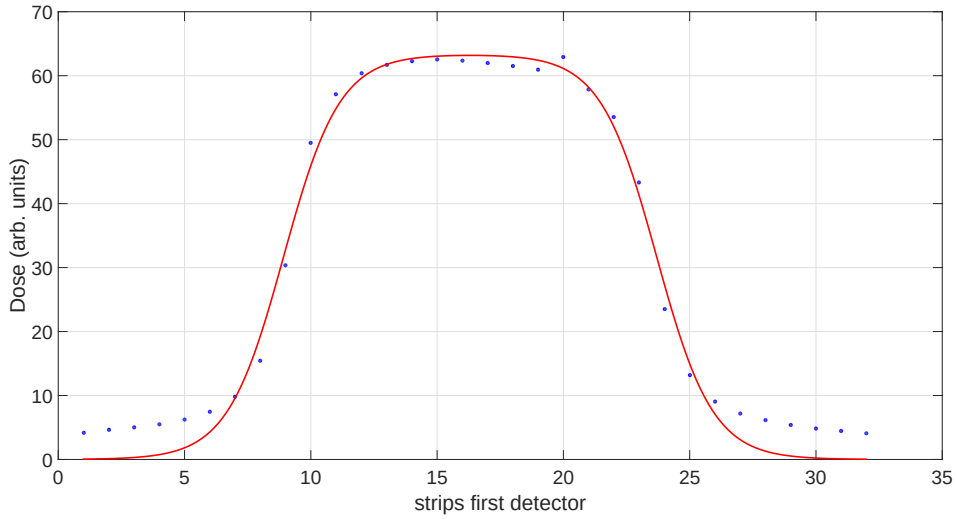

FIGURE 3.22: Absorbed dose in arbitrary units in function of the detector strips for an irradiation field of 3 x 10 cm^2 centered at the isocenter. The experimental data are plotted as blue circles, while, the red line represents the fit with equation 3.35.

If the detector is located at the isocenter, the parameter c is expected to be equal to 16.5 (between the two central strips 16 and 17). Fig. 3.21 shows a scheme of the transversal plane of the phantom containing the detector. The experimental data and the fitting curve are shown in fig. 3.22.

The fit sets the following values for the parameters: A = 63.3 ± 2.6, c = 16.3 ± 0.2, w1 = 14.8 ± 0.5 and w2 = 1.1 ± 0.2. Thus, being c = 16.3 ± 0.2 and the element pitch of 2 mm, the detector displacement amounts to 0.4 ± 0.4 mm. The laser in the treatment room has a precision of 1 mm, thus, the centering of the detector is within the laser uncertainty. The same procedure was repeated by

irradiating the detector with a gantry angle of 90 °. This method allows to assure the positioning of the detector at the isocenter of the gantry.

3.3.2.2 Angular response

In order to characterize the system under treatment conditions (detector located in the rotating cylindrical phantom, as described in section 3.3.1), one has to study the strip response at different angles. In fact, the calibration factors calculated in standard conditions, with the detector active area perpendicular to the beam axis, must be corrected to take into account the new configuration of the system.

In order to do that, the detector response at different irradiation angles θ was studied, following these steps:

- A CT scan of the central section of the phantom, with the detector inserted in it, was performed. It was selected an area of (15 × 5) cm ^{2} and slices of 1 mm each were recorded along the coronal plane. Thus, it was possible to identify the axial plane where the detector is located.
- The CT image of the axial plane containing the detector was sent to the treatment planning system (TPS - Philips Pinnacle^3, [38]). The contourings of 32 strips were drawn and the TPS calculated the absorbed dose for each of them simulating a field of 15 × 5 cm ^{2}, 100 MU delivered at the gantry positions of 0º, 45º and 90º, with a uniform density in the whole phantom. These doses constituted the reference dose in water used in the calibration under treatment conditions.
- Measurements were performed maintaining the phantom angle fixed at 0º and positioning the accelerator gantry at 0º, 45º, 90º and -45º; an analogous study was carried out rotating the phantom at 0º, 45º, 90º and -45º and fixing the gantry angle at 0º. Here, we represent the first experimental configuration, for θ = 0º, 45º, 90º and -45º. After applying the calibration factors in standard conditions (section 3.3.1.4), they are plotted in fig. 3.23 and fig. 3.24 respectively.

It has to be noticed that the calibration factor in standard conditions does not correspond to the current configuration and therefore the calculated dose is not actually the absorbed dose to water at the position of the detector.

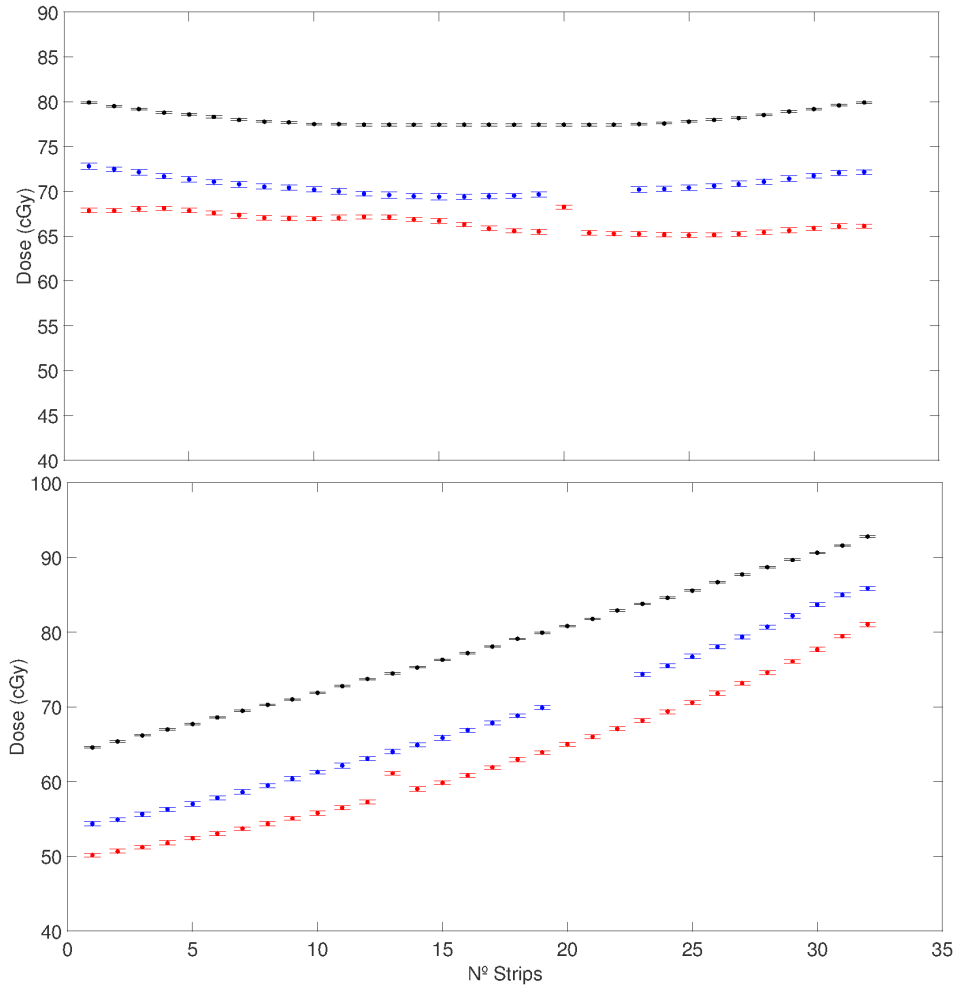

FIGURE 3.23: Dose response for the strips of the DSSSSD. Data of detector 1 are drawn in red, detector 2 in blue and the data from TPS in black color. The detectors' data should be given in arbitrary units as explained in the text. From top to bottom, the dose behavior at θ equal to 0^o and 90^o.

In the analysis, the response for detector 1 and detector 2 are shown respectively in red and blue color. These data are compared to the TPS calculations, which are represented with black dots. The detector experimental data show roughly the same trend as the ones simulated by the TPS, except for strips 20, 21 and 22 of the second detector, which suffered a breakdown and were not taken into account. The dose of detector 2 (the lower one when the detector was in the slab phantom) is higher than detector 1 and this fact is due to the calibration used in the calculation that was done in the slab phantom, where the plane of the detector active area was perpendicular to the beam, being the effective point of measurement is established to be at the centre of the DSSSSD.

In fact, as explained in section 3.3.1, the two chips in the slab phantom differ for

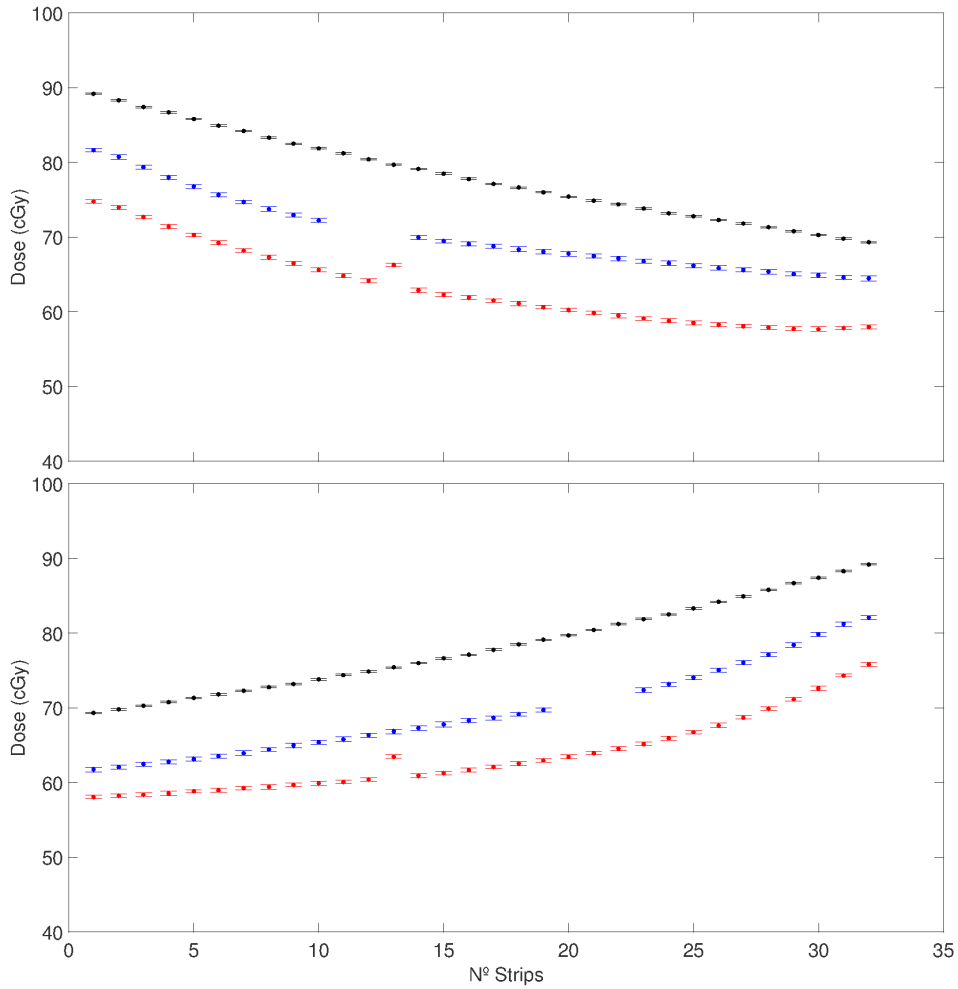

FIGURE 3.24: Dose response for the strips of the DSSSSD. Data of detector 1 are drawn in red, detector 2 in blue and are compared to data from TPS. From top to bottom, the dose behavior at symmetric angles θ = -45° and θ = 45°.

500 μm in depth and the difference in the absorbed dose by the two sensitive layers of the DSSSSD is mainly due to the shading effect of the detector itself and is not related to the absorbed dose in water. Because of this, a single readout for the dual chip has been used. This means that, in standard conditions, the response of the upper detector was decreased during the calibration, with reference to the response of the lower one that was increased to have, at the end, the same readout for both chips.

In this new position, there are no effects of shading and therefore, using the above calibration, detector 2 shows greater values respect to detector 1, which have to be corrected with the new calibration.

For a complete study, the response of the single strip i as function of θ was studied to analyze the possible dependence of the calibration factor with the angle of irradiation. Figure 3.25 shows the behavior of the side strips (N° 1 and 32) for different angle irradiation. Black dots represent the TPS simulations, the red ones are the data of detector 1 and the blue ones of detector 2. Some considerations about the symmetry of the system can be done: in each detector, the pair of strips symmetrical to the detector symmetry axis, (i. e. strips N° 1 and 32, or 16 and 17, etc) can be compared for particular gantry angles. For example, for an irradiation at (θ_g, θ_s) the dose received by the strip N°1 is the same of the strip N° 32 for an irradiation at (-θ_g, θ_s) (or θ_g, -θ_s) and so on for the others.

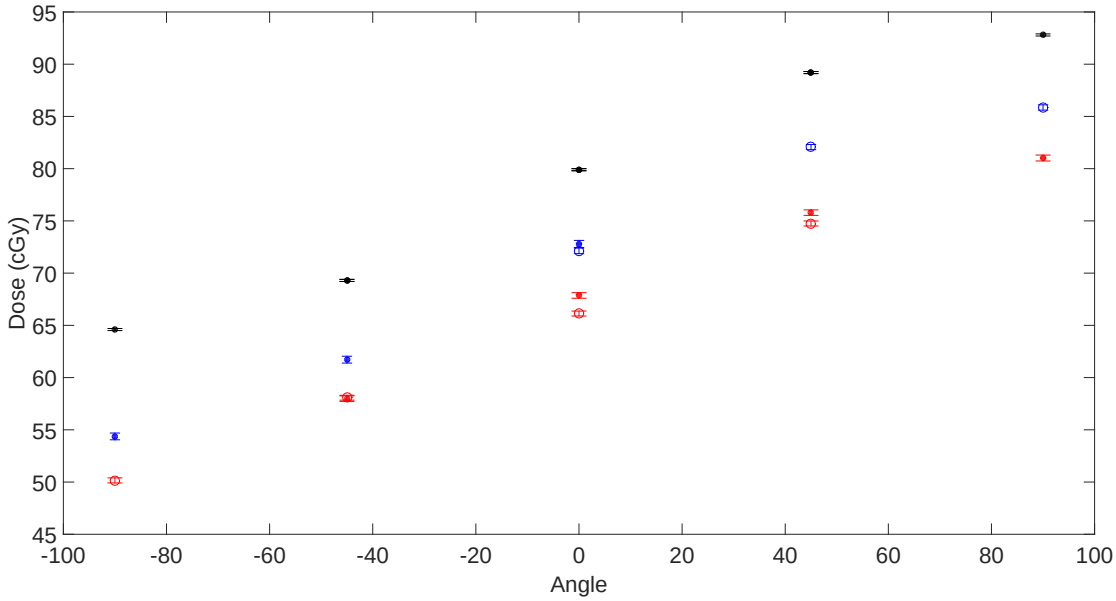

FIGURE 3.25: Dose response in function of the rotation angle θ. The response of the two lateral strips 1 (full dots) and 32 (empty circles) which cover symmetric angles; black points represent the TPS simulations, red and blue ones respectively for det1 and det2.

Thus the new calibration factors for each strip i and angle θ are calculated comparing the data with the TPS predictions through formula:

$$R^i(\theta) = \frac{D^i(\theta)}{D^i_{TPS}(\theta)} \tag{3.36}$$

and are reported in table 3.5:

These factors are different for each strip i, but can be considered constant with the rotation angle ($\mathrm{R}^i(\theta) = \mathrm{R}^i$). In fact, they have been calculated as the average of the

Strips	R^i
1	0.84 ±0.01
2	0.84± 0.02
3	0.83± 0.02
4	0.83± 0.02
5	0.82± 0.02
6	0.82± 0.02
7	0.82± 0.03
8	0.81± 0.03
9	0.81± 0.03
10	0.81± 0.03
11	0.81± 0.03
12	0.81± 0.03
13	0.81± 0.03
14	0.81± 0.03
15	0.80± 0.03
16	0.80± 0.03
17	0.80± 0.03
18	0.80± 0.03
19	0.80± 0.03
20	0.84± 0.03
21	0.80± 0.03
22	0.80± 0.03
23	0.80± 0.03
24	0.80± 0.03
25	0.80± 0.03
26	0.80± 0.03
27	0.81± 0.03
28	0.81± 0.03
29	0.81± 0.03
30	0.81± 0.03
31	0.81± 0.03
32	0.82± 0.03

Strips	R^i
1	0.89± 0.04
2	0.88±0.04
3	0.88±0.04
4	0.88±0.03
5	0.88±0.03
6	0.88±0.03
7	0.88±0.03
8	0.88±0.03
9	0.88±0.03
10	0.88±0.02
11	0.88±0.02
12	0.88±0.02
13	0.88±0.02
14	0.88±0.02
15	0.88±0.01
16	0.88±0.01
17	0.88±0.01
18	0.88±0.01
19	0.88±0.01
20	—
21	—
22	—
23	0.88±0.01
24	0.89±0.01
25	0.89±0.01
26	0.89±0.01
27	0.89±0.01
28	0.90±0.01
29	0.90±0.01
30	0.90±0.01
31	0.91±0.01
32	0.91±0.01

TABLE 3.5: Left: Calibration factors for the DSSSSD in the cylindrical phantom for detector 1; right: Calibration factors for the DSSSSD in the cylindrical phantom for detector 2.

calibration factors at each irradiation angle, and, consequently its uncertainties are calculated as the standard deviation of this average value. Finally, the absorbed dose for each strip 'i' is given by:

$$D^i_{cal}(\theta) = D^i(\theta)/R^i \tag{3.37}$$

and its uncertainty is calculated using the error propagation method of independent variables.

3.3.3 Dose map reconstruction with the dual chip SSSSD: experimental data

Once the strip response is calibrated in absorbed dose to water under treatment conditions, one can proceed to obtain the dose map in the axial plane for the verification of a given treatment. To do that, the algorithm described in section 3.2.4 was applied to the data collected with the detector at different angles.

The method to verify a hypothetical treatment was applied here. The first step was to define a tumor volume placed within the detector active area where the dose had to be uniform. After that, a treatment strategy is performed. It consisted of three incident beams (0^o, 120^o and 240^o) of fields of (2×5) cm^2. The full treatment with 50 MU per field was applied to the phantom that was displaced of 0.5 cm in both x and y directions in respect to the center of the detector and was rotated from 0^o to 90^o with a step of 5^o. As seen in section 3.2.4, the minimum rotation step to get two different projections is given by the detector dimensions, being for this system $\approx 3.6^o$. Thus, collecting the projection with a step of 5^o, we assured to acquire different projections, while maintaining a good angular resolution.

TPS simulates the treatment delivered on the phantom and gives the dose map. In order to know the TPS dose in the volume of each strip, they had to be drawn previously in the treatment CT. Fig. 3.26 shows a TPS dose map of the treatment in the plane virtually containing the detector, where the strips and tumor areas can be seen.

Because of the special geometric configuration of the DSSSSD, we can assume that one chip is acquiring data for a range of 0^o - 90^o and the other chip, at the same time provides data for an angle range of 90^o - 180^o. Thus the acquisition time is reduced to the half in respect to the previous system used in [2].

As mentioned in section 3.3.1, each detector chip active area is divided into 32 parallel strips 2 mm wide, thus, the dose map obtained by applying the projection-slice theorem consists of 1024 pixels. Fig. 3.27 shows on the top the TPS and the absorbed dose map reconstructed with the W1(SS)-500 detector; on the bottom,

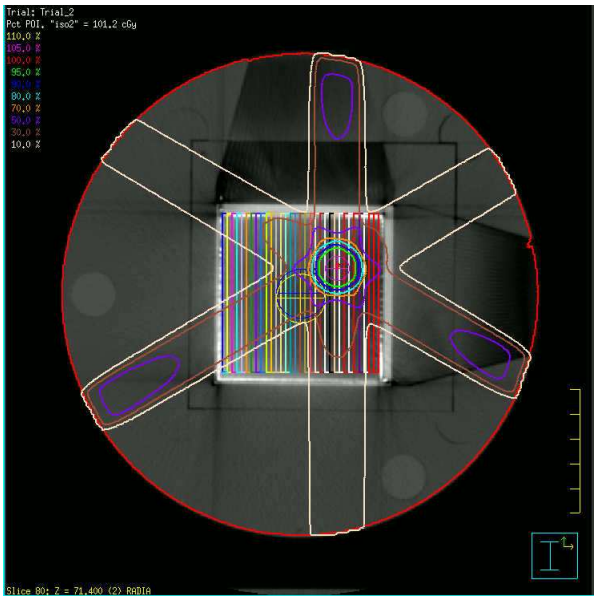

FIGURE 3.26: TPS image of the treatment given to the cylindrical phantom

the dose map established by the TPS is reconstructed using the new detector. Because of the detector rotation, the only valid pixels are the ones located inside the black circle. The smaller element pitch of the DSSSSD allows to obtain an image with a significantly improved resolution, while the bigger area increases the pixeleted dose map from 256 pixels to 1024. In addition, the presence of two chips improves the acquisition time which is twice as faster as the previous system. The results give a value of 92 cGy for the maximum dose in the circle and 100.3 cGy for the TPS, with a difference of 8 % between the experimental data and the simulations.

3.4 Final remarks

In this Chapter, a novel dual chip SSSSD designed by this research group was presented, characterized and calibrated as dosimeter and used for a 2D dose map reconstruction in the axial plane. The whole system for treatment verification comprehends, besides the novel detector, an in-house developed electronics, LabVIEW interface for data acquisition and preliminary analysis and designed phantoms.

Previous studies for the calibration of this system in polyethylene slab phantom as dosimeters were performed in [7]. In this work, this calibration had to be repeated, because of a breakdown suffered by the two detector's kapton cables,

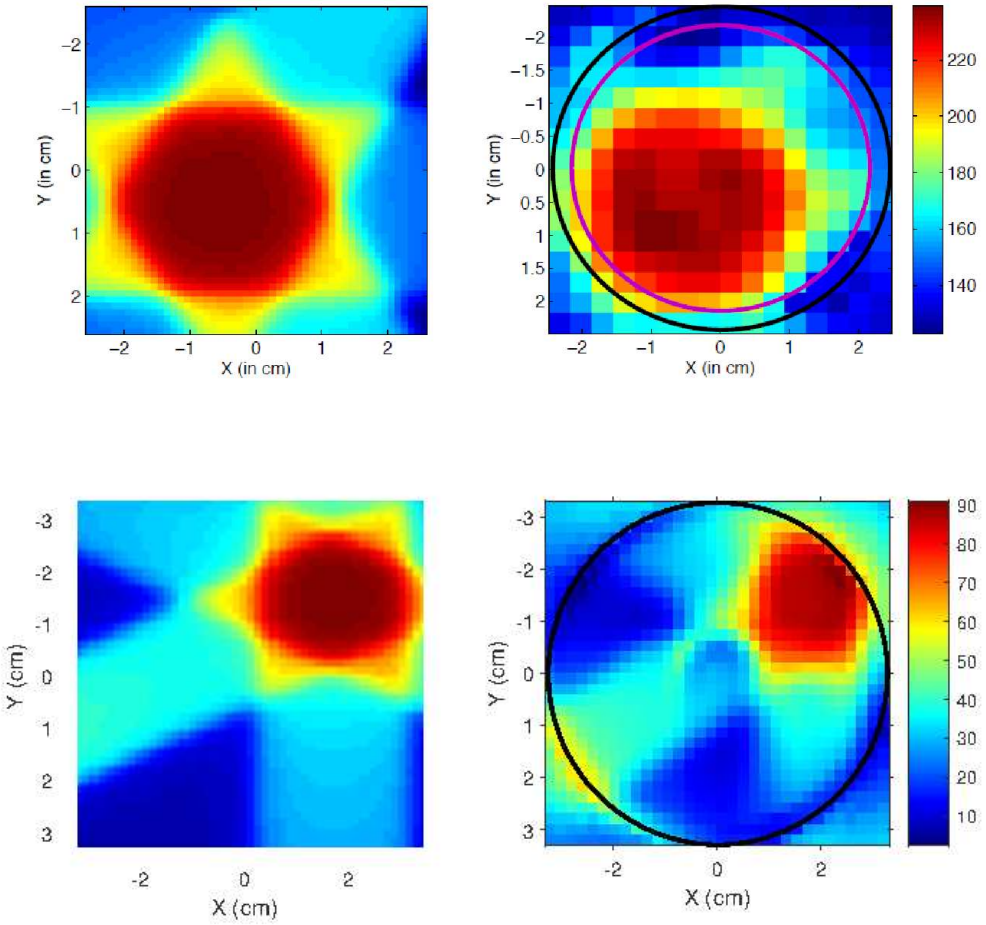

FIGURE 3.27: Top: TPS and W1(500)-SSD dose map reconstruction, from [2]. Bottom: TPS and D-SSSSD dose map reconstruction

which were repaired and consequentially modified from the original model. In addition, also the electronics was changed since three board out four of the ADC showed a saturation of the strips' signal due to a reset value of the voltage higher than the nominal 5 V.

As a first step, the detector is place in the slab phantom, in order to reproduce the standard conditions. In this configuration, its active area perpendicular to the beam direction.

Its response was characterized in absorbed dose to water; first of all, the detector's response to the radiation was studied: all the detector strips (except for strips N° 11 and 12 of the lower detector) showed a linear response to the irradiation with an agreement of the 0.1 % with an adjusted R^2 of 0.9997. The strips' signals

are thus calibrated in absorbed dose to water under referenced conditions. Then, QA measurements such as Penumbra and PDD were performed, and the results obtained were compatible to hospital measurements within 1 %. Output factor measurements show an agreement within 1-2 % in respect to hospital measurements when the detector area is irradiated with beam field sizes bigger than 5 × 5 cm^2. In relation to dose threshold, thanks to the ADC improvements, reliable measurements of the dose at a beam fluence of 2 MU are obtained with an uncertainty of 12 %, while, dose results with a relative uncertainty better than 2.5 % are found for doses equal or bigger than 10 cGy.

After the calibration procedure, the detector was placed in the rotating cylindrical phantom remotely controlled through the LabVIEW interface [39]. The calibration previously done for the slab phantom could not be applied straightforward, since, in the new position, the cavity dimension is larger than in the slab phantom. For this reason, the calibration had to be performed once more in this configuration. The detector area was irradiated at different rotating angles and its response was compared to the absorbed dose calculated by the TPS. Thus, new calibration factors are obtained for each detector's strip i and angle θ. These factors do not show dependence on the incident angle of the beam radiation, Once this procedure was completed, the detector was used for 2D dose map reconstruction in the axial plane. A complete treatment was simulated with the TPS and delivered to the phantom. The data were collected at different angles (from 0^o to 90^o, with a step of 5^o between two consecutive measurements) and an in-house developed algorithm for dose map reconstruction based on the filtered back projection of the Fourier transform was applied to obtain an axial dose map.

Respect to the previous model (W1(SS)-500) the dose map obtained presents a better spatial resolution thanks to the reduction of the detector element pitch (from 3 mm to 2 mm of the new detector) and a reconstructed dose map with 1024 pixels in respect to 256 pixels obtained before (however, the valid pixels are the ones inscribed) The absorbed dose in the tumor volume is measured with a difference of 8% in respect to the TPS simulations.

Despite of the improvements that this new system is offering in comparison to the previous model, we had to face several limitations which give room for future improvements: first of all, we want to mention the fragility of the kapton cables and of the ADC components which had to be repaired several times. Each time

that an ADC component is substituted or repaired the electronic chain suffers small changes that need to be corrected and included in the calibration.

In the final prototype, some elements that can prevent the cable damages such as polyethylene protections for the cables could be manufactured and installed in the phantoms; greater robustness of the electronics components would offer better performances.

A new algorithm base on iterative methods is going to be develop in order to provide a dose map reconstruction in the whole detector area (not only in the inscribed circle). In addition, this method can calculate dose distributions even though some of the detector's strips are not working properly.

Chapter 4

Physical and preliminary radiobiological studies with low-energy protons

In this chapter, an original work in the frame of dosimetry studies with low energy protons is presented. The whole methodology of the optimization of the beam characteristics is presented in a protocol which was established thanks to the studies carried out within this work.

Then, the possibility of using radiochromic films to perform absolute dosimetry with proton beams was investigated along the Bragg curve (at the plateau, maximum and distal fall-off region) and the feasibility of these studies are presented in section 4.3.

Hence, the chapter begins with the biological aspects of the interaction of ions with matter. Then it continues with the description of the methodology and the results obtained for dosimetry with protons of low energy. At the end of the Chapter, the results obtained irradiating breast cancer cells are shown.

4.1 Biological effects of radiation. Relative biological effectiveness

As already explained in Chapter 2, different types of radiations interact differently with matter. As a consequence, the damages produced in biological tissues are diverse depending on the cell type considered, the absorbed dose and also the type of the incident ionizing radiation.

As a matter of fact, photons leave sparse track of ionization events as they proceed toward the tissue. Ions, instead, present a high ionization density leading to larger damage respect to the one produced by photons.

A common way to analyze the different effects of photons and/or ions is by means of the cell survival curves. In the standard experimental protocol [40], cell proliferation is analyzed about 1-2 weeks after irradiation and cells are counted as survivors if they have formed a colony with more than 50 daughter cells. Hence, the survival fraction is given by normalization to the number of seeded cells. Usually, the cell survival S is described by using the linear quadratic (LQ) model [41]:

$$S(D) = exp(-\alpha D - \beta D^2)) \tag{4.1}$$

where D is the absorbed dose and α and β are experimentally determined parameters. The ratio α/β determines the shoulder of the survival curve (fig. 4.1) and indicates the cell repair capacity, which correspond to a value of 1-3 Gy for cells with high repair potential and close to 10 Gy for repair-deficient cells.

Usually, the curve has a descendant curvilinear behavior at low doses which indicates a minor efficiency of the cell destroy at low doses.

Since different types of radiations have different biological effects on living cells, the absorbed dose has to be weighted by the relative biological effectiveness (RBE) of the ionized radiation used for the treatment. The RBE of a certain ion radiation is defined as the ratio between photon absorbed dose and ion absorbed dose required to produce the same biological effect:

$$RBE = \frac{D_{phot}}{D_{ion}} \mid_{Isoeffect} \tag{4.2}$$

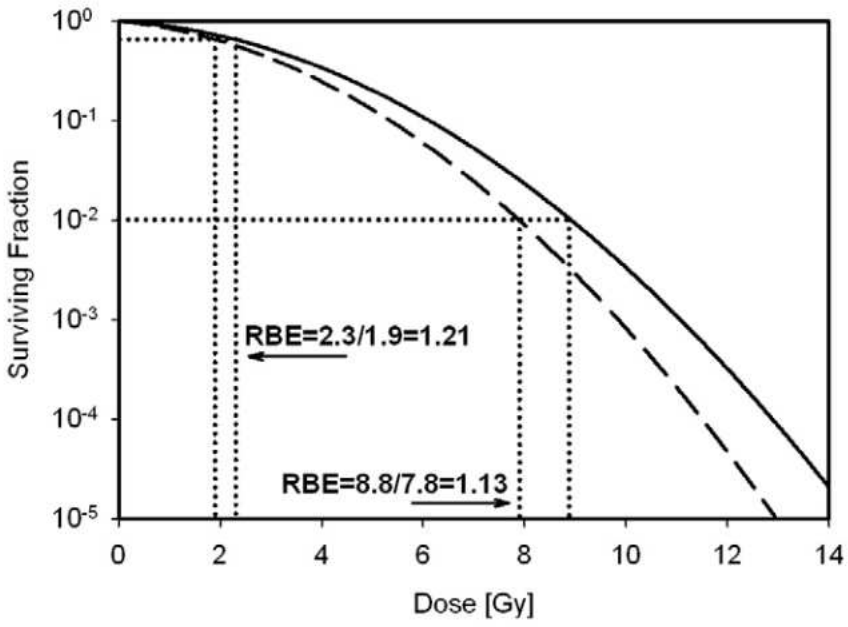

FIGURE 4.1: Cell survival curve for photons (solid line) and for protons (dashed line) as function of the absorbed dose [42].

The RBE depends mainly on three parameters: radio-sensitivity of the irradiated cell line or tissue, absorbed dose and LET. Here, the last two are argumented.

The dependence on the absorbed dose as shown in fig. 4.1, and in general, it is higher for lower dose levels and lower for larger doses owing to the shoulder shape of the cell survival curve.

The RBE value is intimately connected to the LET. In fact, higher is the LET, higher is the ionization density of the radiation considered, the radiation damage produced is more sever and this leads to an increase of the RBE. Since ions are characterized by high gradient LET at the end of their range in tissue (fig. 4.2), the RBE values must be defined for each region of the Bragg curve.

Considering the case of proton beams, as an average RBE for cell survival in the center of a typical spread-out Bragg peak (SOBP), data support a value of 1.15 at 2 Gy/fraction [42]. As said before, the proton RBE increases with LET: its value is about 1.1 in the entrance region of the SOBP, 1.15 in the center, 1.35 at the

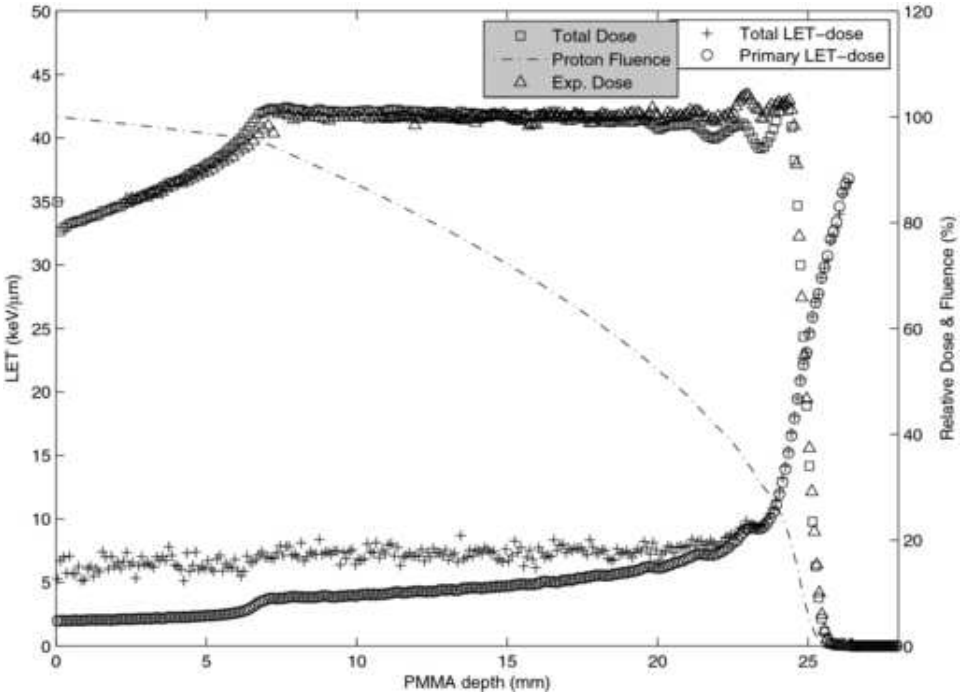

FIGURE 4.2: Total and primary LET-dose distributions for a proton beam in PMMA. From [43].

distal edge and 1.7 in the distal fall-off (when averaged over all cell lines, which may not be clinically representative) [42].

Many studies are addressed to quantify the realistic RBE value in order to be able to take it into account when it comes to planning treatments.

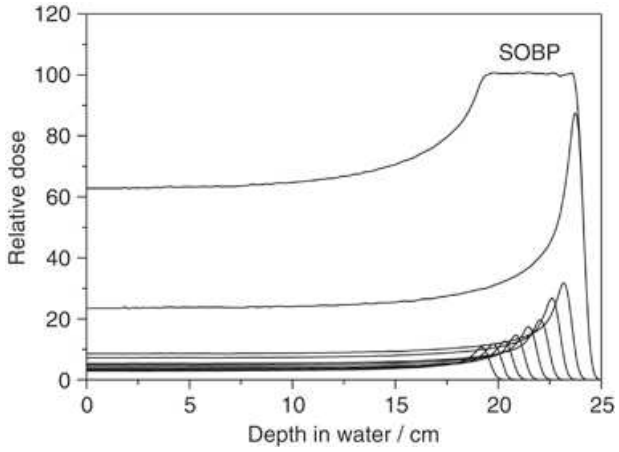

FIGURE 4.3: A view of the SOBP construction, showing its depth-dose distribution as superposition of many pristine Bragg peaks, from [44].

The depth–dose distribution of a single proton pencil-like beam is the Bragg peak with a sharp peak in depth (already mentioned in Chapter 2). In order to irradiate

the whole tumor target volume, a superposition of many Bragg peaks is needed, to obtain a homogeneous depth- dose distribution. Figure 4.3 shows the depth–dose distribution (solid line) in a homogeneous medium of such a superposition. It contains a number of Bragg peaks (dotted lines) in the same beam direction, but with different incident proton energies which is translated into different Bragg peak locations spread out in depth (SOBP). With respect to a single Bragg peak, the entrance dose is increased from a 30% to 80% due to the additional peaks. A uniform dose distribution is achieved within the target volume, (100 % of the total dose) and the sharp distal fall off is preserved. Thus, an RBE value of 1.1 is adopted in clinical practice with protons as a result of the averaged superposition of the RBE of the single Bragg peaks. However, at the distal fall off, only one Bragg peak is present, thus the RBE value in this part cannot be considered as 1.1 and many studies are conducted in this direction to find a good estimation of the RBE value in this region.

Some more recent works for the clinically used spread-out Bragg peaks found values up to 1.6 [42]. Because of the exponential dependence of biological effects on dose, the increase in biological effective dose from 1.1 to 1.6 cause a significant change in the biological effect.

4.2 Thesis core: Materials and methods

This section is dedicated to the description of the instruments and the methodology adopted to obtain the best conditions for dosimetry and biological sample irradiations with protons of low energy.

It starts with the description of the accelerator and the beamline used for the experiment, the protocol established to obtain an homogeneous beam profile over the samples with low currents, presenting the devices that have been used. An important part of this section is entirely dedicated to the description of the EBT3 Gafchromic films and their calibration in absorbed dose in standard conditions. These films were employed to check the beam uniformity and also for proton dosimetry (the results are shown in section 4.3).

Last, the device implemented for the direct measurement of the Bragg peak in air is described, together with an implemented example of a simulation using Geant 4 toolkit.

4.2.1 Tandem Accelerator

The Tandem accelerator is a special type of Van der Graff accelerator specifically proposed by three researchers: Bennett, Kallmann and Alvarez, and built for the first time by the High Voltage Engineering Company. A Tandem accelerator utilizes the terminal high voltage twice, thus obtaining output energies of a factor of two or more higher than those available in a single acceleration. It works in two stages (fig. 4.4):

- A source produces negative ions that are accelerated from ground to the positively charged terminal. Inside this terminal, there is a stripper (gas or solid target) which removes electrons from the incoming negative ions.
- Now, the positive ions experience a second boost of acceleration: they are repelled from the positive terminal and travel down the acceleration tube to ground voltage.

The resulting kinetic energy T depends on the charge of the positive ions, q:

$$T = qU + eU \tag{4.3}$$

where e is the absolute value of electron charge and U is the terminal voltage.

By means of analyzing magnets, it is possible to select the charge state needed for the experiment. The transport of the beam along the beam line is done with the help of dipole and quadrupole elements for the beam focalization, and bending magnets.

In contrast to single accelerating machines, the Tandem has both ends at ground, with the high voltage terminal in the middle. The charges are transported typically with a system of belts and pulleys.

The Pelletron type introduces an important modification in the charging process of the accelerator: in order to solve some drawbacks that were present in the charging belts of the Van der Graff, such as terminal voltage instability and susceptibility to spark damage, in Pelletron accelerators the belts are replaced by chains made of metal pellets separated by insulating nylon links. The chains are moved by pulleys. An electric field applied between a negatively biased inductor electrode

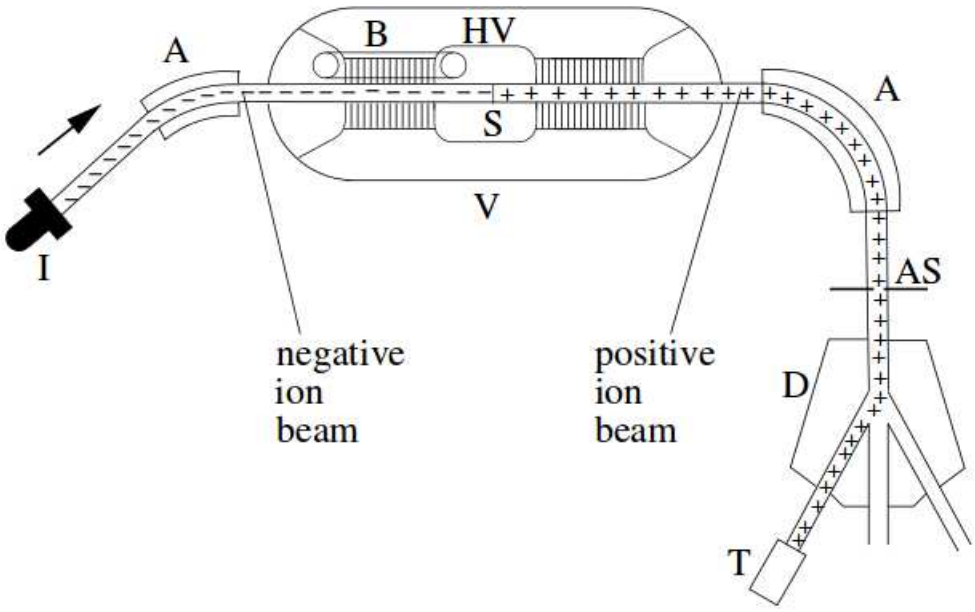

FIGURE 4.4: Inner structure of a Tandem accelerator. I: negative ion source, V: high-pressure vessel, B: belt generator, HV: high-voltage terminal, S: stripper foil or gas, A: analyzing magnet, AS: analyzing slit, D: deflecting magnet, T: target.

and the grounded drive pulley which pushes electrons off the pellets. Since these pellets are still inside the electric field as they leave the pulley, they retain a net positive charge. The chain then transports this charge to the high-voltage terminal, where the reverse process occurs. When it reaches the terminal, the chain passes a negatively-biased suppressor electrode which prevents sparking as the pellets make contact with the terminal pulley. The positive charge flows smoothly via the terminal pulley to the terminal. Typical charging currents are of 100-300 μA and high voltage up to 30 MV can be reached.

At CNA, a Pelletron Tandem accelerator, model 9SDH-2 of the National Electrostatic Corp. (NEC) company is installed, fig. 4.5. The maximum terminal voltage that can be achieved is of 3 MV. The ions can be produced by three ion sources made also by NEC:

- Alphatross, a source that generates ions from gases with radiofrequency techniques;
- SNICS II, a sputtering Cesium source, that produces ions by means of sputtering from solid targets;

- Duoplasmatron, a gas source, where the ion generation is produced in a discharge process in two steps.

Such ion sources are connected to an injection dipole magnet, which has a Mass-Energy Product (MEP) of 15 a.m.u-MeV. Alphatross and SNICS II sources are installed with a ±30 degrees, while the DuoPlasmatron is situated at 0 degrees with the orientation of the acceleration line. The magnet mentioned above can deflect negative ions of 70 keV and mass up to 240 a.m.u and inject them into the accelerator. The accelerated ions travel to a 90 degree magnet with a curvature branch of 1 m and 75 a.m.u of MEP, that can reach magnetic fields up to 13.5 kG. Such magnet selects the energy of the ions and, consequentially, their charge state. After this, a switching magnet allows to direct the beam towards one of the seven beam lines,

FIGURE 4.5: Picture of the 3 MV Tandem Accelerator at the CNA

as shown in fig. 4.6, positioned at 0, ±15, ±30 and ±45 degrees respect to the acceleration line.

The beam line used for this project is located at 30 degrees after the switching magnet and it is named *Basic Nuclear Physics (FNB) beam line*. It is dedicated to experimental study of nuclear reactions, characterization of detectors, dosimetric and radiobiology studies.

FIGURE 4.6: Top view of the seven beam lines coming out from the 3MV Tandem accelerator at CNA

4.2.2 Preparation of the FNB beam line and protocol for the beam characterization for radiobiology studies

One of the greatest challenges of this work is to obtain a homogeneous beam intensity profile at the position of sample irradiation. To do that, a protocol for the beam preparation was established, after many series of measurements, in order to have a stable beam with reproducible conditions.

In this paragraph, after the description of the beam line used, the devices dedicated to the detection and characterization of the beam will be presented, concluding with the beam preparation protocol adopted for this work.

4.2.2.1 Description of the FNB beamline

The protons are produced by the SNICS II source and their current is measured with a retractable Faraday cup close to the entrance of the beamline used for our studies, which is placed at +30 degrees at the exit of the switching magnet as shown in fig. 4.7. The most important elements for this work are:

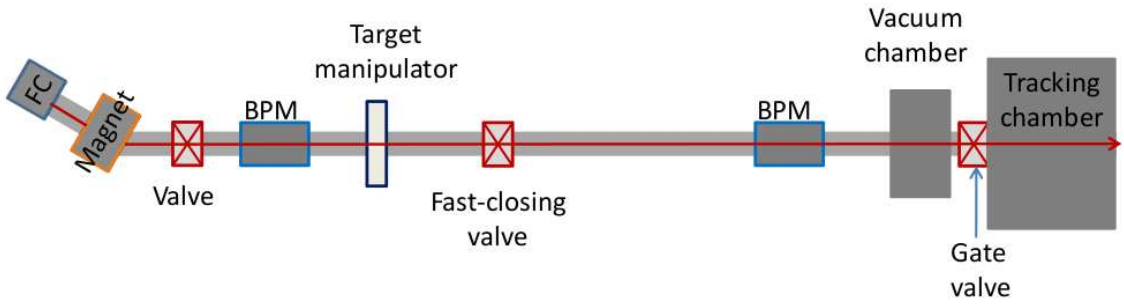

FIGURE 4.7: Beam line scheme. The tracking chamber, installed in this line, was not used in these measurements.

- two beam profile monitors (BPM1 and BPM2), manufactured by NEC (fig. 4.9), which provide information about the beam shape and position in X and Y coordinates.
- a manipulator with Au targets to scatter the beam and obtain a nearly homogeneous intensity beam profile impinging onto the samples to be irradiated.
- a fast-closing pneumatic valve with a closing-time of 100 ms, used as beam shutter to control the irradiation time.
- a thin vacuum exit window (50 μm thick Kapton, 44 mm diameter). It was mechanized in order to meet the requirements for the sample irradiation: due to its thickness, the protons do not lose a large amount of energy in crossing it, allowing to perform the sample irradiation in air. At the same time, such thickness is capable of maintaining a vacuum inside the beam line of the order of 10^{-6} mbar. The aperture of the window was chosen in relation to the irradiations with cell cultures (see section 4.3.3).

The vacuum exit window is placed at the end of the beam line at 5.2 m after the gold foil, and mounted together with an ionization chamber (IC). Directly behind the chamber a special holder with six positions for biological samples is placed (Fig. 4.8). The holder, specifically designed for housing the cell cultures, is also used for irradiations of the Gafchromic EBT3 films. The thicknesses of all the instruments used in the setup are summarized in table 4.1.

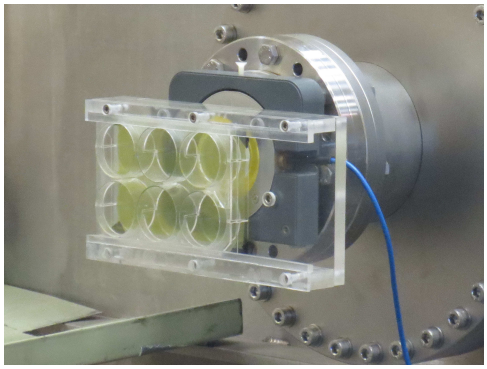

FIGURE 4.8: Experimental setup for the irradiation of the radiochromic film.

Target material	N°	Thickness
Au target	1	5.4mg/cm^2
Kapton window	2	50μm
Air gap	3	10mm
Kapton electrodes	4, 6, 8	7.5μm X3
Air gaps in the IC	5, 7	6.75mm X2
Air gap	9	13mm
EBT3 film (polyester)	10	125μm
EBT3 film (active layer, lucite)	11	28 μm
EBT3 film (polyester)	12	125μm

TABLE 4.1: Elements and correspondent thickness of the beam line components ordered as the beam crosses them.

4.2.2.2 Devices for beam detection and characterization

The elements used to perform the dosimetric studies are described here.

An IC is used to measure the proton fluence. It is a modification of a model from PTW: because of the low energy of the beam, special and dedicated instrumentation is required. For this reason this IC was constructed at GSI laboratories in order to have thinner electrodes suitable for low energy protons. The technical specifications of the chamber are: three parallel electrodes made of Kapton of 7.5 μm of thickness, forming two air gaps of 6.75 mm of thickness, which must be biased at 400 V.

The output of the IC is read with an electrometer; it is an instrument designed to measure small values of voltages, currents and charges. There are many different types and the most modern models (based on vacuum tube or solid state technology) can be used to make voltage and charge measurements with very low

leakage currents, down to 1 fA. They are frequently used for the measurement of radiation with ionization chambers. The electrometer used during these measurements is produced by Keithley company. The model is 6514, which offers 1 fA sensitivity, an impedance higher than 200 TΩ on input voltage measurements and charge measurements down to 10 fC [45].

An ion implanted silicon detector was used to measure the energy of the beam at the same position of the samples. This type of semiconductor detectors is the most used for the measurement of the energy of charged particles. They are made introducing doping impurities at the surface of the semiconductor by exposing the surface to a beam of ions produced by an accelerator. The concentration of the impurities is well controlled by changing the beam energy. This procedure is known as ion implantation and it is used to form n+ and p+ layers in the semiconductor wafer. Semiconductors with impurities have different Fermi levels [18], [46]. Once they are united in a junction, a depletion zone is formed in the semiconductor, which is sensitive to the passage of charged particles.

Thanks to the structure of the crystal, ion implanted detectors tend to be more stable and less affected by environment conditions than surface barrier detectors. Some of them are equipped with thin entrance windows, generally made of 34 nm of silicon equivalent material to protect them from light and so reduce the signal noise.

The detector used for our measurements is produced by ORTEC company and named "ULTRA ion-implanted-silicon detector". This model has been implemented mainly for alpha and beta spectroscopy. Both the entrance and the back contact are ion implanted. The entrance contact is an extremely thin (~ 500 $\mathring{A}$) boron implantation [47].

It was used a 500 μm thick since, for the energies used in this work, the protons lose all their energy in the silicon wafer. This silicon detector is biased at 50 V and its signal processed by a preamplifier (model ORTEC), an amplifier and then sent to the ADC. The program used for the acquisition is named OMQ-DATA. The resulting spectra are energy calibrated by using a triple alpha source (^{239}Pu-^{241}Am-^{244}Cm).

Radiochromic films were also used for the beam detection and characterization. Their calibration in absorbed dose under proton irradiations was studied in detail, and because of that, their characteristics and their use in this work will be extensively explained in the section 4.3.

4.2.2.3 Protocol for beam preparation

FIGURE 4.9: Beam profile monitor

Here we describe the function of the elements that were used for preparing the beam, together with the protocol established to obtain the best irradiation conditions. The method used to lower the beam current is presented and the beam scattering procedure is explained.

The beam profile monitors (BPMs, fig. 4.9) are used to center the beam in the beamline. These devices work as follows: a helical wire on a rotary drive crosses the beam vertically and then horizontally during each revolution. A cylindrical collector around the grounded wire collects beam-induced secondary electrons from the wire to provide a signal proportional to the intercepted beam intensity at every instant. These instruments are precise with currents of the order of few μA or higher. But such currents are too elevated for our dosimetry studies, since one cannot have an effective control of the dose given to the cells. Thus, the BPMs are used to center the beam with elevated currents and subsequently the current is lowered.

Generally, two are the most employed methods to decrease the current: by defocusing the beam with the quadrupole magnets (fast procedure) or decreasing the pressure of the gas used for the stripping process (nitrogen in this case), maintaining unaltered the focalization of the beam (slow method). The latest, despite it

is a time consuming alternative, is the most suitable for our measurements since the beam optics is not touched during this operation and the maximum beam intensity is maintained at the same position. The gas pressure is lowered until a beam current of tenths of nA is reached in the Faraday Cup at the entrance of the beam line.

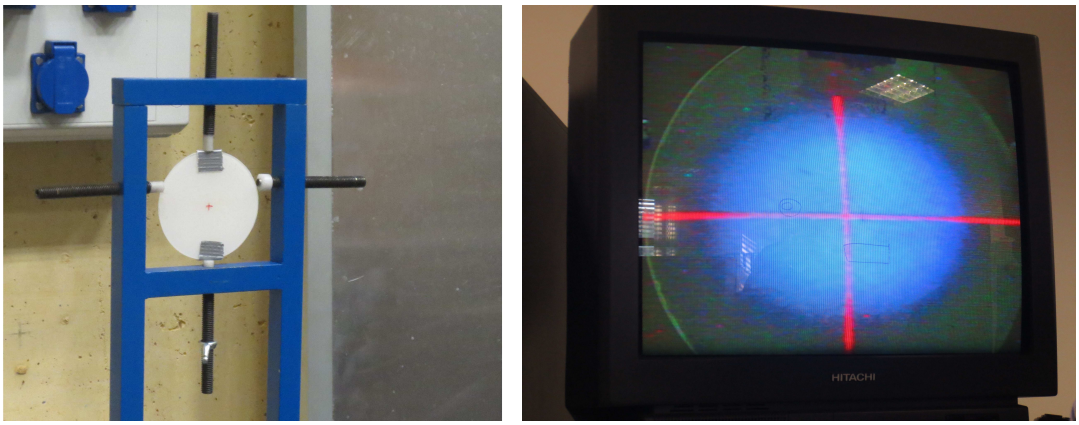

FIGURE 4.10: Fluorescent screen used for the beam alienation

BPMs do not give a precise information of the beam position when the current is so low. In order to check the position of the beam once the current has been lowered, a fluorescent screen placed just after the vacuum exit window and centered with a laser system is used as shown in fig. 4.10. Using the image of the fluorescent screen, fine adjustments with the steering magnets are performed to complete the beam alignment. Table 4.2 shows the accelerator parameters obtained after these operations.

Tandem accelerator parameters

Energy	5.233 MeV
Injection magnet	-823.96 G
Analysing magnet	3262.8 G
Switching magnet	-5084.51 G
Current Faraday Cup (source)	0.785 μA
Current Faraday Cup (after the stripping gas)	-100 nA
Current Faraday Cup (just before the entrance of the FNB beam line)	-8 nA

TABLE 4.2: Accelerator parameters used: energy, bending magnet values and currents in the Faraday cups along the accelerator.

Once current values and beam position reach the desired conditions, we take care of the homogeneity of the beam profile.

As stated in [46] and [48], the particle beam produced in an accelerator is usually not uniform, however uniformity can be obtained by intercepting the beam path with a diffuser. The material used as diffuser must be a good electrical conductor. One could relate the thickness of the diffuser used to the dispersion of the beam produced at the place of the irradiation as described in [46].

We did not perform such study, but instead, we made some empirical measurements with Au targets of thickness 2.0, 3.4 and 5.4 mg/cm^2 to choose the best one for our purposes. Gold is a heavy material which allows to use thin films (reducing straggling effect) for the needed angular scattering of the beam.

It is expected that by varying the thickness of the target, different beam distributions will be obtained.

As will be shown in section 4.3, the best beam profile (in terms of homogeneity) was obtained for 5.4 mg/cm^2 target thickness. Therefore this foil was the one chosen for our work.

4.2.3 EBT3 Gafchromic film

Since radiochromic films (introduced in Chapter 2) stand out because of their equivalence to soft tissue, low energy dependence (for therapy with electrons and photons) and high spatial resolution, they are an appropriate instrument to measure the dose spatial distribution [49]. EBT3 Gafchromic films are a category of radiochromic films largely used for this scope. The structure of GafChromic EBT3 films is comprised of a single active layer 28 μm thick, containing the active component (microcrystalline diacetylene suspended in gelatin), marker dye, stabilizers and other additives giving the film a very low energy-dependence. The active layer is between two transparent polyester substrates of 125 μm of thickness.

On exposure to ionizing radiation, it causes a solid-state polymerization via a free-radical mechanism, and the newly formed polydiacetylene chains exhibit a blue color. This is usually expressed in terms of optical density (see 2.2.1), which, in turn, can be correlated to the dose. This quantity correlates the dose that has been deposited in the sensitive layer. Fig. 4.11 shows an EBT3 film that has been irradiated with different dose values in six circular regions.

FIGURE 4.11: EBT3 film showing circles irradiated with six different dose values

EBT3 films differ from the previous models because of a special polyester substrate that prevents the formation of Newton's Rings interference patterns in images acquired using flatbed scanners. Also the structure of the EBT3 film is symmetric and eliminates the need with EBT2 of keeping track of which side of the film was placed on the scanner (see chapter 2, section "Radiochromic films"). EBT3 were initially designed for dose measurement in external beam radiotherapy, radiosurgery and brachytherapy. As a self-developing film, not requiring post-exposure processing, the film can be easily handled and analyzed.

Technical characteristics are listed here (some of them, particularly important for our work, are treated in more detail later):

- Analysis can be done measuring with a flatbed color scanner (fig.4.12);
- For dose studies up to 10 Gy, the red color channel is the more precise; for dose above 40 Gy, the best response is given by the green channel;
- Active layer incorporates a yellow dye useful for:

  Enabling multi-channel dosimetry;

  Decreasing UV/light sensitivity;
- Self developing in real time without post-exposure treatment;
- Low energy-dependence for photons and electrons (as we will see in Chapter 4, this condition is not always maintained when the films are irradiated with protons);
- Because of the composition of the layers (polystyrene and lucite) and their densities (1.06 g/cm^3 for polystyrene and 1.2 g/cm^3 for lucite) they are considered tissue equivalent;
- Coated on special polyester to stop Newton's Rings patterns from forming;
- High spatial resolution- can resolve features to at least 25 μm;

- Water resistant, can be immersed in water phantoms.

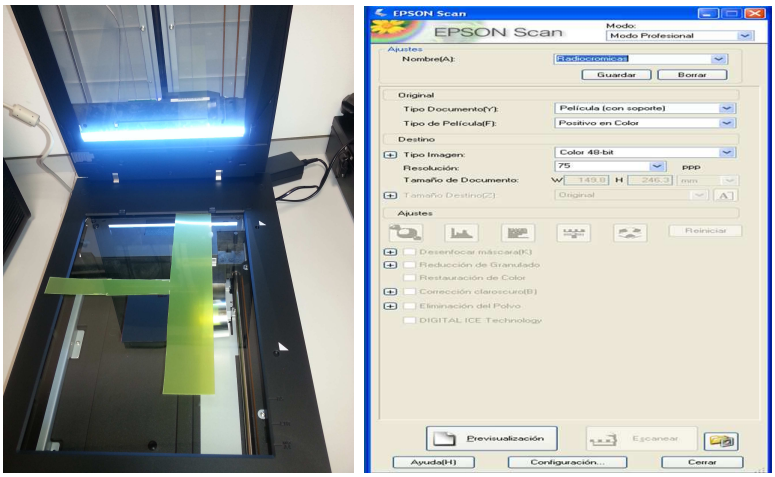

FIGURE 4.12: Epson perfection V700 photo scanner

The slopes of the response curves are different for each color channel. Each signal is comprised of a dose-dependent and a dose-independent portion, but the proportions are different in each color channel. The response in the blue channel has a relatively low slope because the signal has a weak dose-dependence. For the red channel, the signal is highly dose-dependent for doses up to 10 Gy. The green channel is the most suitable when it comes to determine higher doses.

Combining the response of the scanner with the commercial software ImageJ (for Java image processing), it is possible to calibrate in the RGB (red, green and blue) channels the film responses in dose values. In order to obtain the best results from the scanner images, there are several precautions to be adopted:

- Do not cover the calibration window of the scanner;
- Place the film at the center of the scan window;
- Use the scanner in the transmission mode;
- In the software interface for the image acquisition, select:

  Professional Mode;

  Transparency;

  Positive film;

  48 bit color to scan in RGB mode;

Spatial resolution of about 75 dpi (dots per inch) for most applications;

Select "No color correction";

- Acquire the image in .tiff format [50].

4.2.3.1 Calibration in absolute dose with photon fields

The correlation between the digital signal given by the scanner and the absorbed dose of the film represents the calibration of the film itself. Such calibration of the films was carried out at the University Hospital Virgen Macarena (HUVM) in Seville, using a 6 MV photon beam produced by a clinical linac. The calibration is done in standard conditions, which are:

- 100 cm of source to surface distance (SSD)
- a field size of 10×10 cm^2
- 1.5 cm of solid water above and 8 cm below the film (in order to assure the complete backward dispersion of the secondary electrons)

Under these conditions, 100 monitor units (MU) delivered by the clinical linac correspond to 1 Gy of absorbed dose [51].

One sheet of EBT3 was cut in 20 pieces, and then one by one, they were irradiated under the reference conditions only by changing the monitor units delivered by the accelerator, covering a range of doses of 0-15 Gy. In principle, this calibration is valid for films of the same package. Therefore, it is important to repeat the calibration each time a new film lot is used. The optical density of two different packages can be expressed as $OD_1 = k\ OD_2$. Thus, since $Dose_1$ (from the first lot) is given by:

$Dose_1 = F_{cal}(OD_1)$ where F is the calibration function which depends on the OD, the dose for the second stuck can be easily calculated with:

$Dose_2 = F_{cal}(k\ OD_2)$.

For calculating the factor k, two pieces of film, with an irradiation of 0 and 200 MU, are analyzed:

$$k = \frac{netOD_{cal}(200MU)}{netOD(200MU)} \tag{4.4}$$

where netOD$_{cal}$(200MU) is the OD(0MU)-OD(200MU) in calibration conditions, and netOD (200MU) = OD(0MU)-OD(200MU) for the new lot.

Other corrections can be included in the film analysis (as the multichannel correction [51]) especially when such films are used for clinical machine checkings, but for our scope such corrections can be avoided.

Subsequently, the films were analyzed with the Epson perfection V700 photo scanner installed at the CNA. The plot of the netOD (defined in Chapter 2) as function of the absorbed dose in color of the three channels RGB (red, green and blue) represents the calibration curve (fig. 4.13).

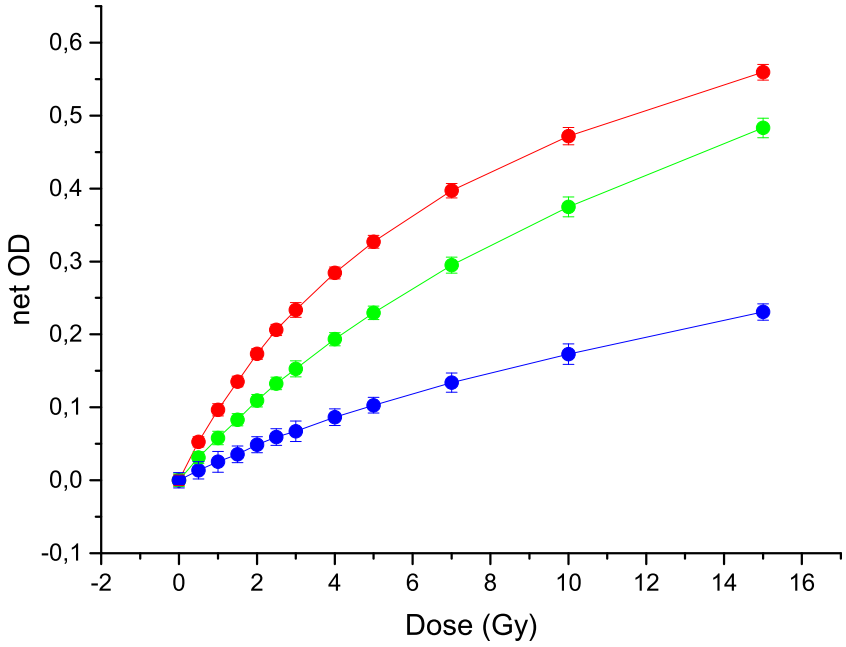

FIGURE 4.13: Calibration of the EBT3 films in absolute dose for RGB channel colors.

As described previously, the red channel is the most sensitive in terms of dose response [52] up to 10 Gy, since its slope is higher compared to the green and blue channel (as shown in fig.4.13). For radiobiology purposes, the dose range of interest is located below 10 Gy, thus, this channel has been used to calibrate the films.

4.2.4 Setup for dosimetry in the Bragg peak degrading the beam in air

In order to be able to have a direct measurement of the Bragg peak position in air, some modifications needed to be added to those already done in the beam line.

The diameter of the exit vacuum window had been initially fixed to 44 mm, in order to allow irradiation of sufficiently large samples. For the case of beam degradation in air, this aperture diameter was reduced to 20 mm by placing an internal collimator. The reason is that the initial diameter of 44 mm causes a significant bending of the window when the beamline is in vacuum, whereas with 20 mm diameter this bending is negligible. A large bending gives rise to appreciable differences in the distances traveled in air by different protons within the same beam. This is a problem when studying the response of radiochromic films in the Bragg peak region, which is very sensitive to small energy differences. A study of the effect of the bending of the kapton window is shown in paragraph 4.3.1; a silicon detector is used to measure the energy loss in different regions of the window, in order to establish if the bending causes a significant variations on the proton beam energy.

The final part of the setup, after the IC, was also modified for these measurements with the beam degraded in air. The holder for the radiochromic films was kept out and a tool equipped with a precision linear driver, provided by GSI (fig. 4.14) was installed. This driver mainly consists of a table with adjustable height, equipped with a central holder where samples or detectors can be mounted, and which can be displaced linearly; the displacement is measured with micrometric precision by means of a Mitutoyo micrometer. In our case, the holder was used to host a second IC.

4.2.4.1 Monte Carlo simulation of the setup using a Geant 4 application

Monte Carlo calculations, using Geant4 (simulation tool for the passage of the particles through the matter [53], version 10.2), were performed to simulate this setup and calculate the energy loss through these elements. The simulations were conducted introducing some modifications on the extended example TestEm11

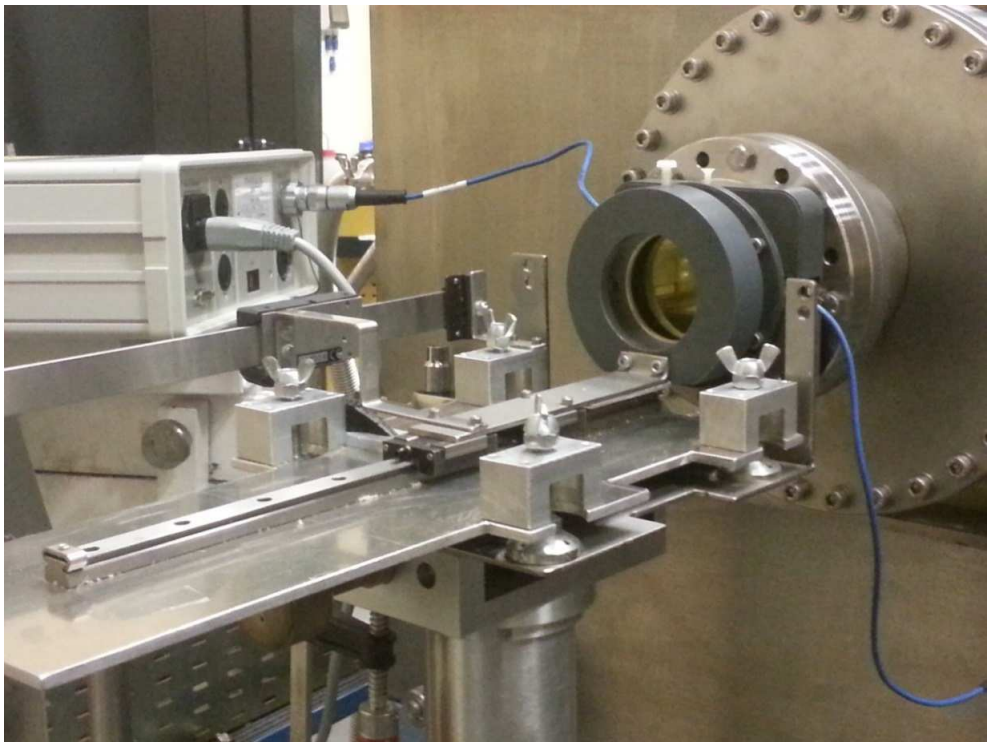

FIGURE 4.14: Precision linear driver

which belongs to the G4 version 10.1.2. TestEm11 computes the depth dose profile along the trajectory of the incident particle in the experimental room, which is considered as a rectangular box. The beam is defined in terms of particle type, energy and straggling in the PrimaryGeneratorAction class. The particles are shut at the left face of the geometry in the kinematics file. Energy and straggling can be changed through command lines in the ParticleGun class. Proton beam with a mean energy of 3.77 MeV (at the same position where samples are usually placed for the irradiation), which value was previously measured with a 500 μm thick ion implanted detector, and a straggling of 0.0321 MeV was set. The beam is described as a cylinder of 2 cm of diameter (to simulate the collimator used in the experiment) starting at the left of the physical space. Afterwards, we defined the geometry, which consists of a stack of one or several blocks of homogeneous material, called absorbers. The absorbers are represented as rectangular boxes filled with the corresponding material and thicknesses, and are placed perpendicularly respect to the beam orientation.

In this study, the dose depth profile was computed into the second IC to reproduce the experimental Bragg curve. The elements crossed by the beam from left to right are represented in fig.4.15.

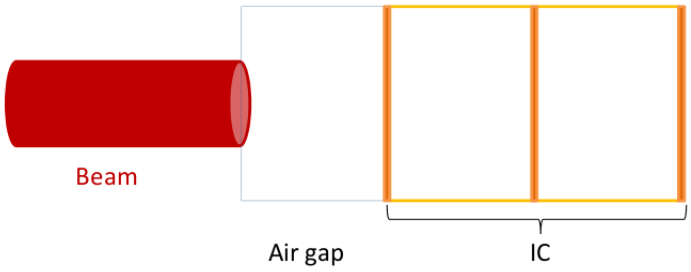

FIGURE 4.15: Scheme of the setup used for the Geant 4 simulation

The IC was defined as three electrodes made of Kapton (G4 KAPTON density 1.42 g/cm^3 and 7.5 μm thick) creating two air gaps (G4 AIR density 0.00120479 g/cm^3 and 6.75 mm thick), and the transversal dimension of the chamber was set at 44 mm. The air gap was varied at each simulation, in order to see how the Bragg peak is moving towards the elements. The PhysicsList is local in this case, which means that the standard electromagnetic physics (emstandard opt4) was already set in the example. The energy deposited is randomly distributed along the step. The step size is automatically given by the binning of the histogram. In this case the dose depth profile was computed with a step of 7.5 μm. Results are presented and discussed in the subsection 4.3.2.3.

4.3 Thesis core: Results

This section starts presenting the results obtained for the beam characterization in terms of homogeneity of the beam profile, energy and fluence (connected to the estimation of the dose onto the sample). As mentioned in Chapter 1 (see the subsection "Aim of this thesis work"), these studies are important in order to provide the best conditions for cell sample irradiations, in fact:

- the beam profile homogeneity assures a uniform dose distribution over the whole sample surface;
- the measurement of the energy onto the sample is important to identify the region of the Bragg curve used in the irradiation;
- particle fluence is used to quantify the amount of dose given to the sample.

The section continues with the results for the validation of the film calibration performed with the IC are shown. Then the behavior of the radiochromic films irradiated by protons and their response in absorbed dose will be presented. These data will be compared with Monte Carlo simulations using both SRIM2008 and LISE++ codes. Moreover, a Geant 4 application (described in subsection 4.2.4.1) has been implemented in order to simulate the experimental setup and to compute the dose inside the active layer of the films for each thickness of the absorbers. The section ends with the application to cancer cell cultures irradiated with the setup described above, presenting and discussing the results on the DNA damage caused by the low energy protons and comparing them to the damages caused by photon fields.

4.3.1 Characterization of the proton field: homogeneity and energy

For preparing irradiations of biological samples it is important to achieve a homogeneous and uniform dose distribution in an area equal to the sample surface. The first step of the analysis consists in checking the uniformity for different values of dose. Several tests were performed with gold targets of different thicknesses in order to choose the best compromise between energy loss and homogeneity onto the samples. The raw profiles of the beam for two gold targets used as scatterers, with thicknesses of 2.0 mg/cm^2 and 5.4 mg/cm^2 were studied. The energy loss for protons of 5.233 MeV in a gold target of 2.0 mg/^{2} is 0.055 $\pm$ 0.001 MeV, while for a thickness of 5.4 mg/cm^2 it is 0.149 $\pm$ 0.001 MeV. Such energy losses are acceptable, so in order to choose which scatterer is the most suitable, one should look at the beam profile onto the sample. The Au scattering foil of 5.4 mg/cm^2, leads to a beam profile with relative deviations from homogeneity within 5% while the other gives relative deviations from homogeneity within 15-20 % which is not acceptable measurements (fig. 4.16).

As a checking of the beam energy impinging onto the samples, measurements with the silicon detector were performed at the same position of the samples. Fig. 4.17 shows the energy spectrum (calibrated, as previously said, with a triple alpha source ^{239}Pu-^{241}Am-^{244}Cm) of the beam in this position, aligned with the center of the vacuum exit window. The black curve represents the experimental data while

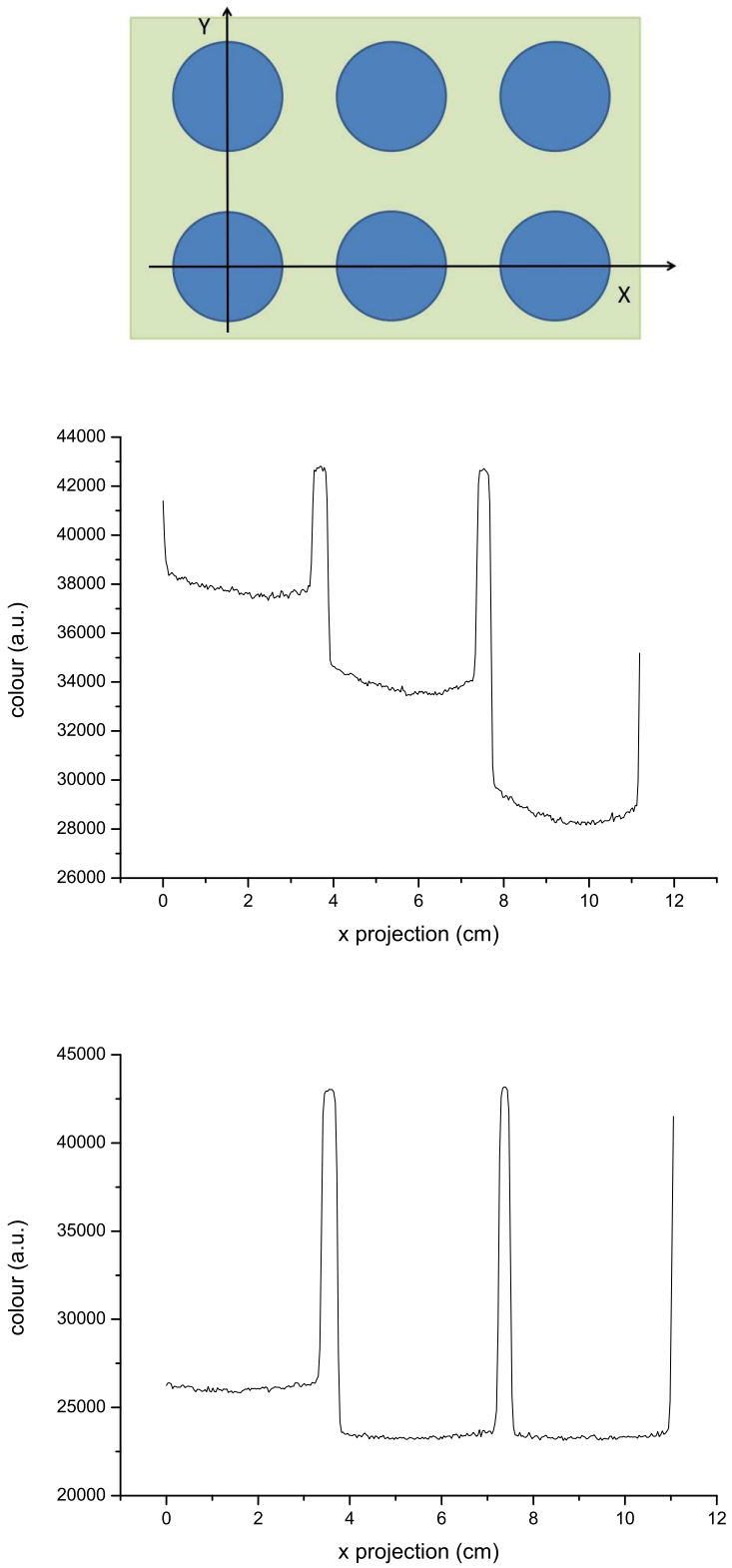

FIGURE 4.16: Top image: scheme of the profile projections of the film along X and Y directions; central image: raw beam profiles obtained for 2.0 Au mg/cm^2 target and dose values of 0.5, 1.0, 2.0 Gy; bottom image: raw beam profiles obtained for 5.4 Au mg/cm^2 target and dose values of 2.0, 3.0, 3.0 Gy

the red one is the fit to Gaussian distribution, which gave as result an energy of 3.83 ± 0.05 MeV.

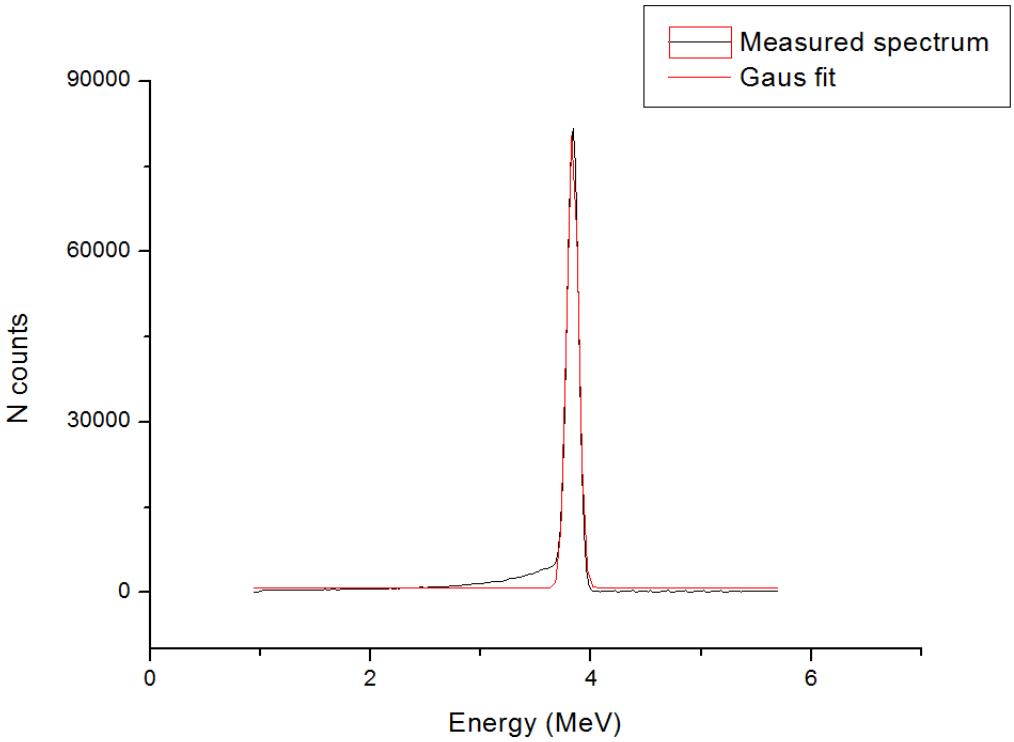

FIGURE 4.17: Energy spectrum measured by the silicon detector at the same position of the radiochromic films.

Another effect that must be taken into account is the bending of the Kapton window due to the pressure difference between its two sides. At very low energies, moving towards the Bragg peak, this could affect the performances of the irradiations, due to variations in the path traveled across the Kapton by protons crossing it at different points.

In order to establish if this is important in our measurements, studies of the energy at different transversal beam positions of the window were performed with the detector. Using the device shown in fig 4.18, five positions were measured, respectively, at the center and at the up, down, left and right borders of the proton beam.

As the results given in table 4.3 reflect, the variation of the energy at the borders is negligible since it lies within the standard deviation in all the positions.

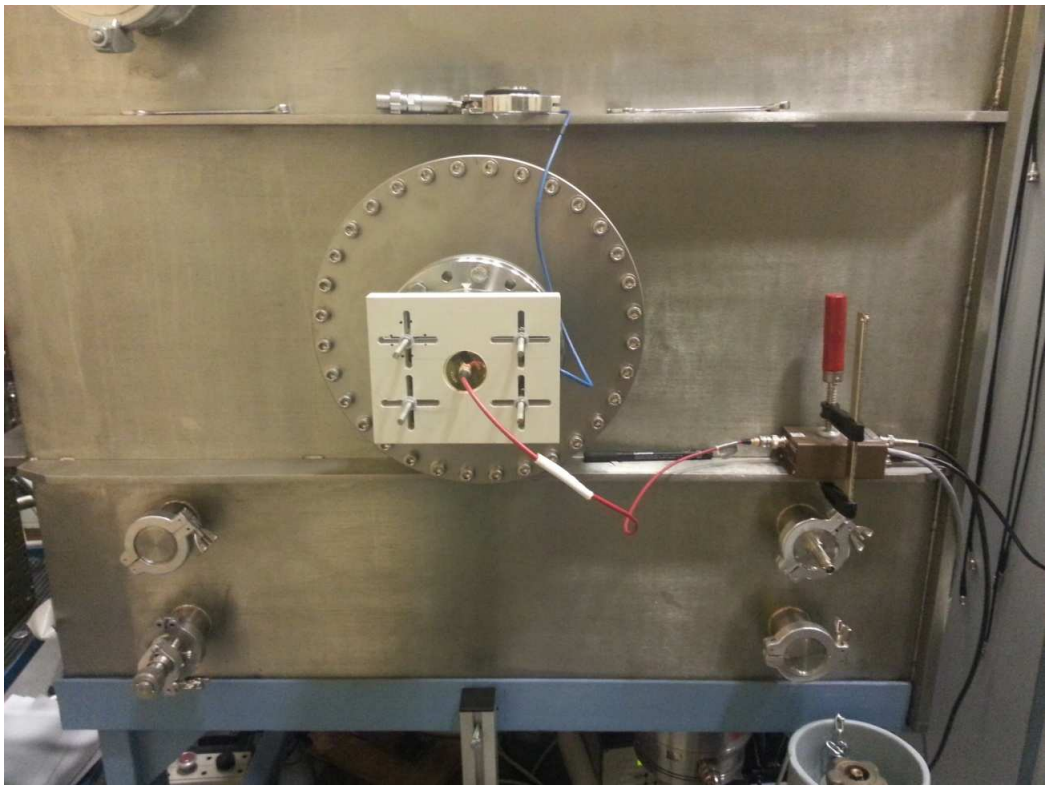

FIGURE 4.18: Holder for the silicon detector to measure the energy in different points of the exit window.

Energy measured (MeV)	Position of the detector
3.83 ± 0.05	Centre
3.80 ± 0.05	Up
3.81± 0.05	Down
3.81 ± 0.06	Left
3.81 ± 0.05	Right

TABLE 4.3: Energy measurements at five positions in the Kapton window.

Besides, the measurements with the silicon detector were performed in order to compare the energy measured at the sample position, with the one computed with LISE++ and SRIM2008 codes.

Moreover, this method can be used also to verify the thickness of the mylar foils used to degrade the beam energy. As it is summarized in table 4.4, the data given by the detector and the simulations are well comparable within the standard deviation.

Mylar thicknesses (μm)	Energy measured, silicon detector (MeV)	Energy calculated by LISE++
0	3.83 ± 0.05	3.83 ± 0.01
13	3.68 ± 0.05	3.63 ± 0.01
19	3.60 ±0.06	3.55 ± 0.01
26	3.52 ±0.06	3.46 ± 0.01
32	3.44 ±0.06	3.38 ± 0.01
38	3.36 ±0.06	3.29 ± 0.02
39	3.35 ±0.06	3.28 ± 0.02
45	3.27 ±0.06	3.19 ± 0.02
51	3.18 ±0.06	3.10 ± 0.02

TABLE 4.4: Energy measured by the silicon detector at the same position of the film with different mylar foils.

The characterization of the proton beam in terms of beam fluence is connected to the dose measurements and will be described in the following section.

4.3.2 Dose response of EBT3 GafChromic films to low-energy protons

One of the most important goals of this work was to perform dosimetry studies in the region of the Bragg peak, since it is a region of great interest in radiobiology studies and the dose quantification is not trivial because of the high gradient of energy loss. Here we will present and discuss the results obtained employing the EBT3 films for absolute dosimetry along the Bragg curve.

This study was performed in the following parts:

- Dose response at the plateau region of the Bragg curve, without beam energy degradation.
- Dose response at maximum and distal fall-off of the Bragg curve, degrading the proton energy with mylar foils.
- In addition, a further study, degrading the proton energy in air, was carried out to have a direct measurement of the Bragg peak.

In order to check the position of the Bragg peak inside the transversal section of the film, when the beam energy is degraded using mylar foils, SRIM2008 simulations

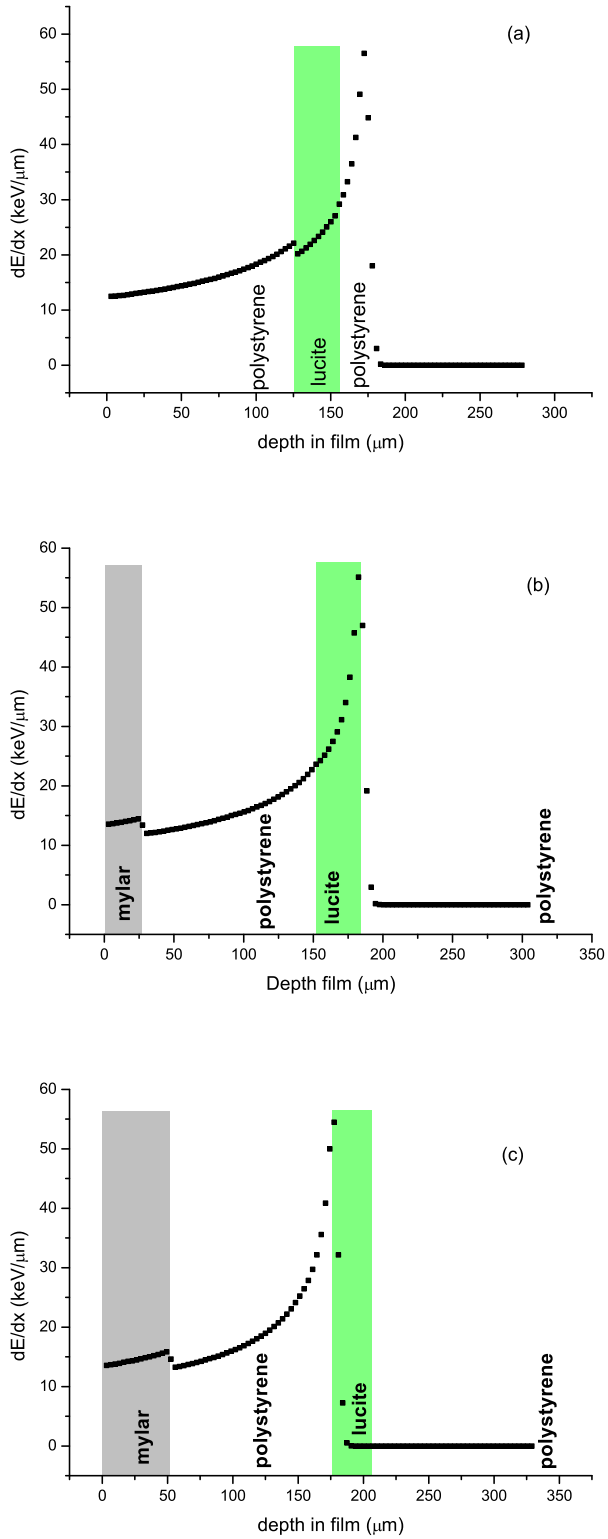

FIGURE 4.19: Bragg curve inside the transversal section of the EBT3 film for beam energy degradation with a) 0 μm, b) 26 μm and c) 51 μm of mylar, placed between the IC and the first polyester substrate of the film.

were performed. Fig. 4.19 shows the three main situations: (a) plateau region, (b) maximum and (c) distal fall-off.

4.3.2.1 Beam energy without degradation

First of all, we started studying the response of the films in the case of no beam energy degradation, represented in fig. 4.19 (a).

To calculate the dose onto the films, we used the data for the IC in the following way:

The number of protons going through the IC (N_p) is calculated by the formula:

$$Q = N_p \frac{\Delta E}{W} \tag{4.5}$$

where Q is the integrated charge measured with the IC, ΔE is the proton energy loss inside the two air gaps of the IC and W is the ionization energy needed to create an ion-electron pair in air, for which W = 34 eV.

The dose in the film is then obtained as:

$$D = F \frac{dE}{dx} \frac{1}{\rho} \tag{4.6}$$

where F is the fluence of the protons through the IC, dE/dx represents the stopping power of the protons in the active layer of the film and ρ is the density of the EBT3 active layer.

All the measurements were performed under the conditions of a nominal energy given by the accelerator fixed at 5.233 ± 0.001 MeV and low values of beam current of the order of 10 nA before passing the Au-scatterer.

The energy loss of the beam through the beamline elements was estimated using two codes: SRIM2008 and LISE++ [54] (see table A.1 in Appendix A).

In order to establish if the film calibration described in section 4.2.3.1 can be used to calibrate the films irradiated with protons, the curves of netOD of the EBT3 film's response, provided in the three color channels, are compared to that of photons. Fig. 4.20 shows such comparison, representing the optical density of

EBT3 Gafchromic films as function of the dose received for the three color channels red, green and blue (RGB) for protons (full dots) and photons (solid lines).

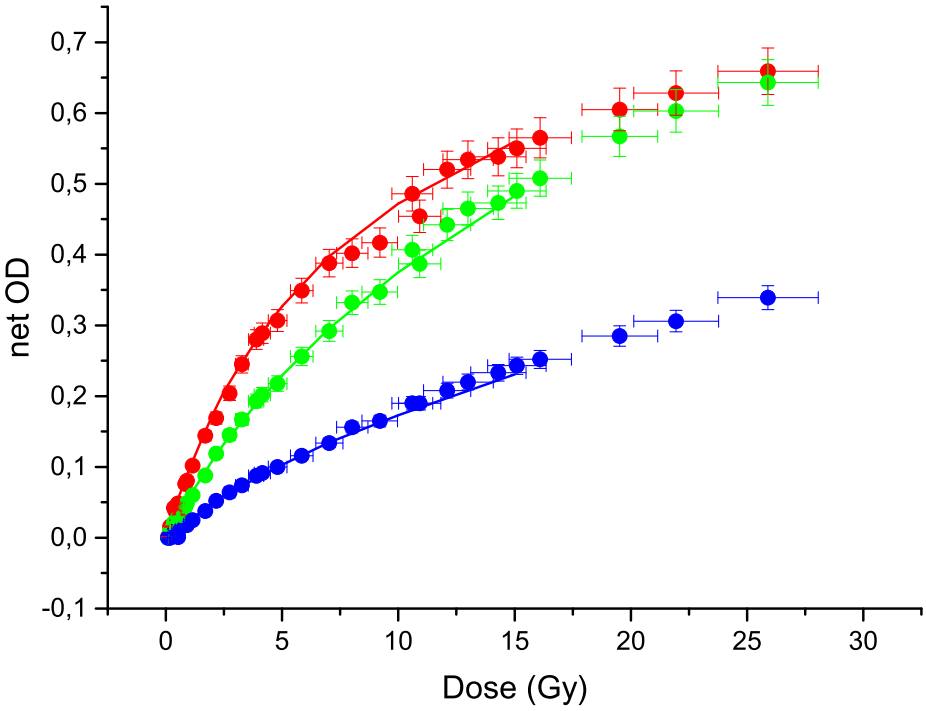

FIGURE 4.20: netOD of the EBT3 film for a dose range of 0-30 Gy. Dots represent the netOD in function of the dose for films irradiated with protons, the solid lines are for the films irradiated with photons. All these irradiations were performed outside the Bragg peak region studying the response for the three color channels RGB.

The uncertainties associated to the net OD are calculated as the standard deviation from the average value of the intensity color value (I) at each dose. Then, the uncertainty of the netOD derives from the uncertainty propagation associated to I and I_o. The results show that the two calibrations are compatible, verifying that the dose deposition of photon fields and protons at the plateau region of the Bragg curve is very similar.

As recommended in [55], in order to have a precise calibration in dose of the EBT3 films, one should look at the netOD curve and its first derivative with respect to dose. The experimental data of the netOD in a dose range (0 - 20) Gy were collected and analyzed (considering the averaged value of LET in the active layer of 23.32 keV/μm). They were well fitted by second order polynomial functions.

It is thus possible to calculate the first derivative of the netOD and study the sensitivity to the dose for the three color channels.

Top of fig. 4.21 shows the curves of netOD for protons obtained with the polynomial fit. At the bottom, we find the curves for the first derivative. Looking at these bottom plots, for a dose lower than 10 Gy, the red channel offers a better sensitivity compared to the green and the blue one, since the value of its derivative in this dose range is higher than the green and blue ones. For doses above 10 Gy, the green curve exceeds the red one, indicating that it could be preferable to use the green channel at higher doses. The blue one has a lower response gradient for the whole dose range considered therefore it is not recommended for dose value calibration.

It is important to note that, a considerable decrease in the sensitivity of the film response for doses above 10 Gy can be observed: in fact, the first derivative values decrease by a factor of two in a dose range of 0-10 Gy, suggesting that the best performances of such films must lie for small dose values.

A similar investigation was done by S. Reinhardt et al. [56]. The EBT3 films were irradiated using 6 MV photon beams and 20 MeV protons. The optical density in the red color channel was studied as function of dose and fitted using a polynomial equation. Such formula, provided in [56], was used to fit our data. The results of this study are shown in fig. 4.22. The solid black line represents the fit using the model proposed in [56] for photons and the dashed black one for the 20 MeV protons. We can notice that their model suits very well our experimental data (represented in red) within the measurement uncertainties.

After having demonstrated that the calibration done with photons can be used for films irradiated with protons (when the Bragg peak is placed at the second polyester substrate, top of the fig. 4.19), we calculate the dose using by formula 4.6 (D_{FL}) and the dose values given by the calibration (D_{EBT3}), (fig. 4.23). The ratio D_{EBT3}/D_{FL}) keeps within the range 1.0 - 1.1.

This can be explained considering that the energy distribution along the path in the matter for photons is similar to the one of protons at the plateau of the Bragg curve.

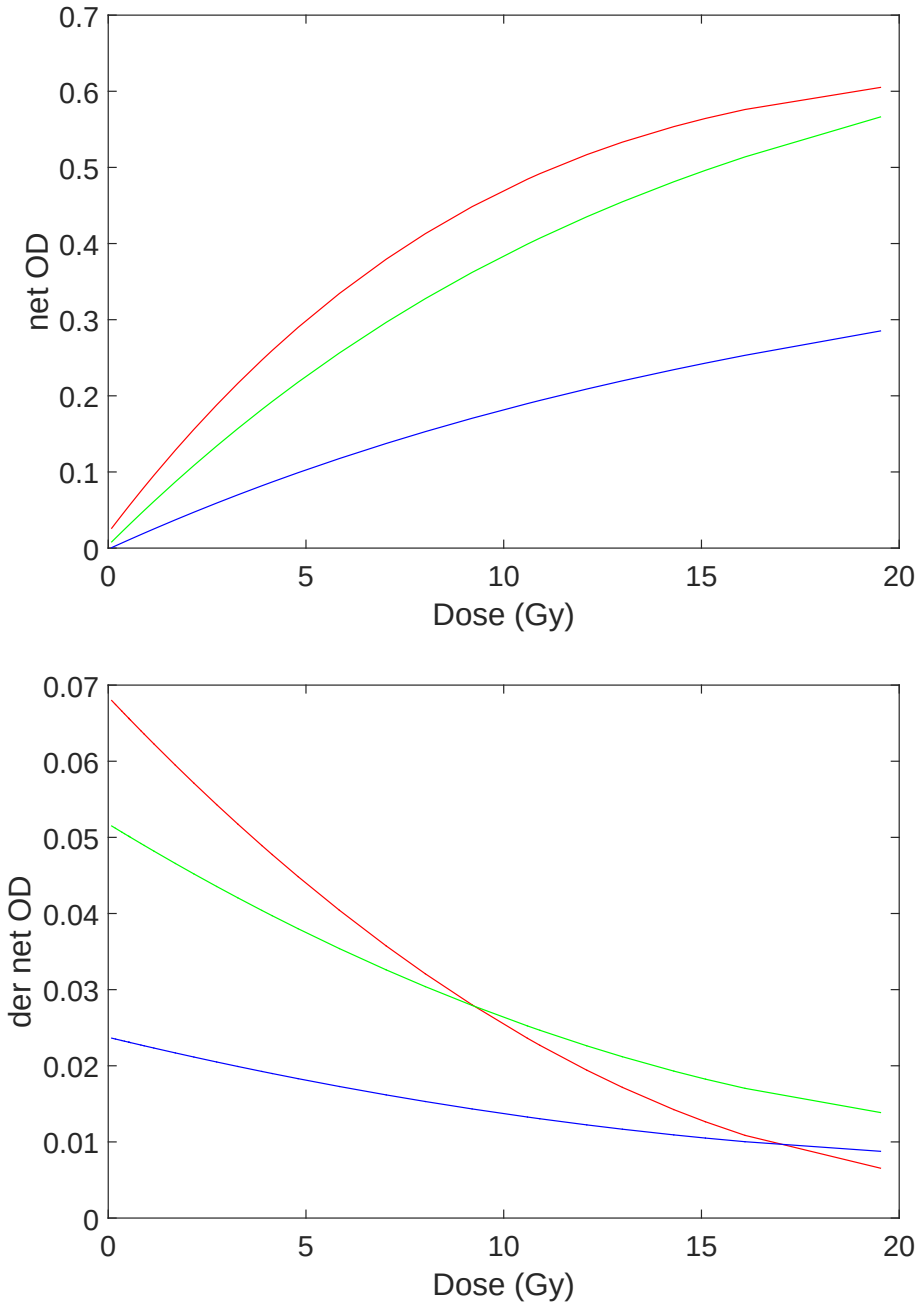

FIGURE 4.21: Top: netOD of the film for a dose range of 0-20 Gy. All these irradiations were performed outside the Bragg peak region studying the response for the three color channels RGB. Bottom: first derivative of the optical density with respect to dose, for the same dose range.

Once having established that in this case, the photon calibration curve can be applied when the films are irradiated with protons, we can directly obtain the calibrated dose profile, as shown in fig. 4.24 for three different dose values.

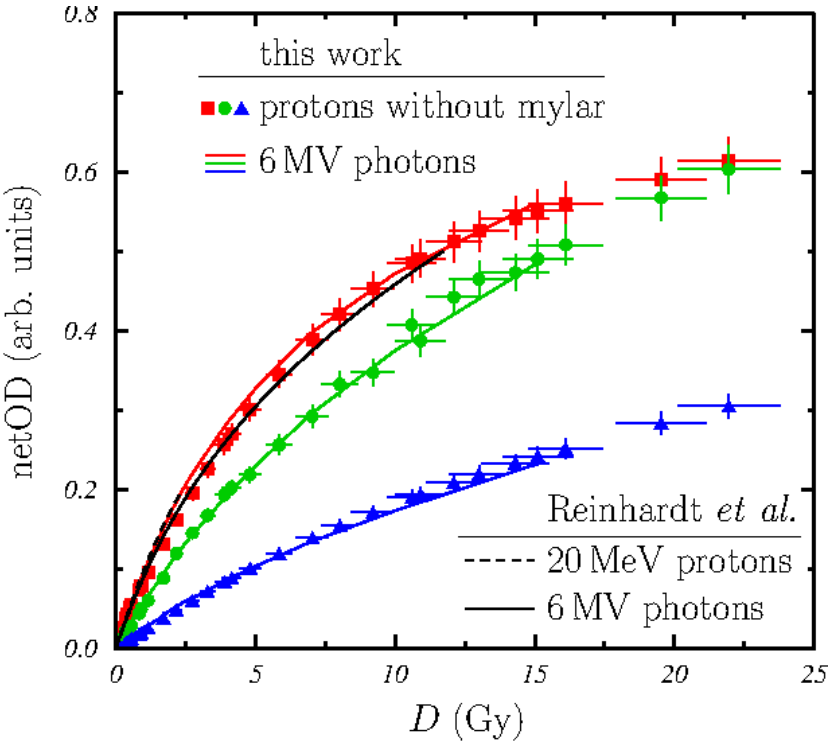

FIGURE 4.22: Comparison between the netOD curves presented in this work and with the study of S. Reinhardt et al. [56]

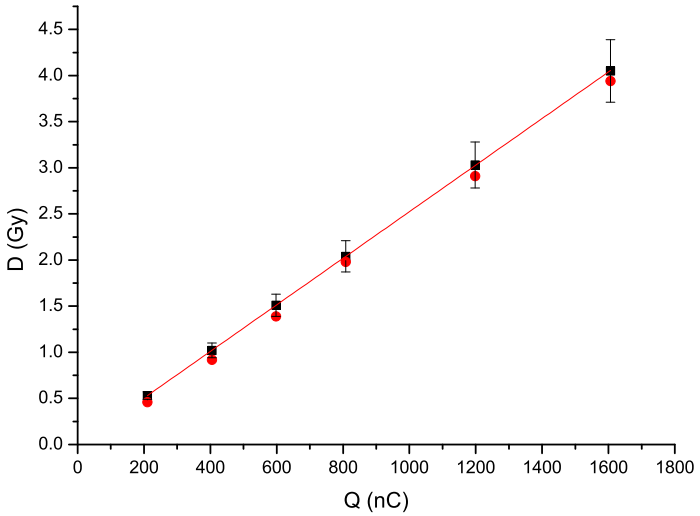

FIGURE 4.23: Comparison of dose values obtained from EBT3 films (using the standard photon calibration, red circles) and calculated doses (D_{FL}), at the position of the active film zone, using proton fluences obtained from charge measurements with a parallel-plate IC in front of the film (black squares).

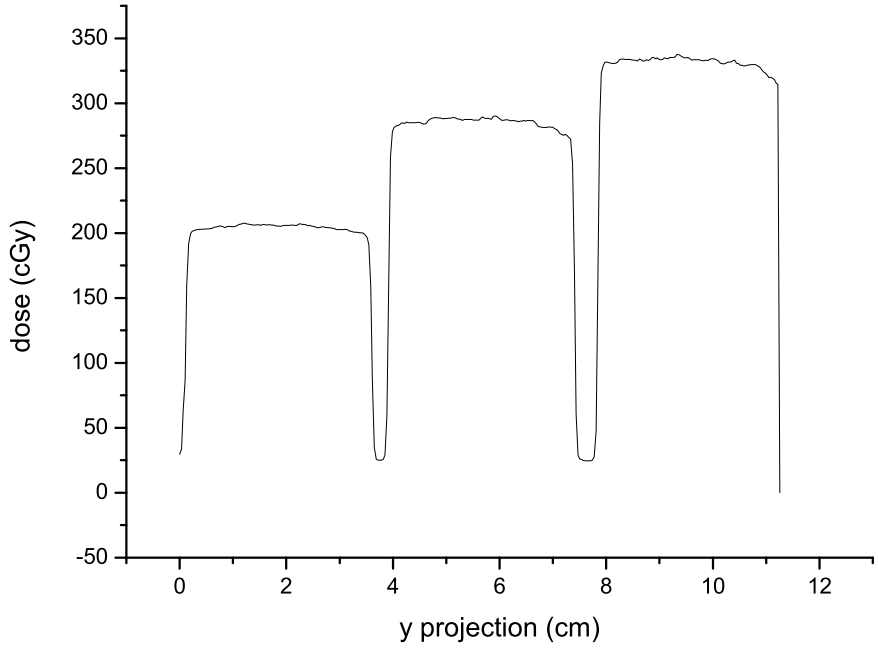

FIGURE 4.24: Calibrated dose profile for three irradiations.

4.3.2.2 Beam energy degradation with mylar foils

In order to move the Bragg peak inside the active layer of the film, the beam energy has to be decreased.

To do that, two main paths can be followed: i) one could change the terminal voltage of the accelerator or ii) it is possible to degrade the energy with passive absorbers of different thicknesses. Fig. 4.25 shows the beam profile for three values of dose, obtained by changing the accelerator terminal voltage. As can be seen, the profile obtained has deviations from homogeneity of 13 %, which is a value not acceptable for our measurements. Changing accelerator parameters affects the beam optics, so this method is more complicated to employ and there is no guarantee that we can reproduce similar beam profiles for the different energies. On the other hand, degrading with absorbers the beam energy, the homogeneity of the beam profile is maintained for the whole set of data; an example is shown in fig. 4.26. By means of this technique, the energy of the beam was degraded passively. This allowed to maintain the same accelerator and beam conditions for the whole series of measurements.

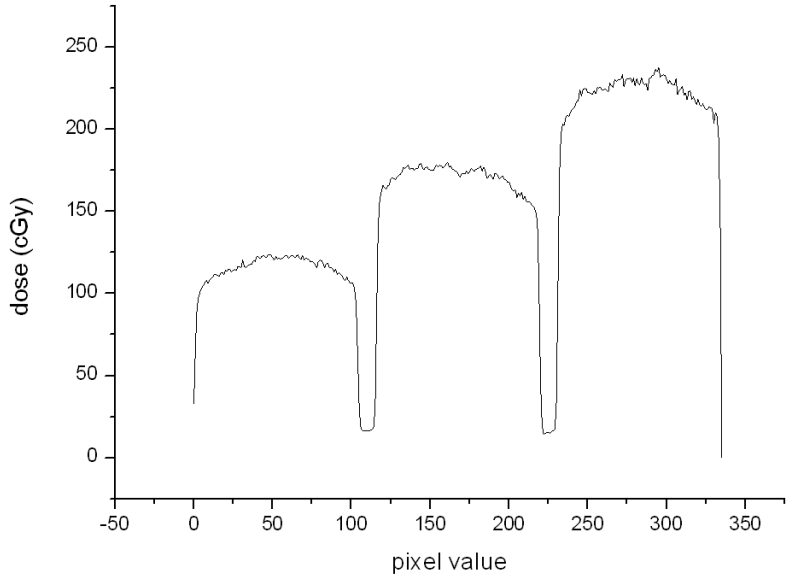

FIGURE 4.25: Dose profile for a beam energy degraded changing the voltage of the accelerator terminal.

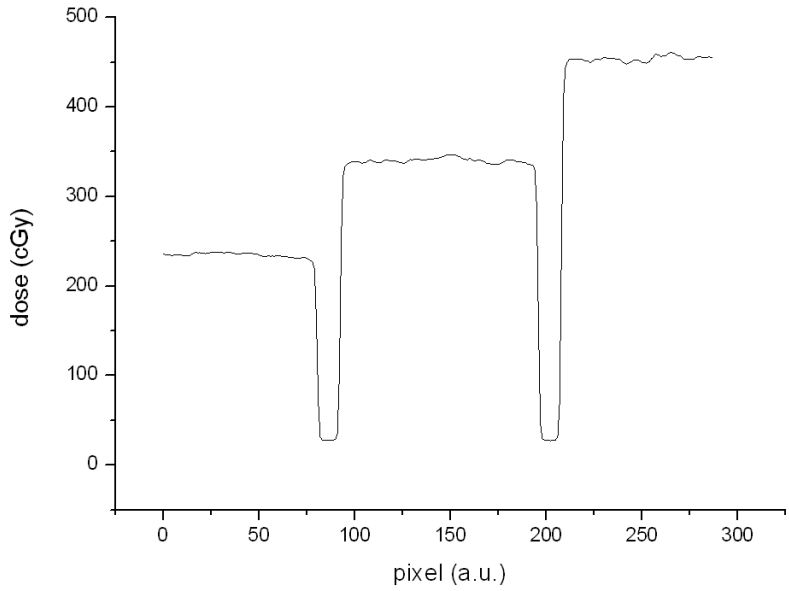

FIGURE 4.26: Dose profile for a beam energy degraded passively.

When the Bragg peak falls inside the active layer (central panel of Fig. 4.19), effects of saturation are noticed. The darkening of the radiochromic films depends on the organic monomers, which polymerize under ionizing irradiation. When the Bragg peak is located inside the active layer, the LET and the associated stopping power increase abruptly, the energy of the protons is deposited in a small volume [57] and such effect leads to a darkening of the film that is not anymore

proportional to the absorbed dose. Moreover, previous studies showed that the film response is dependent on the proton energy near the Bragg peak and the distal fall-off region [58], [56], [59].

Fig. 4.27 and table 4.5 present the results obtained for eight irradiations where the initial energy of the protons delivered by the Tandem accelerator was degraded using mylar foils of 6 and 13 μm (20% of thickness tolerance, data reported in the manufacture guide) in different combinations. In order to investigate the effect of saturation occurring in the EBT3 film when the Bragg peak approaches or falls inside the active area, Monte Carlo simulations (with SRIM2008 code) were performed to study how the dose in the film changes by interposing sets of 2 μm thick mylar foils in a range of 2-50 μm (fig. 4.27, black curve) and then compared to the experimental data of the film dose. The results show that the dose calculated by equation 4.6 (where the $\mathrm{d}E/\mathrm{d}x$ was computed with SRIM), deviates from the standard calibrated one, as soon as the Bragg peak approaches the active layer.

We define the mylar thickness interval which placed the Bragg peak in the active layer as "Bragg peak region" (26-51 μm of mylar, Fig. 4.19 (b) and (c)).

Mylar thickness (μm)	$D_{\mathrm{EBT3}}/D_{\mathrm{FL}}$
0	1.03 ± 0.09
13	0.93 ± 0.08
19	0.82 ± 0.07
26	0.81 ± 0.07
32	0.71 ± 0.06
38	0.69 ± 0.06
45	0.71 ± 0.06
51	0.81 ± 0.07

TABLE 4.5: Comparison between the dose calculated on the basis of proton fluences measured with the IC (D_{FL}) and the dose obtained from the film calibration with photons (D_{EBT3}), increasing the mylar thickness.

According to our measurements, the saturation effect starts for a mylar thickness of 19 μm.

In fact, the values reduce noticeably when the mylar thickness ranges from few microns below the lowest limit of the Bragg peak region up to its upper limit, varying from 0.69 ± 0.06 to 0.82 ± 0.07. Looking at these results, we can make some important considerations: when the Bragg peak lies well outside of the active layer the film calibration can be used because the ratio $D_{\mathrm{EBT3}}/D_{\mathrm{FL}}$ is compatible

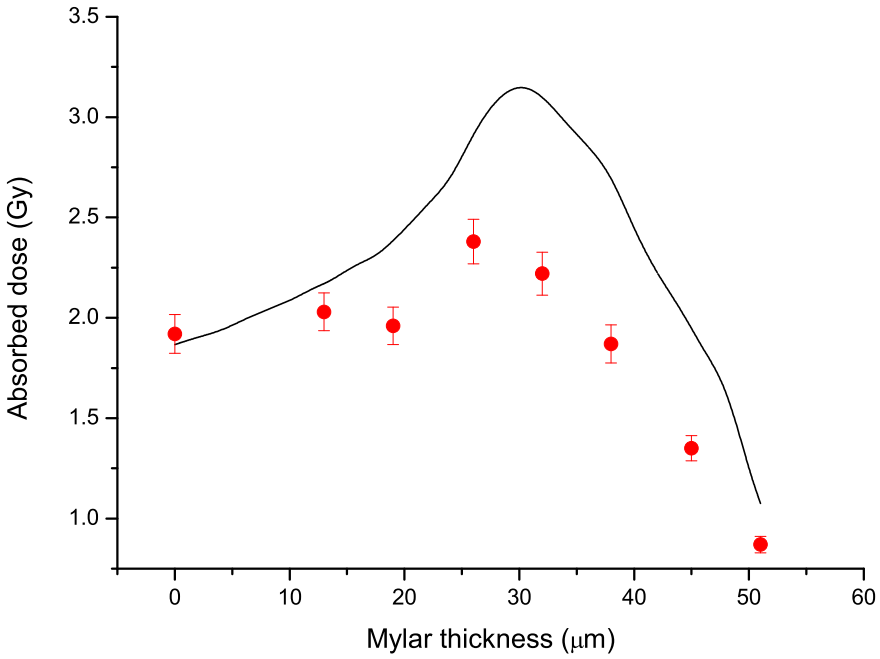

FIGURE 4.27: Absorbed dose at different mylar thickness. Black curve indicate SRIM2008 simulations, while the red dots represent the experimental data of the calibrated dose for the EBT3. Around the maximum value that corresponds to a mylar thickness of 32 μm, the film response is lower than expected due to the quenching effect.

with 1. By increasing the thickness of the mylar foils, the Bragg peak is moved towards the active zone. A quenching effect can be noticed (between 19 and 51 μm of mylar in our measurements) with a marked effect when its maximum lies in the active zone (32 - 45 μm of mylar). Finally, in the situation shown in fig. 4.19 (c), where the Bragg peak is just exiting the active area, the saturation effects are less evident due to the sharp decrease of the deposited dose. Other causes of uncertainties in the quantification of the quenching effect can be attributed to the stopping power libraries used by SRIM2008, which show uncertainties of the order of 10 % at energies in the proximity of the Bragg peak [60], [61]. This source of uncertainty is also well-known in other general purpose Monte Carlo codes such as PENH [62] and Geant 4 [53].

As a consequence of the above mentioned quenching effect, the standard EBT3 film calibration is not valid in the Bragg peak region, and another method of calibration has to be adopted in such case.

This subsection is concluded with a comparison, shown in fig. 4.28, of the calibration curve of optical density as function of the dose without beam degradation (continuous line), taken as reference, with the netOD obtained for beam energy degradation using respectively 32 μm (triangles) and 51 μm (circles), regions of maximum and distal fall off of the Bragg curve, to investigate the effect of higher LETs onto the films.

The measurements were performed in a dose range 0 - 20 Gy and analyzed separating the red, green and color channels (respectively top, central and bottom panel).

The plots show that, as the LET increases, the netOD is lower than expected, with a more evident effect for increasing dose values.

A possible explanation for the decrease of netOD (and thus of the ratio D_{EBT3}/D_{FL}) when the Bragg peak is overlapping the active layer of the film is that a local saturation of the polymerization is occurring:

Explaining in terms of LET, the number of radiation-induced activated polymerization sites increases with LET until eventually no more sites are available for activation and the polymerization stops locally. Thus, since there are no sites available for activation, when the dose increases, no sites will be activated, leading to a greater difference between the D_{EBT3} values at maximum and distal fall off and the correspondent D_{FL} values.

Quenching values are summarized in table 4.7.

Table 4.7 gives an estimation of the quenching factor represented by the ratio $Dose_{EBT3}/Dose_{FL}$, distinguishing between irradiation at low doses (< 5 Gy) and high doses (> 10 Gy). In the region of the maximum (32 μm of mylar), the quenching factor is passing from a value of 0.62 ± 0.06 for a dose around 4 Gy to 0.39 ± 0.03 for a dose range of 16-19 Gy.

At the distal fall off (51 μm of mylar), the trend is similar to the previous case: the quenching factor is passing from a value of 0.89 ± 0.08 at low doses to 0.47 ± 0.04 at high doses.

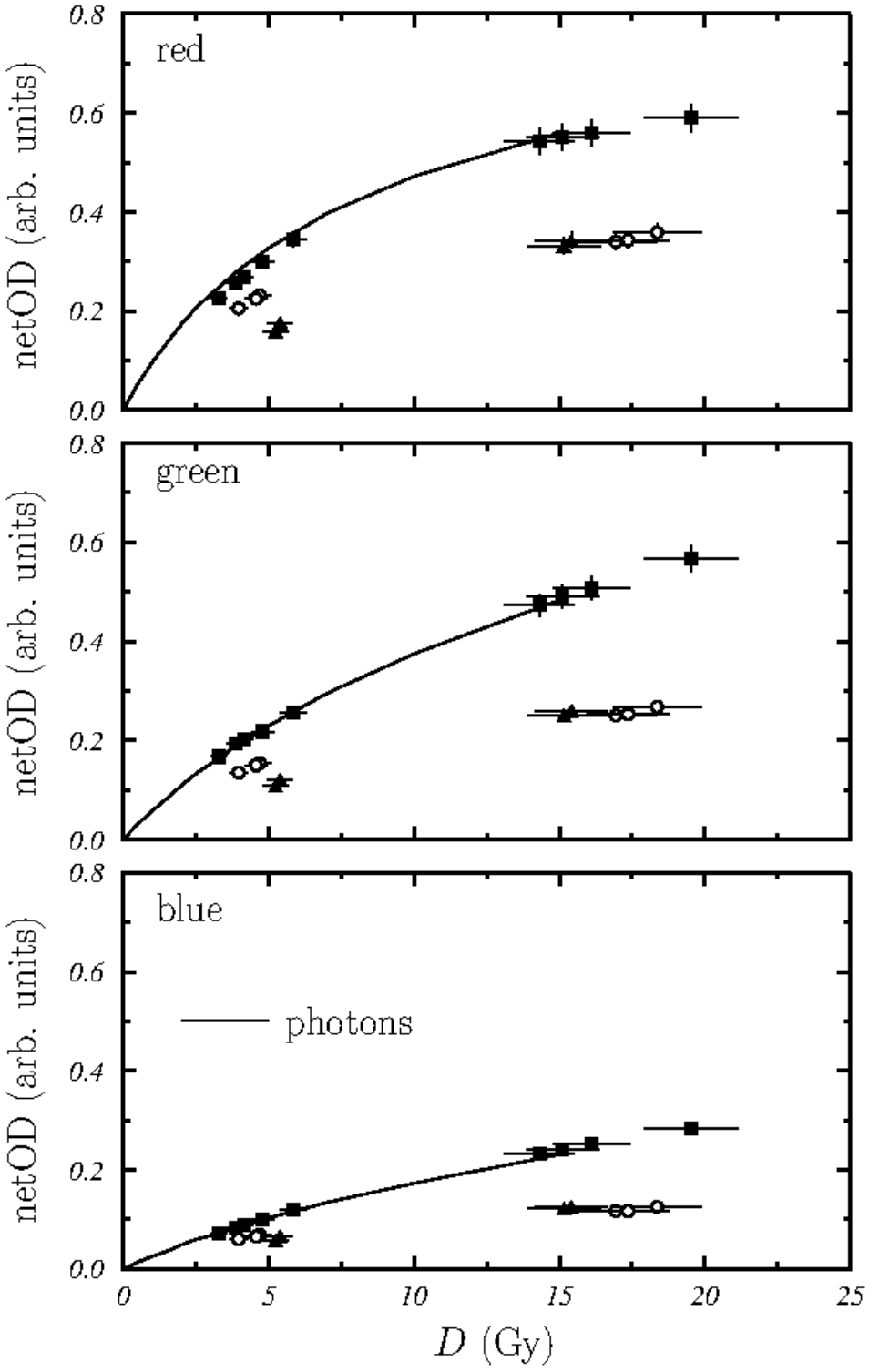

FIGURE 4.28: Calibration curve of optical density as function of the dose without beam degradation (continuous line) and the experimental data for beam energy degradation using 32 μm (triangles) and 51 μm (circles) of mylar. From top to bottom, the plots show the study for each of color channels RGB.

TABLE 4.6: Quenching values

Mylar thickness (μm)	$Dose_{EBT3}$/ $Dose_{FL}$, low doses (< 5 Gy)	$Dose_{EBT3}$/ $Dose_{FL}$ high doses (> 10 Gy)
0	0.93 ± 0.08	1.00 ± 0.06
13	0.81 ± 0.07	0.77 ± 0.05
19	0.81 ± 0.07	0.77 ± 0.05
26	0.69 ± 0.06	0.48 ± 0.04
32	0.62 ± 0.06	0.39± 0.03
38	0.76 ± 0.06	0.33 ± 0.03
45	0.77 ± 0.06	0.53 ± 0.04
51	0.89 ± 0.08	0.47 ± 0.04

TABLE 4.7: Comparison between the dose obtained from the film calibration with photons and the dose calculated with formula 4.6, increasing the mylar thickness. The comparison is done at low doses (< 5 Gy) and high doses (> 10 Gy)

4.3.2.3 Beam degradation in air

One of the greatest challenges of this kind of measurements is to establish the position of the Bragg peak in the transversal section of the EBT3 film. This is not experimentally measurable because of the polystyrene substrate before the active layer of the film. Thus, we rely on Monte Carlo simulations to know this position.

In order to validate our simulation, we performed a direct measurement of the Bragg peak for low energies and then the results were compared to the Geant 4 simulation (see subsection 4.2.4.1). This was done by using the precision linear driver described in subsection 4.2.4 and two flat, parallel electrodes ICs working in air. The scope was to degrade passively the beam energy by interposing different "layers" of air and study the energy loss of protons as function of their incident energy on the second IC. The first IC is fixed at the Kapton window at the exit of the beam line, while the second IC is mounted in a moving support. The measurements were performed for a range of 0 - 20.2 cm of air with a step of 0.2 cm.

When the fast closing valve is opened, the protons go through the two ICs. Each measurement was stopped when an integrated charge value Q1 (for the first IC) of approximately 100 nC was reached and then, the integrated charge Q2 was also measured in the second IC. From the ratio Q2/Q1 one could reconstruct the Bragg curve, as shown in fig. 4.29 (black squares).

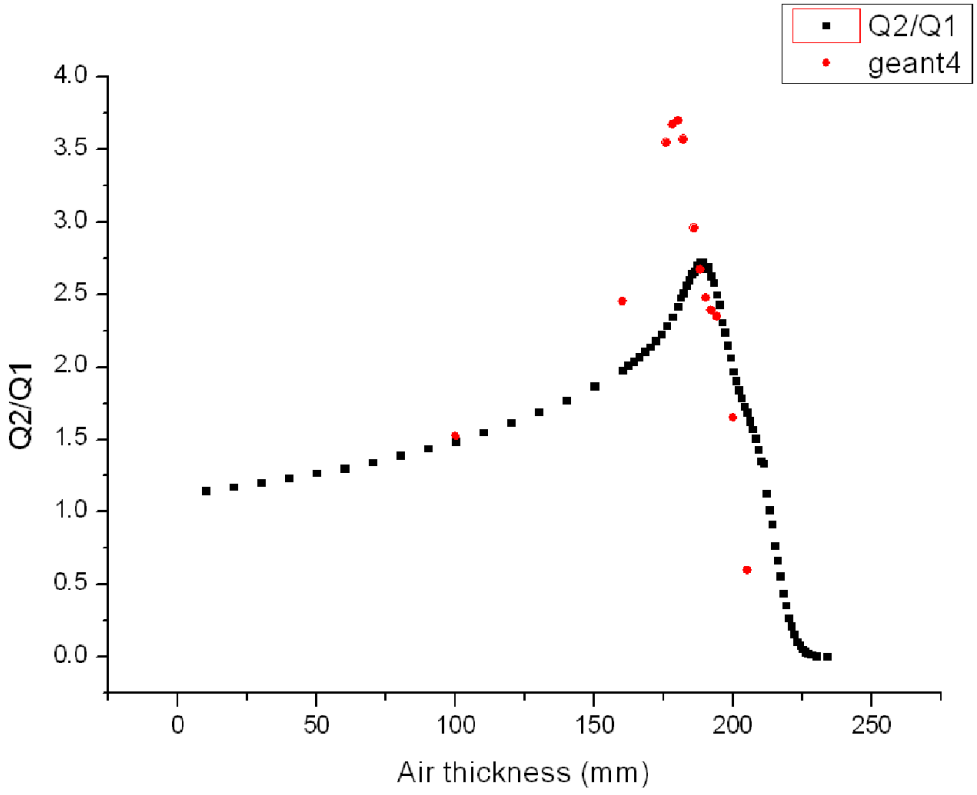

FIGURE 4.29: Comparison between the Geant4 simulations (red circles) and the measurements performed with the two ICs (black squares).

The data from simulations are represented as red circles. In principle, the width of the peak is primarily due to the range straggling, but it is also affected by the energy definition of the proton beam. The position of the maximum of the Bragg peak is located at 180 mm for the simulation and 189 mm for the measured data. The accordance between the simulations and the experimental data is about 5%, which is a very good agreement.

It should be noted that the IC is not infinitely thin and makes an integration of the pristine Bragg curve; this is why the curve appears with a FWHM greater than the simulated one. In addition, for air thicknesses of 20.2 cm and more, the proton beam is stopped in the first air gap of the second IC; this fact gives rise to the discontinuity of the curves around this value.

4.3.3 First radiobiological studies

Radiobiological studies are very important in order to investigate the effects of the radiations in the living cells. When an ionizing radiation impacts a living organism, a damage in the DNA may occur. As a response to this damage, the cell suspends its cycle and tries to repair the damage. The result of this response admits three scenarios: the cell may repair error free, repair wrongly (causing mutations, which could lead to cancer) or die. The scope of treating cancers is to stop the malignant cells from dividing. However, the tumor is a complex structure in which not all the cells contribute in the same way to its growth. The compartment of proliferative cells, well oxygenated, is known as "fraction of the tumor growth". In this compartment, one must distinguish between clonogenic cells, which are responsible for the unlimited proliferation of cells, and neoplasic proliferant cells of limited life. Clonogenic cells are the ones to kill in order to control the tumor by means of radiations.

All the studies mentioned before (beam profile homogeneity, measurement of the energy incident onto the sample, particle fluence measurement and quantification of the absorbed dose) are essential in order to obtain the best conditions for cell culture irradiation. Once an homogeneous profile is obtained over the whole cell sample surface, the cells can be irradiated.

These cells were irradiated with proton energies in the plateau region of the Bragg curve, where the dose evaluation is well known [9], and where the RBE is established to be 1.1.

At very low doses (approximately 0.5 Gy), Marples and Joiner, reported in 1993 that, for the cellular line V79 of hamster fibroblasts, the value of the survival fraction of cells decreases respect to the one expected at these low doses. From this critical dose, the fraction of survival cells increases till 1 Gy. For bigger doses, the survival curve is well described by the quadratic model. This phenomenon is known as low dose hyper radiosensitivity (LDHRS). Many other studies on hypersensitivity to cell killing of samples exposed to X-rays and γ rays have been reported for doses below $\sim$ 0.5 Gy.

The biological interpretation is not completely clarified. There are several hypotheses to explain the biological mechanisms that cause this phenomenon; the most one attributes the hypersensitivity to a delay in the reparation mechanism

at very low doses. Thus, the cells die for apoptosis. Results suggest that a dose of 0.5 Gy or less is not sufficient to trigger an inducible repair mechanism [63], [64], [65].

Two are the principal motivations which drove our investigation of the cell response for low energy protons. At first, we wanted to study the effect of the protons onto the cells to understand how LET influences DNA damage; the results were then compared to those of photon irradiation. Secondly, we performed the measurements at low doses to investigate the low-dose hypersensitivity phenomenon.

4.3.3.1 Materials and Methods

The cell samples were prepared and supplied by collaborators of this research work from University of Granada.

Cell cultures: The cells used are from the MCF-7 breast cancer cell line. They were cultured in monolayer and placed in Petri dishes (fig. 4.30).

FIGURE 4.30: MCF-7 cells. Cells in the culture medium placed in Petri dishes, before behind irradiated.

For the cell culture experiments, around 200,000 cells were seeded on sterile coverslips (Hirschamann Laborgerate 22x22 mm, Germany) contained in tissue culture plates 6-wells flat botton cell (Sarstedt, Inc. Newton, USA) and Petri culture dishes (Becton Dickinson, 35 mm of diameter and 10 mm thick. N.J. USA). The culture medium used was DEMEM/High Glucose medium (GE Healthcare Life Sciences HyClone Laboratories, Utah, USA) integrated with 10% fetal bovine

serum. Cells were incubated at 37°C in 5% CO_2 pH=7 y 95% of humidity to guarantee the optimal growth of the cells. Each box contained only alternative cultures (fig. 4.31) which were irradiated with the same dose value to have a triplicated result for each measurement.

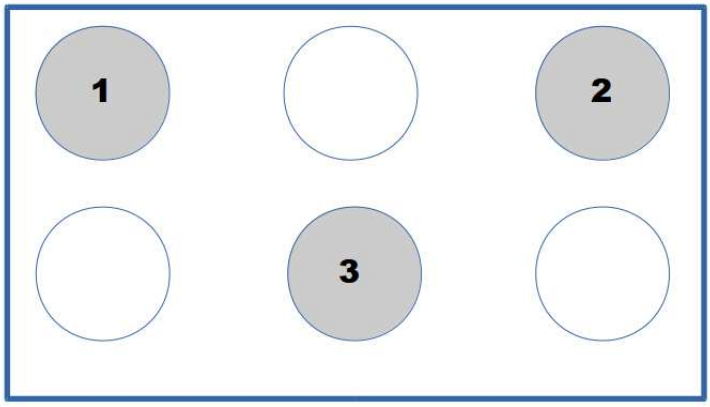

FIGURE 4.31: Cells in Petri dishes: irradiation order from number 1 to 3 for each series of measurements.

Proton irradiation:

The cells furnished by the University Hospital S. Cecilio Granada, Radiology Department, are brought to CNA in adequate conditions of temperature with the minimum stress possible to not alter the results.

The impinging energy onto the samples was of 3.585 MeV (measured with the ion implanted silicon detector at the same position in air of the cells). Just before the irradiation, the cells were stripped off medium for the proton assays; instead, in the case of photon assays, cells were irradiated with the medium. The holder for cell samples is placed in a vertical position at the end of the beam line. The selected sample was centered with the help of a laser and irradiated. The fast-closing valve was opened and closed manually, checking the values of integrated charge onto the electrometer. Subsequently, the charge value was transformed into absorbed dose value. For each value of dose, three samples were irradiated using the order shown in fig. 4.31. The dose values for proton irradiation, measured with the IC were: 0.25, 0.38, 0.52, 0.63, 0.78, 1.03, 1.28, 1.91, 2.57, 3.82, and 5.10 Gy. In table 4.8, details about each value of irradiation are reported.

Immediately after the irradiation, the cell damages are fixed following the protocol cited above and are placed in a box filled with ice.

Cell position	Expected dose (Gy)
1	0.25 ± 0.02
2	0.25± 0.02
3	0.26 ± 0.02
1	0.38 ± 0.03
2	0.37± 0.03
3	0.38 ± 0.03
1	0.51± 0.04
2	0.52± 0.04
3	0.52 ± 0.04
1	0.65± 0.05
2	0.65± 0.05
3	0.58 ± 0.05
1	0.79± 0.07
2	0.77± 0.06
3	0.77 ± 0.06
1	1.03± 0.09
2	1.02± 0.08
3	1.04 ± 0.09
1	1.28± 0.11
2	1.27± 0.11
3	1.28 ± 0.11
1	1.89± 0.16
2	1.93± 0.16
3	1.90 ± 0.16
1	2.56± 0.21
2	2.59± 0.22
3	2.55 ± 0.21
1	3.82± 0.32
2	3.81± 0.32
3	3.84 ± 0.32
1	5.10± 0.42
2	5.10± 0.42
3	5.09 ± 0.42

TABLE 4.8: Absorbed dose at the cell positions 1,2,3 for proton irradiations, estimated with the ionization chamber measurements (D_{IC})

Photon irradiation:

For the photon assays cells were irradiated with X-rays produced by the accelerator ARTISTE, Siemens, operating at 6 MV. The cells were irradiated with their medium and maintained in horizontal position respect to the beam direction.

The measurements were performed at the University Clinical Hospital in Granada, Spain. The culture boxes are situated inside a phantom built up with solid water RW3 (PTW, Freiburg, Germany), slabbed at a depth of 1.5 cm, with an additional 6 cm of the same material on top of it. The doses applied in this case were: 0.2, 0.3, 0.4, 0.5, 0.6, 0.8, 1, 1.5, 2, 3, and 4 Gy and analyzed a non-treated control cells.

The cells were fixed and moved for their analysis.

4.3.3.2 Sample analysis

The damage produced by the radiation on the DNA is evaluated counting the number of foci produced in the nucleus considering the average over the cells in a sample. The damage was fixed immediately after the irradiation. The number of foci was observed each ten minutes for the 24 hours that followed the irradiation.

Straight away, the samples were washed with ice-cold PBS pH 7.3 twice. Then cells were fixed and washed with ice-cold Fixation Buffer and Permeabilization Wash Buffer (BioLegend Inc, San Diego, USA) according to the recommendations described in the protocol.

After that cells were incubated with Cell Staining Buffer (BiolLegend Inc., San Diego, USA) for 30 min at room temperature. Purified Mouse anti-γH2AX (pS139) (BD PharmingenTM BD Biosciences, San Jose, USA) was added overnight in 100 μl of Staining Buffer (1:2000 dilution).

Samples were incubated overnight in the dark at 4ºC. Excess primary antibody was removed by washing with permeabilization Buffer three times for 5 min. Goat Anti-Mouse IgG H&L (HRP) ab97023 (abcam, Cambridge. UK) was added in 300 μl of Staining Buffer (1:3000 dilution) and incubated for 1h in the dark at room temperature. Excess secondary antibody was removed by washing with permeabilization Buffer twice for 5 min. Next, TO-PRO*-3 dye (invitrogen, California. USA) was added in 100 μl of PBS pH 7.3 (1:300 dilution) and cells were incubated

for 15-20 min in dark at room temperature. Finally, after removed the dye of stained, cells were washed with 1 ml of distilled water for 5-10 min in the dark at room temperature. The immunostaining images were visualized by a Leika SP2 confocal laser and a DC200 camera, with a 100x objective.

Around 30 nuclei were analyzed per each coverslip. The foci analysis was made studying the relative fluorescence intensity and was performed whit ImageJ software, adjusting brightness and contrast of the images acquired previously, fig. 4.32. To this scope, an Image macro (called PZFociEZ, implemented in [66]) was used to reduce the image background leaving only the fluorescence signal, which belongs only to single foci.

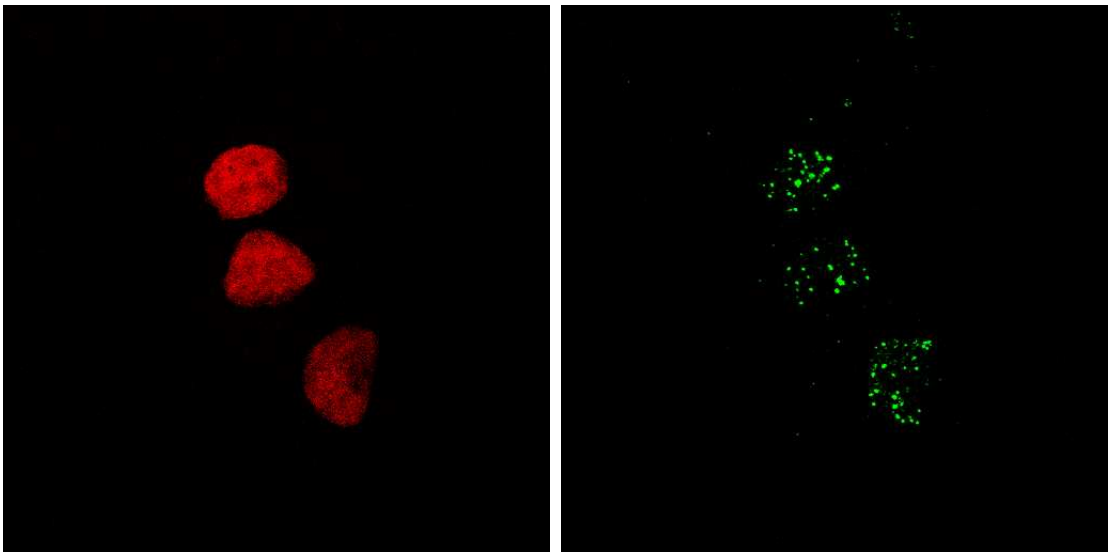

FIGURE 4.32: *Left*: Microscope image of DNA damages for a 3 Gy dose of protons.*Right*: Image of the DSB for 3 Gy of dose of protons.

Three independent measurements were performance and the results were presented as the mean ± SEM (Standard Error of the Mean).

4.3.3.3 Preliminary results

Here the preliminary results of the cancer cells performed at CNA are reported. Imping energy onto the samples was of 3.585 MeV (measured with the ion implanted silicon detector at the same position in air of the cells).

The same cell type were also exposed to photons delivered by a linac operating at 6 MV mode. Since dosimetry and radiation biological effects are well known for

exposure to photons and/or electrons, the radio biology studies performed with ions must be compared to photons for having referenced measurements.

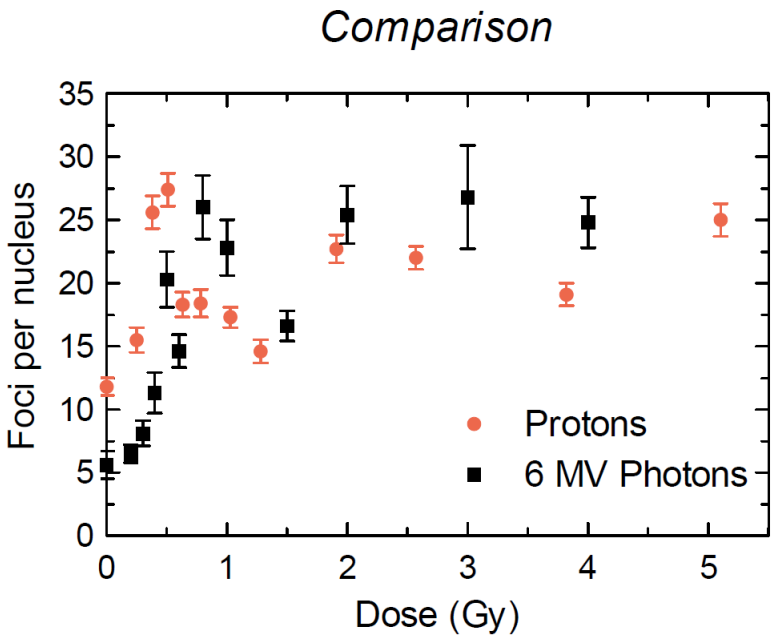

FIGURE 4.33: Comparison between the foci due to photon irradiation (black squares) and protons (orange circles). For doses $\leq$ 1 Gy evidences of hyper sensibility are noticed.

The observation of low dose hyper sensitivity requires knowledge of how the cell survival varies with the absorbed dose for doses below 0.5 Gy, and this requires that both the dose and the survival must be accurately determined, the methods employed must be carefully analyzed and the corresponding uncertainties must be calculated in detail.

Measurements with doses of 0.25-5.10 Gy have been done both with protons and with photons. In fig. 4.33, the comparison between these two sets of data is performed. However, for doses lower than 1 Gy, there is a sudden increase of the foci; this can be explained considering the cell hyper sensitivity to low doses (mentioned above). By increasing the dose, the repairing mechanism is triggered and the number of foci decreases, and the trend is well explained by the linear quadratic model (eq. 4.1).

This could have important clinical implications: since RBE is higher for protons than for photons, normal surrounding tissues could be heavily damaged in penumbra areas, so more attention has to be paid in a treatment plan.

On the other side, hypersensitivity has an important therapeutic application: since the cells have a delay in repairing for low doses, treatment plans provide dose-fractionation delivery, for enhancing the radiation killing power.

4.4 Final remarks

In this chapter, the preparations necessary for performing irradiatons of biological samples at the CNA Tandem accelerator were described. This includes the installation of various beam line elements in order to achieve homogeneous irradiation fields and to monitor the proton fluence by a transmission ion chamber located in front of the samples.

The protocol implemented to optimize the beam conditions for sample irradiations was presented, showing a methodology to reach low currents (of the order of tens of nA) without modyfing the beam optics.

The energy of the protons was measured in air (at the sample position) using an ion implanted silicon detector.

The field homogeneity was measured with GaFChromic films (EBT3) by studying the color distribution over the irradiated area of the films. At the sample surface a value better than 5 % was obtained by scattering the protons on a Au target of a thickness 5.4 mg/cm^2.

Once the best conditions for sample irradiations were reached, dosimetry studies were performed.

EBT3 films were irradiated with 6 MV photon beams at the HUVM and their response was calibrated in absorbed dose using the protocol established at the HUVM (D_{EBT3}). Then, other films belonging to the same production series were irradiated with the optimized proton beam. Their response in optical density as function of dose was compared to the calibration curve obtained for the films irradiated at the HUVM. It was observed that the calibration curve fits very well the data obtained with proton irradiation, thus, allowing to use this curve to calibrate the films also for protons.

The results were compared to the absorbed dose calculated by measuring the beam fluence with the IC (D_{FL}), revealing that, outside the Bragg peak region, the ratio D_{EBT3}/D_{FL} = 1.0- 1.1.

These results suggest that the absorbed dose for photon irradiations is similar to the one for proton irradiations; therefore, such films can be successfully adopted as absolute dosimeters when the protons passing through the film are not in the region of the Bragg peak.

The measurements, in the Bragg peak region, showed effects of saturation in the films when the films were irradiated by beams with higher LETs.

In this case, the ratio between the dose values obtained from the films and those calculated on the basis of the fluence measurements varied significantly. This phenomenon is known in literature as "quenching". In these measurements, it was noticed that the values of quenching vary with the amount of dose on the film: at low doses (less than 5 Gy), the ratio D_{EBT3}/D_{FL} varies between 0.62 - 0.89, for doses higher than 10 Gy it is in a range of 0.33 - 0.77.

The quenching effect can be due to numerous factors and further studies will be necessary to establish the nature of such an effect. A possible explanation is that the number of radiation-induced activated polymerization sites increases with LET until eventually no more sites are available for activation and the polymerization stops locally.

Furthermore, a direct measurement of the Bragg curve in air was performed and compared to Geant 4 simulations. The position of the Bragg peak was found to agree within 5% with the measurement.

As future work, more measurements are planned in order to furnish the curves for netOD (for the RGB channels) in a dose range of 0-20 Gy for different values of LETs.

This Chapter ends presenting the application of this setup for the irradiation of mammalian cancer cells. In fact, this setup assures a uniform distribution of the dose onto the whole sample and furnishes an accurate dosimetry for cell irradiations. Preliminary tests were conducted at the plateau region of the Bragg curve where the dosimetry can be provided with high precision. These studies focused on the DNA damage provoked with proton irradiations in a dose range of 0.25 - 5 Gy. The results were compared to the DNA damages caused by photon beams

for the same dose range. The number of foci present for proton irradiations and the ones for photons showed the same trend and the hyper sensitivity was noticed for doses ≤ 1 Gy. These very first radiobiological experiments demonstrated the feasibility of such studies at the CNA Tandem accelerator.

Chapter 5

Conclusions and perspectives

This thesis work presents two studies which have as common ground the dosimetry. The first part presents the characterization a novel dual chip SSSSD designed by this research group, together with its dedicated electronics, data acquisition system and manufactured phantoms. This system has been implemented to provide dose maps in the axial plane for complex treatment verification in conventional radiotherapy. In the second part of this thesis, the procedure adopted for the optimization of proton beams to perform dosimetry studies along the Bragg curve is presented. Particular attention is given to the study of the beam homogeneity, the measurement of the energy of the protons incident onto the samples and the dosimetry using an ionization chamber and EBT3 films. At the end, the results of a first set of irradiations onto cancer cell samples is presented, comparing the DNA damages produced by 3.83 MeV protons to those induced by 6 MV photon beams.

5.1 2D dose verification in complex radiotherapy treatments

The novel system presented in Chapter 3 allows to perform the verification of complex radiotherapy treatments. The system consists of several parts: the dual-SSSSD detector (designed within this research group), two phantoms, the electronics, and the data acquisition and analysis interfaces.

At the beginning, the detector was placed in a slab phantom, with its active area perpendicular to the beam axis, and characterized. Its response was calibrated in absorbed dose to water in standard conditions. This study was previously performed in [7], but, since the detector's original design and the electronics underwent changes, this calibration had to be repeated here.

The following results were obtained:

- Detector strips have a linear response to the irradiation.
- Penumbra and PDD are compatible to hospital measurements within 1 %.
- Output factor results show a difference of 1-2 % from hospital measurements for beam fields bigger than 5×5 cm^2.
- Dose thresholds: measurements of the dose at a beam fluence of 2 MU are obtained with an uncertainty of 12 %, while, dose results with a relative uncertainty better than 2 % are found for beam fluences equal or bigger than 10 MU.

The detector was then placed in the cylindrical phantom. In this configuration, the system was calibrated under treatment conditions and used for dose map reconstruction in the axial plane. The measurements and the calibration in treatment conditions, plus the dose map reconstruction with this system have been presented and studied for the first time in this work. The most relevant results are summarized below:

- The calibration previously done for the slab phantom could not be applied straightforward because the cavity created in the medium had different dimensions: the data had to be corrected applying new calibration factors to take into account the new configuration. Those factors are calculated comparing the experimental data with the dose received by each strip according to TPS algorithm. Calibration factors for each detector strip "i " can be considered independent of the angles between the strips and the radiation field.
- The algorithm for dose map reconstruction developed for the previous detector ([1]) was modified to be adapted to the new system. An axial dose

map was obtained with an improved resolution with respect to the previous system, thanks to the reduction of the detector element pitch and the bigger active area. The reconstructed map of absorbed dose shows an agreement within 8% with the dose map simulated by the TPS.

Despite the advantages of this novel system with respect to the previous prototype, some limitations had to be faced regarding the fragility of the detector's Kapton cables and connectors, and of the ADC components.

Future work

In the final prototype, some elements that can prevent the cable damages (guides for the cables) and a major robustness and radiation hardness of the electronics would improve significantly the whole system.

A new algorithm for the dose map reconstruction will be developed based on iterative calculations: an initial image is chosen, then projected and compared with the experimental data. From this comparison, the corrections are obtained and the image is updated. This procedure is repeated iteratively, until acceptable values are obtained. This will allow to obtain a dose map reconstruction over the whole detector area and the application of filters will be optional.

Besides the DSSSSD, the possibility of using a pixelated detector will be evaluated in order to provide directly a 2D dose map without the need of developing dedicated reconstruction algorithms.

5.2 Dosimetry of low-energy protons

In this section, the main features of the physical and radiobiologcal studies using low energy protons are summarized and discussed.

The methodology developed in this work consists of:

- A dedicated setup was installed in one of the beamlines of the 3MV Tandem accelerator at CNA with the main objective of obtaining a system which provides the best conditions to irradiate biological samples with low energy protons.

- A protocol for the beam optimization has been established, to obtain low current beams and homogeneous beam profiles for the irradiation fields. A field homogeneity, measured using EBT3 films, of 5 % in a circle of 3.5 cm of diameter (which corresponds to the dimensions of the cell sample cultures) is obtained using a Au scatterer of 5.4 mg/cm^2.

The main results obtained for the dosimetry studies are:

- The measurements, without degrading the beam energy show that the dose calibration used at the HUVM for the EBT3 film under photon irradiation, can be successfully adopted for low energy protons outside the Bragg peak region, as it has been verified through the IC fluence measurements.
- The measurements degrading passively the beam energy show the effects of saturation that occur when the LET increases. In this case, the ratio between the dose values obtained from the films and those calculated on the basis of the fluence measurements varies significantly. This effect is more remarkable for doses higher than 10 Gy.
- An additional study, a direct measurement of the Bragg peak in air, was performed and the results were compared to the Geant 4 simulations, obtaining a range agreement of 5%.

Finally, using the irradiation setup implemented in this work, first irradiations of biological samples were performed.

Breast cancer cells of the MCF-7 line were irradiated and the DNA damage induced was studied as function of dose.

The DNA damage increases with the absorbed dose as predicted by the linear quadratic model, except for doses lower than 1 Gy, for which, the DNA damage is larger than the one predicted. This phenomenon is known as "low dose hyper-radiosensitivity". This preliminary study shows the feasibility of the setup installed at the 3 MV Tandem accelerator for biological studies.

Future work:

- More measurements using EBT3 films will be performed in order to provide the curves of netOD at the plateau, maximum and distal fall-off regions of

the Bragg curve covering a dose range of 0-20 Gy. This has the final goal of establishing a precise correlation between the increase of the LET and the quenching covering the whole dose range for which the results of EBT3 are considered reliable.

- Further experiments will be performed with biological samples; the objective is to be able to perform irradiations along the Bragg curve to study the RBE.
- In addition, the protocol established for the optimization of the beam for sample irradiations is going to be adapted (with the convenient modifications) at the cyclotron installed at CNA, that provides proton beams of 10 MeV. Thus, an extension of the dosimetry studies with the EBT3 films is going to be performed at higher energies. Besides, irradiations of cell cultures are planned to study DNA damages produced by protons of higher energy.

Appendix A

Appendix

A.1 Energy loss through the beam line elements

Target N°	Energy remain (MeV)
0	5.233
1	5.01
2	4.44
3	4.31
4	4.19
5	4.09
6	3.97
7	3.87
8	3.75
9	3.58
10	1.89
11	1.25
12	stopped

TABLE A.1: energy loss, step by step, through each beam line component

Bibliography

[1] Patent at the oemp - oficina española de patentes y marcas – ministry of industry & commerce: Number p201101009 (13/09/2011).

[2] Z. Abou Haidar. *A 2D Silicon Detector System for Complex Radiotherapy Treatment Verification*. PhD thesis, University of Seville, 2012.

[3] Z. Abou et al. Output factor determination for dose measurements in axial and perpendicular planes using a silicon strip detector. *Phys. Rev. STAB*, 15: 042802, 2012.

[4] M. A. Cortés-Giraldo. *Desarrollos y aplicaciones de GEANT4 para radioterapia y microdosimetría en detectores y circuitos integrados*. PhD thesis, University of Seville, 2011.

[5] A. Bocci et al. et al. Silicon strip detector for a novel 2d dosimetric method for radiotherapy treatment verification. *NIM A*, 673:98–106, 2012.

[6] M. A. G. Alvarez et al. Novel dual single sided silicon strip detector chip for radiotherapy verification. *Proceedings of Science*, page 049, 2013.

[7] A. Selva. Characterization of a silicon strip detector for radiotherapy use. Master's thesis, University of Padova, 2014.

[8] M. Ovejero. *Perfeccionamiento de un Sistema para Vericar Tratamientos de Radioterapia y diseño del nuevo entorno VeRa*. PhD thesis, University of Seville, 2015.

[9] M. C. Battaglia, D. Schardt, J. Espino, et al. Dosimetric response of radiochromic films to protons of low energies in the bragg peak region. *Physical Review Accelerators and Beams*, 2016.

[10] M. Belli et al. Inactivation and mutation induction in v79 cells by low energy protons: Re-evaluation of the results at the lnl facility. *International Journal of Radiation Biology*, 63(3), 1993.

[11] E. Segrè. *Nuclei and Particles*. 2 edition, April 1982.

[12] M. Jermann. Particle therapy statistics in 2013. *Int. J. Part. Ther.*, 1:40–43, 2014.

[13] http://www.radiologyinfo.org/en/info.cfm?pg=linac.

[14] http://www.rtanswers.org/statistics/aboutradiationtherapy/.

[15] http://www.prostatecancertreatment.co.uk/treatment-options/radiotherapy/.

[16] J. M. Slater. *From X-Rays to Ion Beams: A Short History of Radiation Therapy*. springer edition, 2012.

[17] D. Schardt. Hadrontherapy. *Springer Proceedings in Physics*, 182:187–191, 2015, La Rabida International Scientific Meeting on Nuclear Physics.

[18] W. R. Leo. *Techniques for Nuclear and Particle Physics Experiments*. Springer-verlag edition, 1987.

[19] Linear energy transfer. *ICRU report 16*, 1970.

[20] E. B. Podgorsak. *Radiation Oncology Physics: A Handbook for Teachers and Students*. IAEA, 2005.

[21] D. Schardt et al. Heavy-ion tumor therapy: Physical and radiobiological benefits. *Review of Modern Physics*, 45, 2010.

[22] P. V. Vavilov. Ionizational losses of high energy heavy particles. *Zh. Eksp. Teor. Fiz.*, 32:920–923, 1957.

[23] N. Bohr. Scattering and stopping of fission fragments. *Phys. Rev.*, 58:654–655, 1940.

[24] S. P. Ahlen. Theoretical and experimental aspects of the energy loss of relativistic heavily ionizing particles. *Phys. Mod. Rev.*, 52:121–173, 1980.

[25] J. Izweska and G. Rajan. Radiation dosimeters. http://www-naweb.iaea.org/nahu/DMRP/documents/Chapter3.pdf.

[26] S. Devic. Radiochromic film dosimetry: past, present and future. *Physica Medica*, 27:122–134, 2011.

[27] A. Niroomand-Rad et al. Radiochromic film dosimetry. *Medical Physics*, 25: 11, 1998.

[28] S. Devic et al. Optimizing the dynamic range extension of a radiochromic film dosimetry system. *Med Phys*, 36:429–437, 2009.

[29] L. Xu et al. Measurement of lateral dose distributions using gafchromic ebt films and ptw starcheck 2-d array. *Med Phys*, 36:2624, 2009.

[30] A. Rink et al. Temperature and hydration effects on absorbance spectra and radiation sensitivity of a radiochromic medium. *Med Phys*, 35:4545–55, 2008.

[31] Bidimensional silicon dosimeter: Development and characterization.

[32] Small field measurements with a novel silicon position sensitive diode array.

[33] A silicon strip detector dose magnifying glass for imrt dosimetry.

[34] C. J. Karzmark et al. Medical electron accelerators. *McWrall-Hill Inc., New York, 1973*.

[35] ICRU. Prescribing, recording, and reporting intensity-modulated photon-beam therapy (imrt). Report 83, International Commission on Radiation Units and Measurements (ICRU), 2010.

[36] IAEA. *Accuracy Requirements and Uncertainties in Radiotherapy*.

[37] https://es.mathworks.com/.

[38] Philips healthcare, available on-line at http://www.healthcare.philips.com.

[39] National Instruments. *Software de Desarrollo de Sistemas NI LabVIEW*. http://www.ni.com/labview/esa/.

[40] T. T. Puck and P. I. Marcus. Action of x-rays on mammalian cells. *J. Exp. Med.*, 103:653–666, 1956.

[41] E. Hall. Radiobiology for the radiologist. *5th, ed. Lippincott Williams and Wilkins, Philadelphia.*, 2000.

[42] H. Paganetti. Relative biological effectiveness (rbe) values for proton beam therapy. variations as a function of biological endpoint, dose, and linear energy transfer. *Phys. Med. Biol.*, 59:R419–R472, 2014.

[43] F. Romano et al. A monte carlo study for the calculation of the average linear energy transfer (let) distributions for a clinical proton beam line and a radiobiological carbon ion beam line. *Physics in Medicine and Biology*, 59 (2863), 2014.

[44] C. Stannard et al. Radiotherapy for ocular tumours. *Eye*, 27(119–127), 2012.

[45] *http://www.tek.com/keithley-low-level-sensitive-and-specialty-instruments/keithley-high-resistance-low-current-electrom.*

[46] E. C. Montenegro et al. Study of proton beam diffusing system for pixe analysis. *Nuclear Instruments and Methods*, 164:231–234, 1979.

[47] *http://www.ortec-online.com/.*

[48] V. L. Highland. Some practical remarks on multiple scattering. *Nuclear Instruments and Methods*, 129:497–499, 1975.

[49] C. Rodríguez et al. A new implementation of multichannel radiochromic film dosimetry. *Rev. Fis. Med*, 15:49–54, 2014.

[50] *EBT3 GafChromic films user guide.*

[51] R.Arrans et al. *Rev.Fis. Med*, 10(2):83–104, 2009.

[52] J. Sorriaux et al. Evaluation of gafchromic EBT3 films characteristics in therapy photon, electron and proton beams. *Physica Medica*, pages 1–10, 2010.

[53] S. Agostinelli et al. Geant4–a simulation toolkit. *Nuclear Instruments and Methods in Physics Research A*, 506:250–303, 2003.

[54] http://www.srim.org/srim/srimlegl.htm.

[55] V. Casanova et al. Dosimetric characterization and use of gafchromic ebt3 film for imrt dose verification. *Journal of applied clinical medical physics*, 14 (2), 2012.

[56] S. Reinhardt et al. Investigation of EBT2 and EBT3 films for proton dosimetry in the 4-20 MeV energy range. *Radiat. Environ. Biophys.*, 54:71–79, 2015.

[57] L. Zhao and I. J. Das. Gafchromic EBT film dosimetry. *Phys. Med. Biol.*, 55:N291–N301, 2010.

[58] F. Fiorini et al. Under-response correction for EBT3 films in the presence of proton spread out Bragg peaks. *Physica Medica*, 30:454–461, 2014.

[59] D. Kirby et al. LET dependence of GafChromic films and ion chamber in low-energy proton dosimetry. *Phys. Med. Biol.*, 55:417–430, 2010.

[60] H. Paul and D. Sánchez-Parcerisa. A critical overview of recent stopping power programs for positive ions in solid elements. *Nuclear Instruments and Methods in Physics Research B*, 312:110–117, 2013.

[61] Stopping powers and ranges for protons and alpha particles. *ICRU report*, (49), 1993.

[62] E. Sterpin et al. Extension of penelope to protons: simulation of nuclear reactions and benchmark with geant4. *Medical Physics*, 40:111705, 2013.

[63] L. G. Smith et al. et al. Investigation of hypersensitivity to fractionated low-dose radiation exposure. *Int. J. Radiation Oncology Biol. Phy*, 45:187–191, 1999.

[64] MC Joiner et al. et al. Low-dose hypersensitivity: current status and possible mechanisms. *Int J Radiat Oncol Biol Phys*, 49(2):379–89, 2001.

[65] Low-dose radiation hyper-radiosensitivity in multicellular tumour spheroids.

[66] Pawel Jacek Znojek. *Investigation of the role of poly(ADP-ribose)polymerase inhibition in topoisomerase I poison-induced cytotoxicity.* PhD thesis, Newcastle University, 2011.